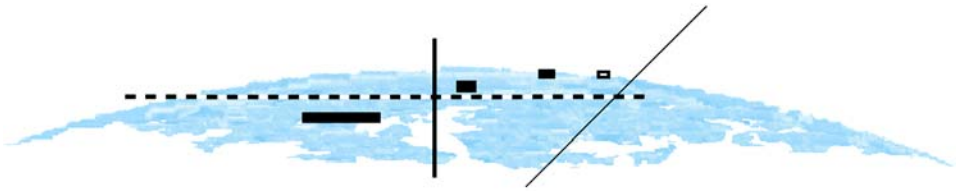

GeoForschungsZentrum Potsdam

STIFTUNG DES ÖFFENTLICHEN RECHTS

Scientific Technical Report

ISSN 1610-0956

Benjamin S. Heit

Teleseismic tomographic images of the Central Andes at 21°S and 25.5°S: an inside look at the Altiplano and Puna plateaus

Dissertation zur Erlangung des Doktorgrades
am Fachbereich Geowissenschaften
der Freien Universität Berlin

2005

Erster Gutachter: Priv. Doz. Dr. Günter Asch

Zweiter Gutachter: Prof. Dr. Rainer Kind

Tag der Disputation: 15.11.2005

Denying temporal succession, denying the self, denying the astronomical universe, are obvious acts of desperation and secret consolation. Our fate is not frightful because it is unreal; it is frightful because it is irreversible and ironclad. Time is the thing I am made of. Time is a river that sweeps me along, but I am the river; it is a tiger that tears me apart, but I am the tiger; it is a fire that consumes me, but I am the fire. The world, unfortunately, is real.

J. L. Borges

Contents

Abstract

A set of 59 seismological stations was deployed in the Central Andes region at 21°S (Chile-Bolivia) along a profile ~600 km long and were operated between 2002 and 2004. The teleseismic tomographic images (from P- and S- waves) show low-velocity anomalies that are interpreted as the effects of melting or fluids at both flanks of the Altiplano plateau. Beneath the Central Volcanic Zone (CVZ) a low-velocity anomaly is interpreted to be caused by fluids that are the origin of the volcanic material from the CVZ. A low-velocity anomaly in the upper crust is interpreted as the Altiplano Low-Velocity Zone that appears to extend as far to the east as the Eastern Cordillera. A high-velocity body between 100 km and 150 km depth is interpreted as being part of the old cold lithosphere that detached from the base of the crust. The Brazilian Shield is thought to be responsible for the strong high-velocity anomaly on the eastern side of the Central Andes.

In addition, another set of 19 stations was deployed in the southern Argentine Puna along a profile ~200 km long and were run over the same period of time (2002-2004). The intention was to study the crustal thickness at 25.5°S, where delamination of the lithosphere was proposed to explain the higher elevation of the Puna plateau. Beneath the plateau a negative velocity anomaly is observed and interpreted here as being the location of fluid transfer between the deeper and shallower portions of the crust, that emanate from the Benioff zone at depths of ~200 km. This anomaly clearly divides in two branches: one to the west towards the volcanic arc (CVZ) and the other to the east where the back-arc volcanoes are located. On their way to lower depths, the fluid paths are probably influenced by the presence of nearby isotherms. The bifurcation of the ascending path could be related to the presence of the lithosphere-asthenosphere boundary (LAB) at ~100-130 km. Based on our observations, the type and form of the anomaly, it is possible to propose the presence of a return-flow type model for fluid ascent in contraposition to the assumed corner-flow model usually proposed

for the Andes. The fluids that cause the seismic anomalies beneath the Puna plateau are generated at deeper levels in the asthenosphere and ascend parallel to the oceanic slab in the manner of a return-flow.

In the crust and beneath the Salar de Antofalla (SA), a high-velocity block with seismic activity is interpreted as part of the old and cold Palaeozoic magmatic arc (Faja Eruptiva de la Puna Occidental). The presence of this block is may be responsible for the distribution of volcanic activity localized at both sides of this anomaly. Eastern of the SA, it is possible to recognize a zone with low-velocities beneath the Galan volcano. A sharp limit imposed by high velocities, probably related to metamorphic rocks from the Paleozoic basement (Tacuil and Luracatao ranges) can be detected on the east of the profile.

A high-velocity block with seismic activity is located in the crust beneath the Salar de Antofalla (SA) and interpreted as part of the old and cold Palaeozoic magmatic arc (Faja Eruptiva de la Puna Occidental). This block might be responsible for the distribution of volcanic activity localized at both sides of this anomaly. Beneath the Galan volcano and east of the SA, a zone with low-velocities can be recognized. A sharp limit towards high-velocities can be observed on the east of the profile, probably related to metamorphic rocks from the Palaeozoic basement (Tacuil and Luracatao ranges).

Zusammenfassung

Im Bereich der Zentralen Anden zwischen 2002 und 2004 wurden 59 seismologische Stationen betrieben, welche bei 21°S (Chile-Bolivien) entlang eines ~600 km langen Profils aufgestellt wurden. Die teleseismische tomographischen Bilder entlang des untersuchten Profils (von P- und S-Wellen) zeigen erniedrigte Geschwindigkeitsanomalien, welche in Form von Schmelz- oder Flüssigkeitsvorkommen an beiden Flanken des Altiplano Plateaus/Hochland interpretiert worden. Eine geringe Geschwindigkeitsanomalie unterhalb der Zentralen Vulkanischen Zone (CVZ), wird als Fluide interpretiert, die in Zusammenhang mit dem vulkanischen Materials der CVZ stehen. Eine Anomalie mit erniedrigter Geschwindigkeit innerhalb der oberen Kruste wird als die Altiplano Low Velocity Zone (ALVZ) interpretiert, die sich bis hin zur östlichen Kordilliera zieht. Ein Bereich erhöhter Geschwindigkeit zwischen 100 und 150km Tiefe, wird als Teil der alten und kalten Lithosphäre angesehen, die sich von der Basis der Kruste getrennt hat. Eine stark erhöhte Geschwindigkeitsanomalie im östlichen Teil der Zentralen Anden wird dem brasilianischen Schild zugeschrieben.

Im gleichen Zeitraum (2002-2004), wurden weitere 19 Stationen entlang eines ~200km langen Profil im Süden der argentinischen Puna betrieben. Das Ziel dieses Profils war die Krustendicke bei 25.5°S zu bestimmen wo die deutliche Heraushebung des Puna Plateaus mit der Delamination der Lithosphäre erklärt wird. Das Ergebnis der vorliegenden Arbeit zeigt eine negative Geschwindigkeitsanomalie unterhalb des Puna Plateaus an, für die ein Fluidtransport zwischen dem tieferen und flacheren Bereich der Kruste verantwortlich gemacht wird, welcher von der Benioff Zone in einer Tiefe von ~200km ausgeht. Diese Anomalie trennt sich deutlich in zwei Bereiche auf: der eine Ast verläuft westlich in Richtung des vulkanischen Bogens (CVZ) während der andere in östlicher Richtung zu den back-arc Vulkanen verläuft. Bei dem Aufstieg der Fluide in flachere Bereiche der Kruste werden die

Wege wahrscheinlich durch in der Nähe vorkommende höher Temperaturen beeinflusst (e.g. 1400°C). Die Verzweigung des Aufstiegpfades kann in Verbindung mit der Grenze zwischen der Lithosphäre und der Astenosphäre (LAB) bei ~100 bis 130km gebracht werden. Allerdings liegen die Ergebnisse der seismischen Stationen oberhalb der LAB in den südlichen Zentralen Anden zurzeit noch nicht vor.

Aufgrund unserer Beobachtungen, des Typ und der Form der Anomalie liegt es nahe für die aufsteigende Fluide einen “return-flow” anzunehmen. Diese Interpretation steht im Widerspruch zu den für die Anden üblicherweise vorgeschlagenen “corner-flow”. Die für die Anomalien in der Puna verantwortlichen Fluide werden wahrscheinlich in tieferen Bereichen der Asthenosphäre gebildet und steigen als “return-flow” parallel zur ozeanischen Platte auf. Unterhalb des Salar de Antofalla (SA) ist im Bereich der kontinentalen Kruste ein Block mit erhöhter Geschwindigkeit und seismischer Aktivität zu beobachten, der als Teil des alten und kalten paläozoischen magmatischen Bogens (Faja Eruptiva de la Puna Occidental) interpretiert wird. Dieser Block ist möglicherweise für die Verteilung der vulkanischen Aktivität auf beiden Seiten der Anomalie verantwortlich. Östlich vom SA ist unterhalb des Vulkans Galan eine Zone erniedrigter Geschwindigkeiten zu beobachten, während erhöhte Geschwindigkeiten im Osten des Puna Plateaus in Verbindung mit den metamorphen Gesteinen des paläozoischen Basements (Tacuil und Luracatao Kette) gebracht werden.

Resumen

Un conjunto de 59 estaciones de registro sismológico fueron instaladas en los Andes Centrales entre los paises de Chile y Bolivia a lo largo de un perfil de aproximadamente ~600 km de largo en sentido este-oeste (transversal a la cadena andina) a 21°S entre comienzos de 2002 y fines de 2004. Imágenes tomográficas de telesismos de ondas P y S muestran anomalias de baja velocidad relativa que son interpretadas como producto de fluidos o melting a ambos flancos del plateau Altiplánico. Por debajo de la zona de arco volcánico (CVZ por Central Volcanic Zone) se interpreta la presencia de fluidos que dan origen a material magmático del arco volcánico debido a la presencia de una anomalia de baja velocidad. En la parte central del perfil y casi en toda su extensión por debajo del Altiplano, se detecta la presencia de la zona de baja velocidad altiplánica (ALVZ - Altiplano Low-Velocity Zone) que parece extenderse hasta inmediaciones de la Cordillera Oriental. Por encima de la zona de Benioff y entre 100-150km de profundidad, un bloque de alta velocidad relativa es interpretado como parte de litósfera antigua, separado o desprendido de la base cortical por diferencia de temperatura y/o densidad con respecto a la roca circundante en la litósfera sudamericana. El escudo Precámbrico de Brasil (aqui BS, también llamado Guaporé) debe ser responsable por el cambio de bajas a altas velocidades que se observa al este de la Cordillera Oriental y zona Interandina en el extremo oriental de la zona de estudio.

Un perfil adicional de 19 estaciones sismológicas, de características similares al anterior, fue instalado en el extremo sur de la Puna Austral Argentina, durante el mismo periodo de tiempo. La disposición este-oeste de las estaciones, desde el arco volcánico (limite con Chile) hasta el extremo occidental del Valle Calchaquí en la localidad de Tacuil alcanzó una extensión de aproximadamente ~200 km. La intención en este caso fue la de analizar la estructura cortical y dimensiones de la corteza a 25.5°S donde procesos de delaminación litosférica fueron propuestos para explicar la presencia de magmatismo tipo OIB y la mayor

elevación de la Puna Argentina con respecto al Altiplano de Bolivia. En este caso y por debajo de las porciones centrales del plateau, es posible observar la presencia de una anomalia negativa de velocidades que virtualmente "emana" desde inmediaciones de la zona de Benioff a unos 200 km de profundidad para luego bifurcarse en dos, una hacia el oeste donde se encuentra el arco volcánico y otra hacia el este en la zona de algunos volcanes de retro-arco volcánico. Las razones de una bifuración para los fluidos que ascienden hacia la corteza puede deberse a una variación térmica en las isotermas de esta parte de los Andes Centrales o bien debido a la presencia del límite entre litósfera y astenósfrea (LAB por Lithosphere-Asthenophere Boundary) entre los 100-130 km de profundidad. La forma y dispocisión de esta anomalia puede estar indicando la presencia de un tipo de flujo conocido como "return-flow" en contraposición a los modelos usualmente propuestos para los Andes conocido como de "corner-flow". Un tipo de flujo "return-flow" deberia tener su origen a partir de la liberación de fluidos en proximidades de un grupo de sismos en la zona de Benioff (cercana a los 200 km de prof.), que ascienden luego, hacia la corteza en forma paralela a la placa subductada.

La parte central de este perfil muestra una anomalia positiva (alta velocidad) que correlaciona con la presencia del bloque del Salar de Antofalla probablemente representando a rocas del arco magmático Cambro-Ordovícico de la Faja Eruptiva de la Puna Occidental. En la corteza es posible además, observar la presencia de una fuerte anomalía negativa en inmediaciones del volcán Galán a profundidades de la corteza superior. El limite oriental esta marcado por anomalias positivas probablemente relacionadas con la presencia del basamento metamórfico de la Cordillera Oriental (sierras de Tacuil y Lucaratao).

Chapter 1

Introduction

The study of mountain ranges developed at converging plates is fundamental for understanding the processes that govern the subduction of one plate, overriding of the other and in some cases, the collision of both. Within the context of converging plates, there are two large plateau regions in the world: one is the Tibetan plateau which is associated with a collisional orogen between two continental plates (India and Asia). The other one, the Altiplano-Puna plateau, is related to subduction of an oceanic plate (Nazca) beneath a continental plate (South America) in the Central Andes. The elevation of the Altiplano-Puna plateau (~ 4 km) achieved under a subduction regime involving magmatism, shortening, deformation and mass transfer within the upper lithosphere (e.g. Coira et al., 1982; Isacks, 1988; Reutter et al., 1988, Baby et al., 1992; Gubbels et al., 1993; Scheuber et al., 1994; Allmendinger et al., 1997), shows the importance of geodynamic processes to the generation of the impressive Andes ranges and perhaps ironically, how little these generation mechanisms are understood.

The “Cordillera de los Andes” is a long mountain belt located along the western edge of the South American continent, extending for over 7000 km from north to south. It represents one of the world’s best examples of an area that has been formed under the effects of uplift and magmatism arising from the subduction of an oceanic plate (Nazca Plate) under a continental plate (South American Plate) (Figure 1.1). The Andes reach their greatest width at a region known as the Central Andes (central sector between ~14°S and ~24°S) where subduction of the Nazca plate

occurs at angles near 20-30° at a rate of 65mm/yr (Angermann et al., 1999; Cahill and Isacks, 1992).

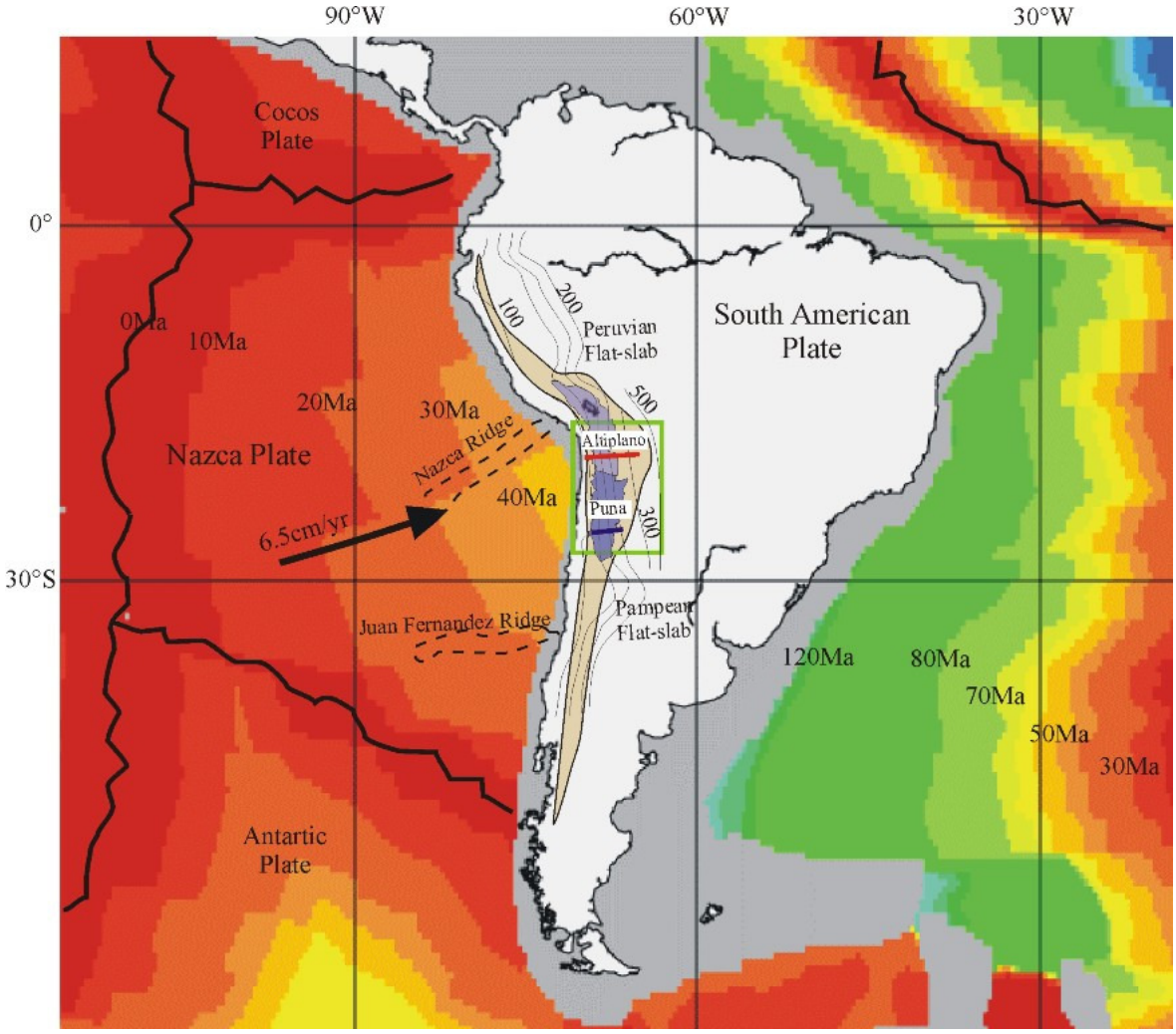

Figure 1.1: The South American continent and the associated tectonic plates. Different colours represent sea-floor age in million of years; bold lines: limit between oceanic plates (spreading centers); Arrow: Nazca/South American plates convergence rate (Angermann et al., 1999). Brown shaded area shows the extent of the Andes from ~5°S to~ 47°S. Thin lines are depth contours of the Wadati-Benioff zone in km (Cahill and Isacks, 1992). Green rectangle: Altiplano-Puna study area in the Central Andes. Red line: Altiplano profile at 21°S. Blue line: Puna profile at 25.5°S. Sea-floor ages after Müller et al., 1997).

Several authors have proposed different geological classifications to describe the Andes. The most accepted approach was given by Gansser (1973) who, based on tectonic and geological differences among the segments of the orogen, proposed three main regions: Northern, Central and Southern Andes. The Northern Andes, north of ~3°S, are mainly constituted of an oceanic basement as a consequence of oceanic crust accretion during Mesozoic times (e.g. Ramos 1999).

The Southern Andes (~47°S to ~52°S) are developed south of the triple junction zone where the South American, Nazca and Antarctic plates produce ridge collision deposits without magmatic activity from the arc (e.g. Ramos, 1999).

The Central Andes extends from ~3°S to ~47°S and are flanked by flat-slab areas to the north (between ~3°S - ~14°S) and to the south (~28°S - ~32°S) where subduction is horizontal to sub-horizontal. Portions of the oceanic plate subducting the central parts of the Andes (Figure 1.1) have ages between ~40 Ma and ~47 Ma (Müller et al., 1997). The Central Andes went through various stages of extension, compression and transtension, alternating with periods of tectonic inactivity (Reutter et al., 1988; Scheuber et al., 1994; Sempere et al., 1997). During Paleogene times, the actual configuration of the central part of the Andes began to take form due to compression between the involved tectonic plates (Pilger, 1981 and 1983; Pardo Casas and Molnar, 1987).

Crustal shortening, variable thickness in the crust and different dipping angles of the subducting plate along strike have created an elevated plateau in the central part of the Andean orogen with geological, morphological and magmatic characteristics that enable a differentiation between the Altiplano in the north (Bolivia and Peru) and the Puna in the south (north-western Argentina) (e.g. Schmitz, 1994; Allmendinger et al., 1997; Kley and Monaldi, 1998, Riller et al., 2001; Riller and Oncken, 2002).

The Altiplano-Puna plateau (Figure 1.1) is the main tectonic feature of the central Andean region and stretches for about ~1700 km from north to south. The plateau has an average elevation of ~4 km and is ~400 km wide. It is limited to the west by an active volcanic arc (Western Cordillera) and to the east by an active westward verging thin-skinned foreland thrust belt (Eastern Cordillera) (e.g. Kley and Rheinhardt, 1994; Whitman et al, 1996). To the east, the topography descends by steps at the Interandean Zone, the currently active Subandean fold-thrust Belt and the Chaco Plain that progressively overlaps with the Precambrian Brazilian shield (the location of the mentioned morphological units can be seen on Figures 3.1B and 6.1) (e.g. Wigger et al., 1994).

In the Central Andes, the presence of low-velocity layers in the upper crust (Wigger et al., 1994; Yuan et al., 2000 and 2002) and the position of bright spots (ANCORP Working Group, 1999 and 2003) as well as possible delaminated portions of the lithosphere (Schurr, 2000 and Schurr et

al., 2003) have been described and considered when resolving the internal structure of the Andean plateau (Haberland et al., 2001; Victor et al., 2004; Elger et al., 2005; Scheuber et al., submitted). Other processes, referring to the differences in constitution, tectonic shortening, altitude above sea level or topography, thickness of the crust, differences in volcanism and magmatism are not well understood (e.g. Allmendinger et al., 1997).

Therefore, the scientific community started to focus its attention on this region, in particular because of the well-known enigma that concerns the generation of a plateau in the absence of a collision scheme (Isacks, 1988; Reutter et al., 1988; Allmendinger and Gubbels, 1996). Hence, over the past two decades, a series of seismological projects (e.g. Wigger, 1991; Wigger et al., 1994; Patzwahl et al., 1999; Schmitz et al., 1997, ANCORP Working Group, 1999 and 2003; Graeber and Asch, 1999; CINCA Working Group, 1997; Haberland and Rietbrock, 1999; Schurr et al., 1999, Bock et al., 1998) were undertaken to bring light on understanding of the many interacting geologic-geodynamical processes in the Central Andes. These passive and active seismic experiments provided unique results that enabled, for the first time, the identification of deep structures in the crust as well as the depth and topography of the Moho- discontinuity (Beck et al., 1996, Zandt et al., 1996; Yuan et al, 2000). The Moho and implicitly the crust of the Andes mountain chain is a topic of study that has always been controversial. So far, the generation of magmas with related movement of fluids (e.g. Schilling et al., 1997) in correlation to earthquake clusters of the subducted slab has been suggested to explain melting and volcanic activity. The electrical conductivity of the Central Andes (e.g. Brasse et al., 2002) provided insight looks at units with anomalously conductive materials in the area of the plateau.

The last funding period of the Collaborative Research Center SFB-267 “Deformation Processes in the Andes” supported a two year deployment of instruments for a seismological project. Initially thought as a receiver function profile along two portions of the Central Andes, the aim was to improve the resolution of previously obtained results concerning Moho topography (e.g. Yuan et al., 2000) and collect data for applying other geophysical methods. In this study, a teleseismic tomography is performed using the collected data to analyze the different anomalies present in this area, as well as the extent to which these anomalies should reach. Previous global teleseismic tomography studies have been able to image the subduction zone on the base of P-wave analysis (Engdahl et al., 1997; Bijwaard et al., 1998). From the beginning of this project, one important issue concerned the morphological units in the subduction scheme and their

relative position with respect to older structures such as the Brazilian shield, which is thought to play a key role in understanding the plateau evolution (Wigger et al., 1994; Myers et al., 1998; Polet et al., 2000, Beck and Zandt, 2002). A comparison between both Altiplano and Puna plateaus, could help us to explain the differences that are observed in the data.

The present work consists in 6 chapters and a final section with additional information (Appendix). The main structure of each chapter is described as follows:

Chapter 2 briefly addresses the field deployment of instrumentation, the characteristics of the instruments and the data acquisition. Some steps followed while installing the stations are also described.

Chapter 3 describes the data processing and the teleseismic tomography algorithm used in this study. The algorithm is then applied to both data sets (Altiplano and Puna). Synthetic tests were first carried out to evaluate vertical and horizontal resolution. Finally, the real-data inversions were performed and the results presented in vertical and horizontal sections.

In Chapters 4 and 5 an overview of the geological history of the Altiplano-Puna plateaus is given, including geodynamical environment, tectonics and magmatic characteristics. The results obtained are presented for each profile separately.

Chapter 6 includes a discussion about the obtained results and their geodynamical implications; the results are compared with those obtained from previous projects and later presented as models for both plateaus. The results from receiver function images of the Moho and other discontinuities obtained from the same data set are compared with our tomographic results. Conclusions are presented in the last part of this work.

In the Appendix, a complete list of station information and instrument characteristics is presented as well as a list of the teleseismic events from the PDE catalogue used in this study. Additional diagrams, vertical and horizontal synthetic tests and real inverted data are also shown at the end of this section.

In the case of the Altiplano profile along 21°S the intention was to improve previous geophysical results. For this reason, this project was conducted: 1) over a longer period of time (almost two years) and 2) extended from the previous experiments (e.g. ANCORP profile see ANCORP Working Group, 1999, 2003) by some 200 km to the east, reaching the Interandean zone of Bolivia (Tarija ~64.5° W). In this way, our profile covers a west-east extension of ~600 km with 59 stations. The spacing between stations (10-15 km) allows us to detect upper mantle and lower-crustal anomalies, as well as, the distribution of anomalies related to structures in the Moho and upper crust (e.g. the extension of geological units at depth or crustal lineaments delimiting them).

The other set of 19 stations along 25.5°S (~200 km long) was also run for two years and with a spacing of 10 to 15 km. The intention was to get first geophysical results for the area of Galan volcano. By applying the teleseismic tomography method, the aim was to evaluate the state of the lithosphere and asthenosphere areas below the Southern Puna were delamination was proposed to explain a series of geological and geophysical observations (e.g. Kay and Kay, 1993; Schurr et al., 2003).

Chapter 2

2. Receiver Function Central Andes Project

The Receiver Function Central Andes (ReFuCA) project was a seismological study carried out along two different profiles at 21°S and 25.5°S where the stations were operated for a period of almost 2 years between 2002 and 2004. The project involved collaboration between scientist from Germany, Argentina, Bolivia and Chile within the collaborative research program "Deformation Processes in the Andes" SFB-267 (SonderForschungsBereich-267). The intention was to record teleseismic waves ***(P and S)***, for use of teleseismic tomography method.

2.1. Instrument deployment and data processing

During the last funding period of the SFB-267 program, in cooperation with GFZ-Potsdam and with the collaboration of our South American partners, a set of 59 seismological stations was deployed and operated (March 2002 - January 2004) at 21°S along a profile between the Coast of Chile at ~70°W and the western margin of the Interandean Zone system in Bolivia at ~64.5°W (see Figure 2.1). Instruments used for this experiment consisted of 47 short-period (SP) RefTek (Refraction Technology dataloggers) and EDL (Earth Data Logger) units equipped with 1-Hz Mark L4-3D seismometers and 9 SAM (Storage and Acquisition Module) with broadband (BB) Guralp CMG-3ESP seismometers *(see Appendix A.1. – Table 1 for details)*. The station spacing was about 10 km (Figure 2.1).

The events (at epicentral distances between 30° and 95°) used in this work are listed in the Appendix A.2. A total of ~500 GB of data were acquired and stored in the GEOFON Data Center[1]. Digital *P-waveforms* from 154 teleseismic events and 31 *S-waveforms* with $Mw \geq 5$ were obtained from PDE[2] catalogue. These events were located predominantly along the western coast of Central and North America and the Atlantic ridge. The ray coverage is generally well distributed but towards Antarctica the events are clearly less well represented (Figure 2.2).

In addition, a set of 19 stations was deployed at ~25.5°S and operated between July 2002 and January 2004 in a profile ~200 km long (Figure 2.1). The instruments used in this case were 10 short-period EDL units with 1-Hz Mark L4-3D seismometer and 9 SAM with BB Guralp CMG-3ESP seismometers *(Appendix A.1. - Table 2)*. The spacing between stations was about 10-15 km. A complete list of the events detected by this profile (≥30°≥95°) is presented in the Appendix A.2. Digital *P-waveforms* from 177 teleseismic events and 29 *S-waveforms* with $Mw \geq 5$ were also obtained from PDE catalogue and ~250 GB data were stored at GEOFON data center.

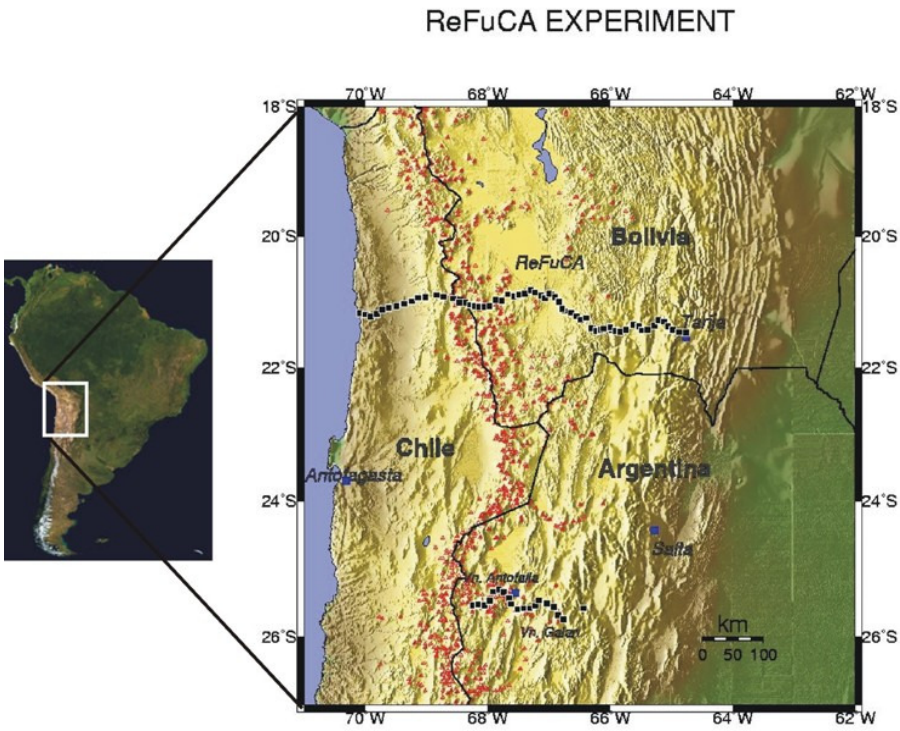

Figure 2.1: Location of the 21°S (RF) profile between the coast of Chile and the city of Tarija in Bolivia and the 25.5°S (PC) profile in the Argentine Puna. The southern profile is in the area of Antofalla and Galan volcanoes.

For both profiles, all stations were run with external hard-drives according to the instruments: 4-6 GB **Earth Data L**ogger and **SAM** and 20 GB **RefTek** (only in Bolivia and Chile). Timing was

synchronized at each station using Global Positioning System *(GPS)* receivers and the sampling rate for the SP stations was 100sps and 50sps for the BB stations. Power supply was provided by solar panels, one in case of short-period stations (50 watt) and two for broadband stations (100 watt). The power supply was stored by batteries attached to a regulator that controlled the energy provided to the instruments (Figure 5). All the instruments were provided by the Geophysical Instrument Pool Potsdam (GIPP-GFZ).

All raw data (~800 GB) has been processed, converted to MiniSEED format and stored at the *GEOFON*. Online requests to *GEOFON* were made in order to access the data that were afterwards converted from MiniSEED to Q-File format. This format was needed to use the SHM (Seismic Handler Motif from Stammler, 1992) program for picking the *P*- and *S*- *waves* first arrivals for the different components. For teleseismic tomography we used seismic waves generated at epicentral distances between 30° and 95° (Figure 2.2). At epicentral distances of less than 30° triplications occur in the crust and upper mantle boundary resulting in complication on P- and S- wave arrivals. At distances greater than 95°the phases become complicate due to interactions with the earths core (Walck, 1984).

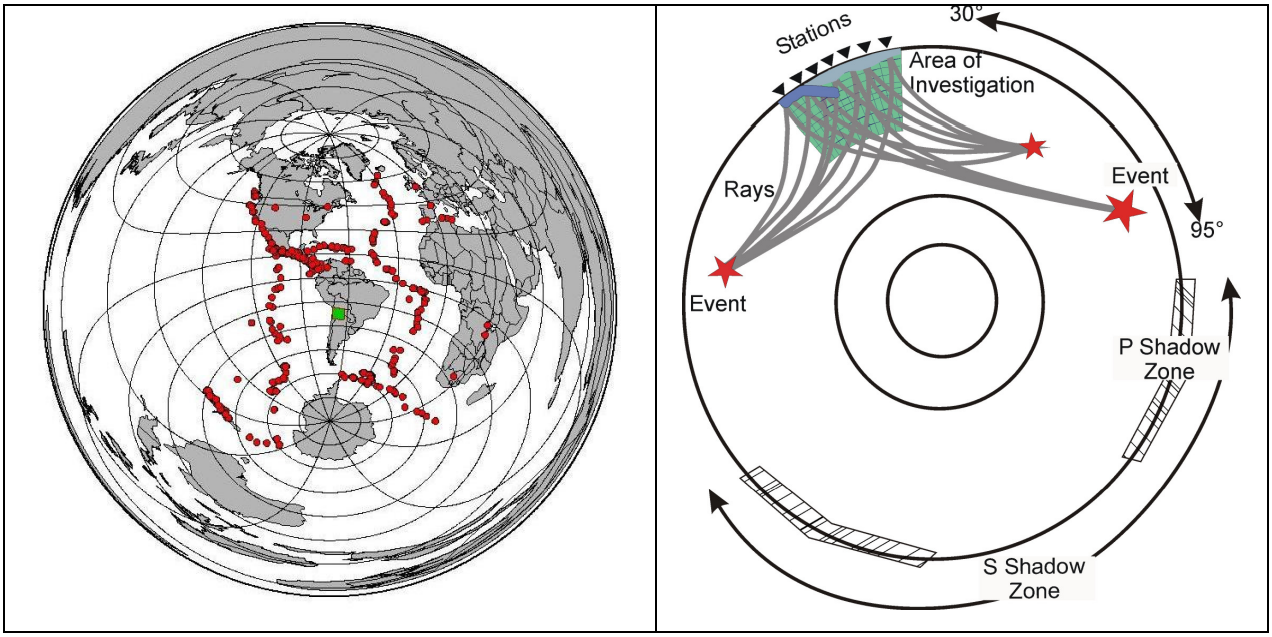

Figure 2.2: (Left) distribution of teleseismic events (red dots) used in this study for both seismological profiles between 2002 and 2004. Events that provided teleseismic arrivals for P- and S- phases are plotted together for epicentral distances between 30° and 95°. Note the inhomogeneous distribution of events from north and south and the more homogeneous distribution between east and the west of our study area (green square in the centre of South America). (Right) Cartoon showing the principle of teleseismic tomography; the area of investigation (green) with superimposed grid and ray tracing from three hypothetical events; P- and S- shadow zones also displayed.

Restitution of ground displacement was made for broadband and short-period signals separately. After restitution all traces had been filtered using pass band 1-3s 2nd order filter. SAM stations have showed, in some cases, a time delay that has been induced by a Firmware module problem. This time error was found to be 0.975 milliseconds (Güralp *pers. com.*), hence a data correction was possible. In those cases where the error proved bigger than the amount previously indicated, the data was not included in the analysis (Figures 2.3 and 2.4).

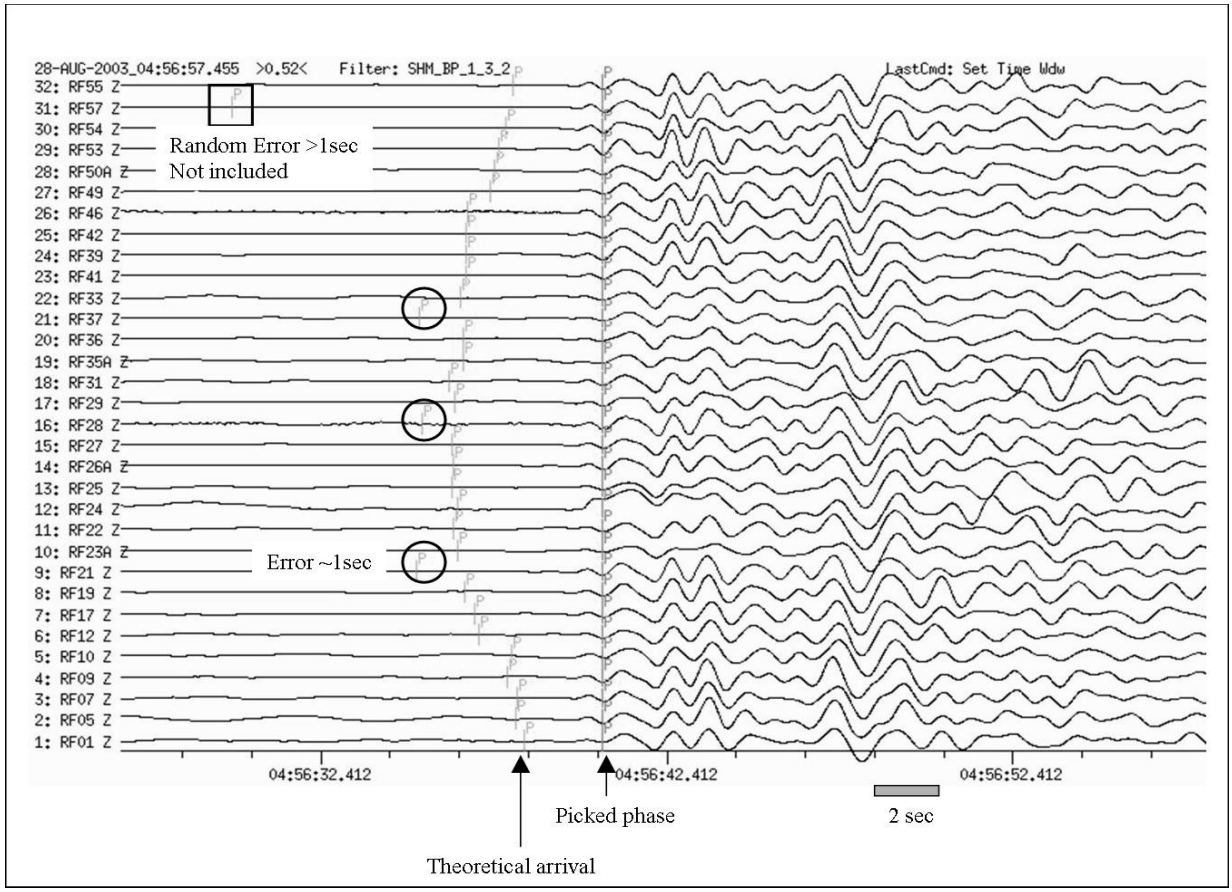

Figure 2.3: SHM screen showing an example of the vertical component (Z) of P waveforms from one event aligned by picked times after restitution and filtering for Altiplano profile at 21°S. The black circles include some of the P-wave delays detected during data processing due to the failure of the Firmware module (Güralp pers. com.). The square on the upper trace encloses the random error of the arrival of the phase probably related to poor GPS coverage (this type of data was excluded from analysis).

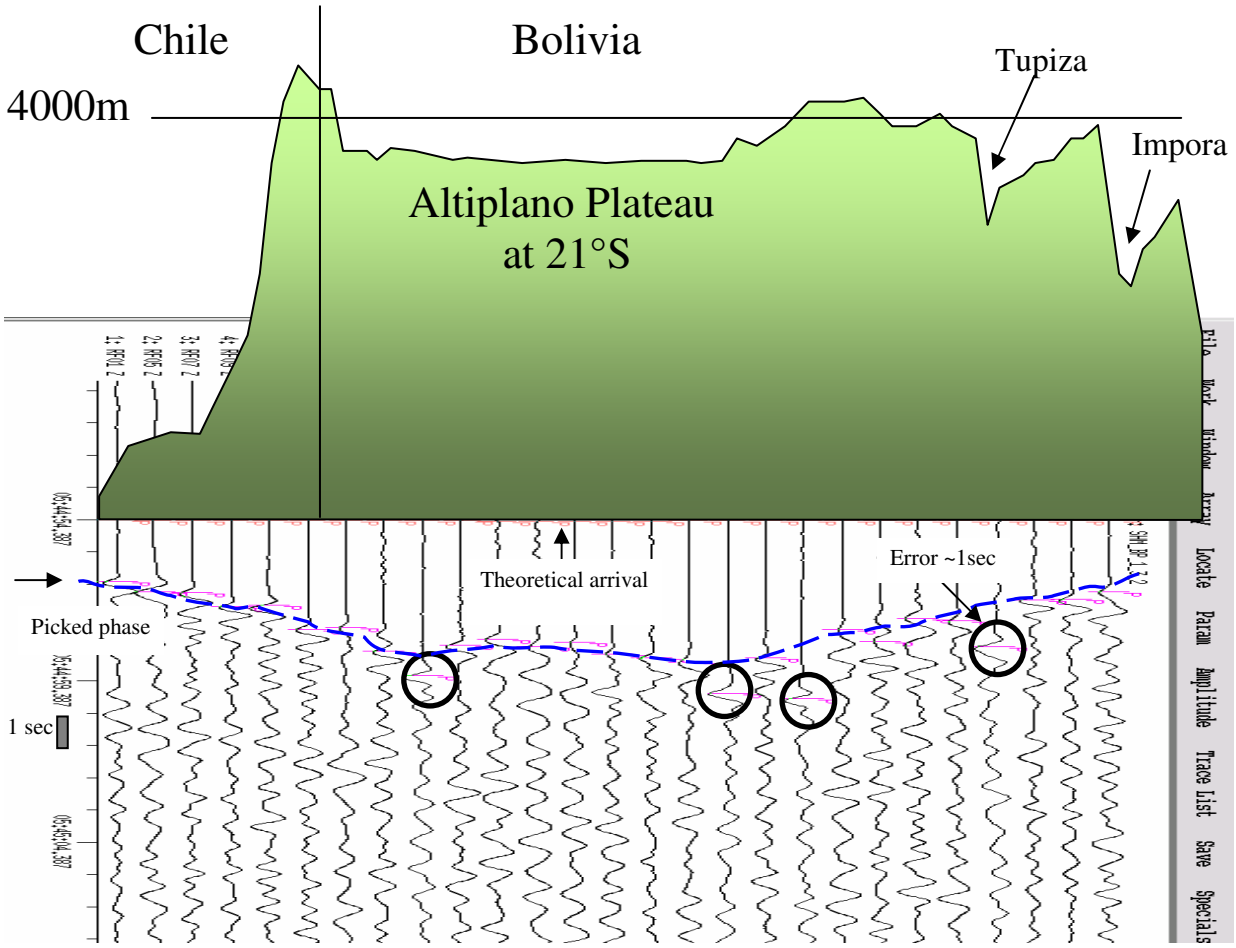

Figure 2.4: Superimposed topography related to arrival times for the Z component of P-waves showing greater delays beneath the Altiplano, where the Andes reach their greatest altitudes. Circles denote errors in real arrivals due to a Firmaware module failure. The effect of topography was corrected later (Moho and station corrections, see Chapter 3).

2.2. Installing the stations

Deploying a seismic station in the field is often not an easy task. Usually, the literature does not deal with the problems that accompany deploying stations for longer periods of time. Our experience after almost 2 years of field work is that there are specific aspects that must be considered if a project is to be concluded successfully, since a proper installation will provide better quality data for analysis. Some of the issues encountered during this project are as follows.

- In the Central Andes, the irregular topography makes the environmental conditions very harsh. Temperatures can reach 30° C or more during the day and fall to 20° below zero during the night. A 50° C difference may therefore affect the proper functioning of the

instruments if they are not installed properly. Digging holes for this purpose, up to 1 meter depth for the recording system and seismometers, helped to maintain the temperature variations within an acceptable range. In addition, the boxes that contained the equipment were provided with an extra layer of thermal isolator. Some equipment included a temperature regulator but the same precautions were always done. The batteries attached to the equipment were especially affected by decreases in temperature. It was therefore necessary to prevent this by covering the batteries with a small amount of soil.

- Strong winds may produce two undesired effects on the equipment: one is the noise (sometimes related to a deficient installation) and the other one is the fact that strong winds can alter the position of the solar panels or in some cases, cover the panels with a layer of sand. By setting the panels at a proper inclination for collecting solar energy, one may allow to be exposed to winds that can reach up to 140 km/hour in the Central Andes.

- Hard disks are sometimes prepared or sealed and recommended for use up to 9000 feet (~3000 meter). In our case, some hard disks presented problems after one year's work, so they needed to be replaced. The stations that presented this problem were those deployed above the recommended altitude above sea level. An extra number of hard disks for replacement were therefore always included in the list of field trips material.

- For the Altiplano and Puna plateaus, precipitation in form of rain and snow can normally alter the functioning of the equipment by covering the solar panels or destabilizing the position of the seismometer. With snow the problem is more dramatic as it can close the access roads for weeks or even months at a time. Special care was taken for stations that were deployed in those areas and all of them were provided them with larger hard disks, as well as digging channels for run off. We also built a well consolidated plate of concrete for the seismometer, as it may become destabilized because of the effect of precipitation.

- The presence of animals can also be a critical point. Leaving cables exposed was also avoided during the deployment.

The stations were visited periodically (i.e. 3-4 months) to avoid data loss due to hardware or software failures, strong climatic changes, etc., that affected the proper functioning of the equipment. Data quality was controlled and a backup was made in the field. These and other factors can vary if the work is carried out near a populated area (which is not the case of the Altiplano and Puna plateaus) but again the noise induced by human activity will alter the recording and quality of the data. A cartoon showing an example of the arrangement of the instruments at one station is presented as example in Figure 2.5.

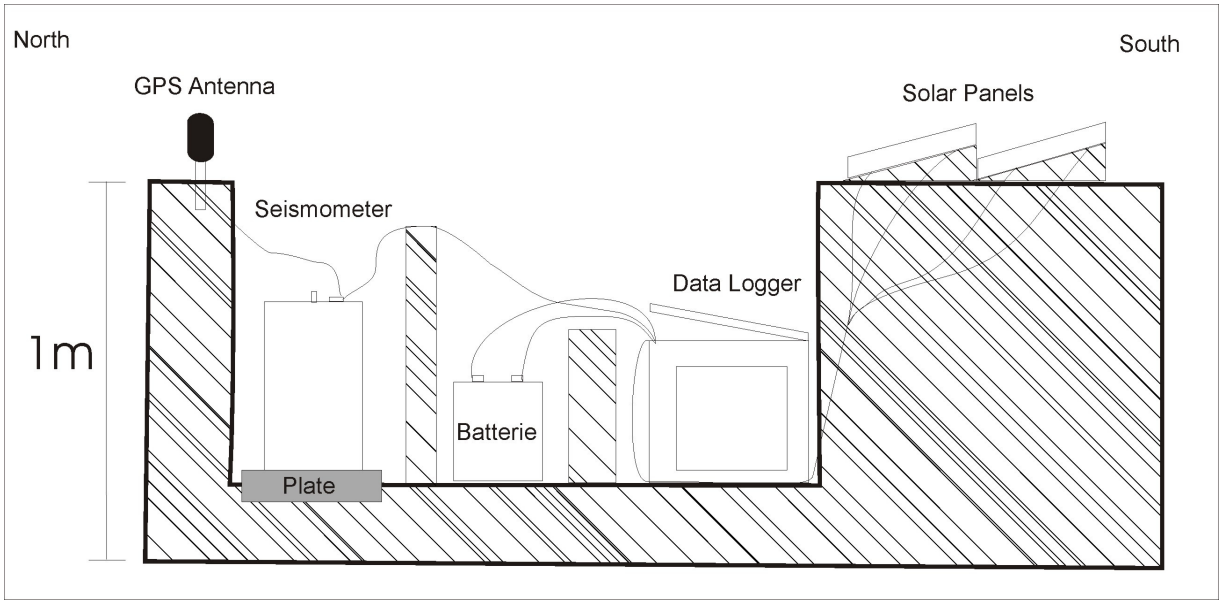

Figure 2.5: Cross section of one of our broadband stations. Solar panels inclined towards to the equator. The plate that supports the sensor was previously consolidated and is made of concrete. At least ~30 cm soil covers the instruments after installation. Superficial drainage channel for runoff has not been included here but supposes to envelope the deployment in plain view.

[1] *GEOFON is a permanent network with ~40 globally-distributed stations that permits access to seismological data via the internet to persons and institutions all over the world.*

[2] *Preliminary Determinations of Epicenters (PDE) online catalogue http://neic.usgs.gov/neis/epic/ from the National Earthquake Information Center (NEIC) that determine location and size of all destructive earthquakes worldwide*

Chapter 3

3. The Teleseismic Tomography Method

3.1. The tomographic inversion method

In geophysics, the earth can usually be described as a first approximation as an onion divided into layers whose properties (e.g. thickness, temperature and density) are responsible for other characteristics (e.g. wave propagation velocity). The number of layers for a given earth model depends upon the assumed structure of the crust, mantle and core discontinuities. There are different types of earth models that can predict the propagation of waves throughout the earth very accurately (e.g. PREM, iasp91, AK-135) and help us to produce a map that images the internal structure of the earth based on velocity variations. Calculating a travel-time anomaly relative to a reference symmetric earth model gives seismologists the possibility of detecting velocity perturbations for particular regions. One of these approaches is named *tomography* after the medical method of Computerized Tomography (CT scan) used to investigate the nature of human bodies. The word "*tomo"* from the Greek "section or slice" has been used to describe a method in which a slice from a three–dimensional (3-D) object provides information about its two-dimensional (2-D) properties. By combining many of these 2-D slices we obtain a 3-D model of the object in question (Lee and Pereyra, 1993)

Teleseismic tomography is a method that provides information about deep seismic velocity anomalies beneath a selected region based on the relative delays of seismic rays arriving from remote events at the stations located in the study area (Figure 2.1). This approach was developed in the seventies (Aki and Lee, 1976; Aki et al, 1977; Aki, K., 1993.) and has since been applied successfully to many different regions (e.g. Achauer, 1992; Evans and Achauer 1994; Koulakov et al., 1995; Wittlinger et al., 1998 and others). The first step in seismic tomography is to formulate the linearized iterative inverse problem by selecting an initial model and the parameters to describe its perturbations and tracing seismic rays through the model for given source-receiver pairs. One method uses an initial model which is a stack of homogeneous flat layers. The model parameters are the perturbations of velocities (or slowness) of the rectangular blocks into which each layer is divided. The lateral size of the model blocks is dependant upon the station spacing of the array (Aki, 1993).

In this study, we followed the same approach of teleseismic inversion as described in Koulakov et al., (2005) to investigate the mantle structure beneath the Dead Sea region. However, some peculiarities of the observation system, configuration and high contrast of the expected velocity anomalies under the Andes required some modifications to the algorithm (see Section 3.2).

The following flow chart portrays the design logic or the connection of the algorithm components and the successive steps that we have used in this process. Different items according to their characteristics (Data Base, Initial Model, Inversion Block, etc.) and their interrelations are also shown *(see diagram below and Appendix A.3.).*

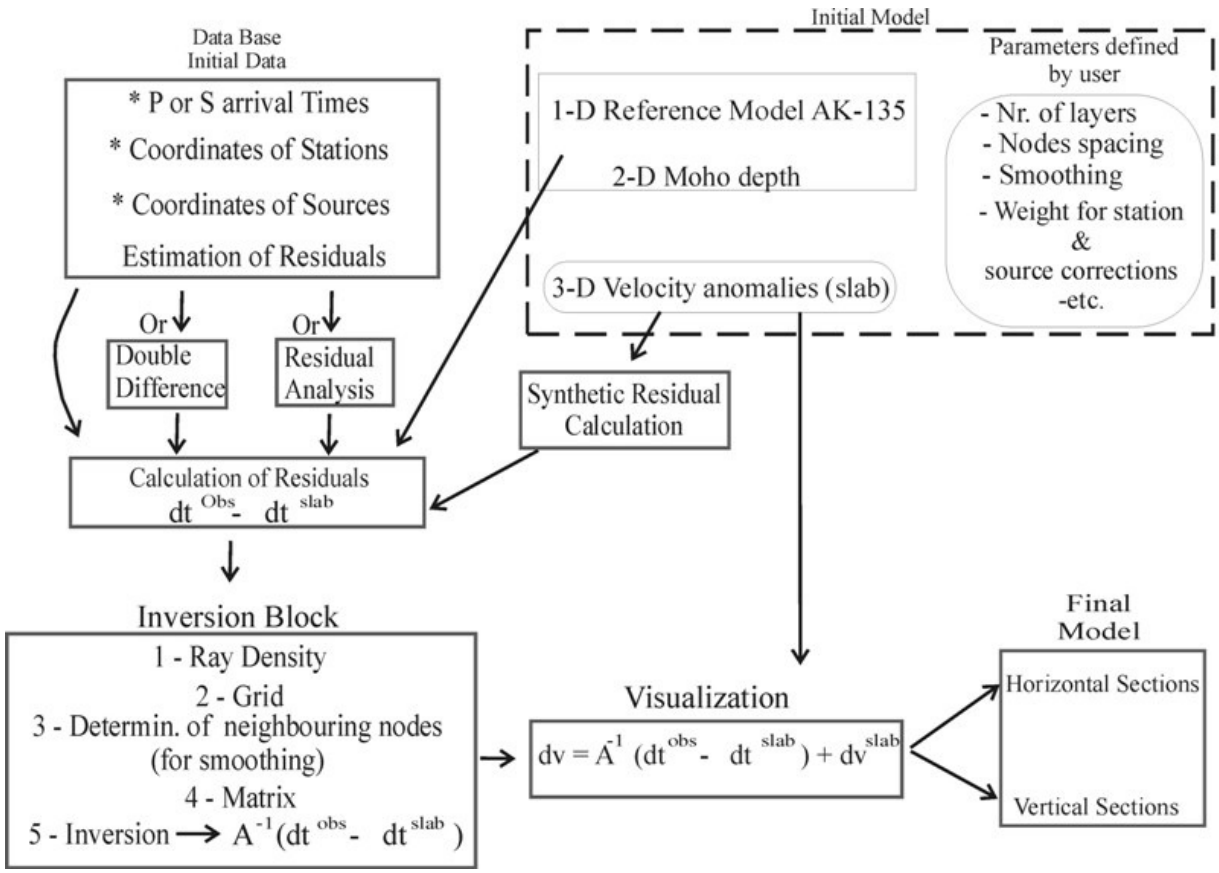

3.2. Tomographic inversion: Altiplano

As a preliminary step, the travel-times at teleseismic distances between 30° and 95°, with possibly equal step of epicentral distances are computed according to the 1D Earth model AK-135 (Kennett et al., 1995) and tabulated, from which reference travel-times of the real rays were computed. The times are corrected for the elevation of the stations above sea level by:

$$dt^{topo} = dh\sqrt{\sigma^2 - p^2}$$

where σ is slowness (1/v) in the upper-most layer, p is the ray parameter and dh is the altitude of the station above sea level.

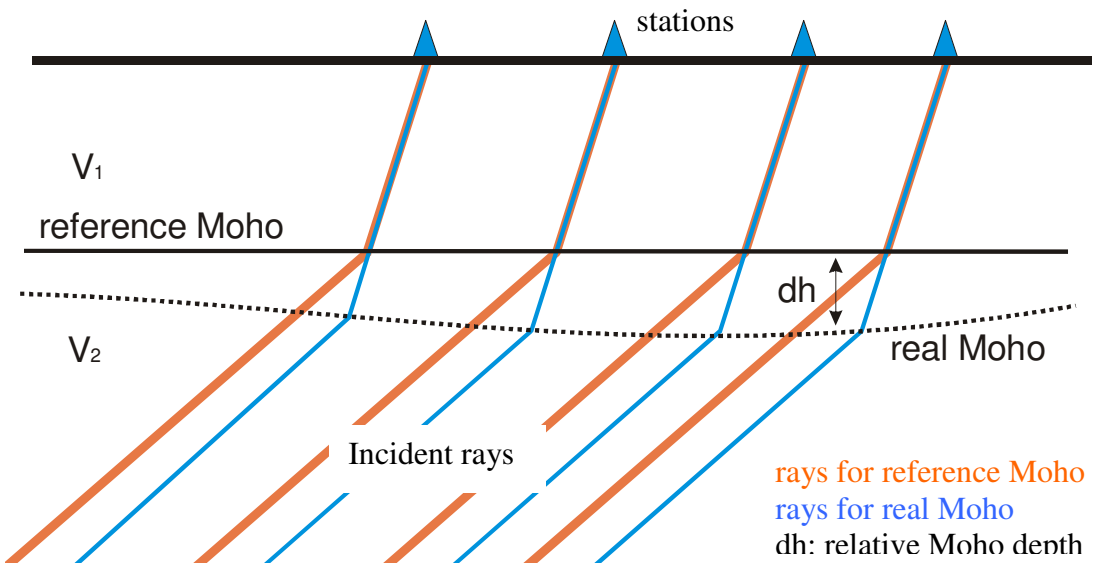

The diagram shows different rays arriving at stations with given Moho depths. Corrections are introduced when reliable data are available as in our case.

If there is information about the Moho depth available, as in the case of our study area, it can also be included as an additional correction:

$$dt^{moho} = dh \left[\sqrt{\sigma_1^2 - p^2} - \sqrt{\sigma_2^2 - p^2} \right]$$

where σ_1 and σ_2 are the values of slowness under and above the Moho interface, p is the ray parameter (horizontal component of the slowness vector), and dh is a relative Moho depth at the entry point with respect to the average crustal thickness in the reference model. In our case, for both profiles along 21˚ S and 25.5° S, the Moho depth is taken from receiver function data (Yuan et al., 2000). Figure 3.1B shows the Moho depth along the Altiplano profile at 21°S.

We do not consider the correction for the ellipticity of the Earth because the size of the study area is quite small and the ellipticity correction at all stations for one source is practically the same. It could in any case, be included in the source correction term which is obtained during the inversion step. The difference in the ellipticity corrections between the eastern and western-most stations is estimated to be below 0.01s (less than the accuracy of our phase picking) and is

included as a constant in the source corrections (see page 31).

The preliminary values of the residuals are obtained by a simple subtraction of the reference and observed travel-times. Usually, for each event, these residuals are biased due to a number of different factors: mislocation and wrong origin time of source, seismic anomalies along the ray path outside the study area, ellipticity of the Earth, non-accuracy of the reference model, etc. Most of these factors affect the travel-times in the same way from one source (e.g. anomalies in the lower mantle that are assumed to be of the same dimension than the study area), therefore the preliminary source correction is computed to provide a zero value for all residuals:

$$dt_{srce}^{0} = \Sigma_{n=1}^{N} (dt_n) / N$$

In the next step of residual processing, the source and station corrections are evaluated so that the difference between residuals corresponding to the rays with similar back azimuth and incidence angle recorded at one station were similar. The residuals that do not fit this condition were rejected as outliers. The algorithm is illustrated schematically as follows, where each vertical line means dt=0, to the left of the lines dt<0 and to the right dt>0:

Step 1 - Residuals for one event are computed so that $\sum dt=0$

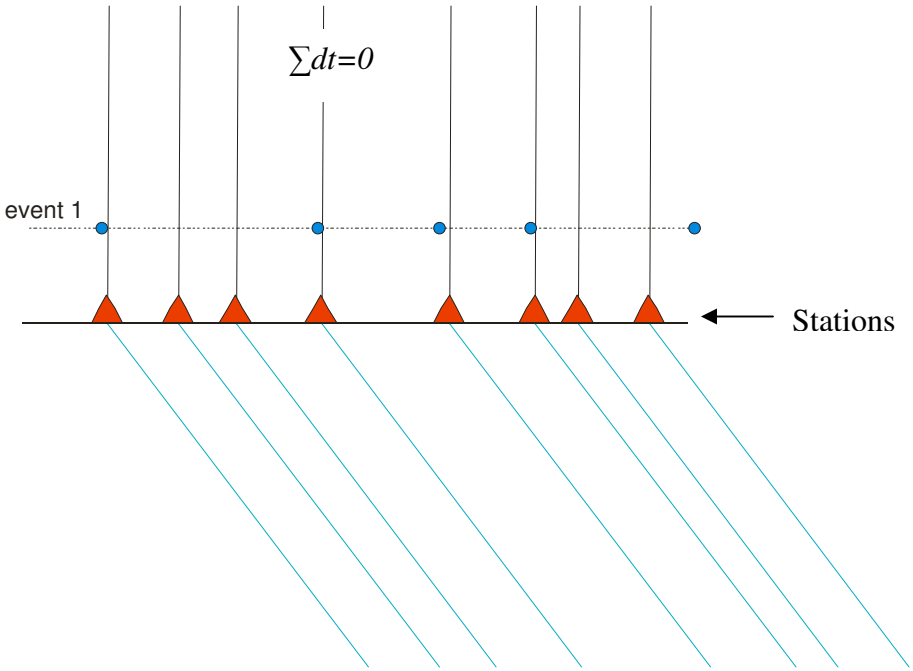

Step 2 - All events providing similar starting parameters are selected. For each event $\sum dt=0$

Step 3 - An event with maximal number of records is selected as reference

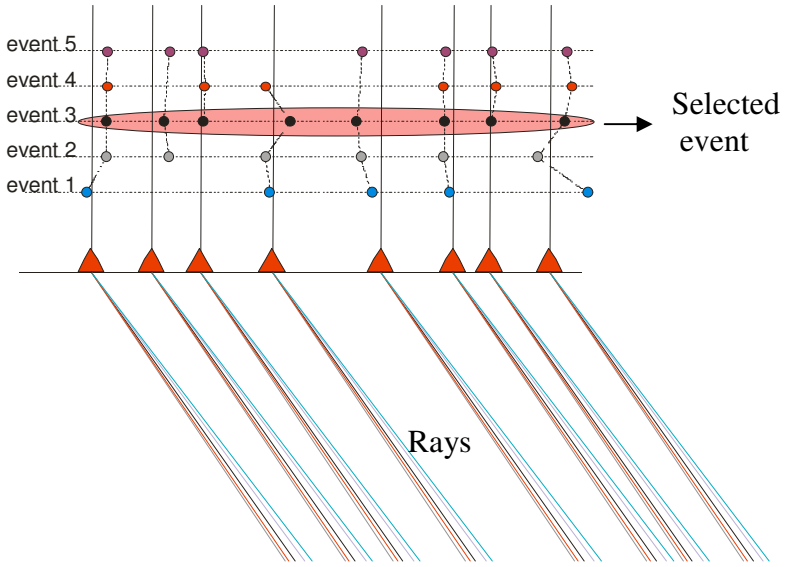

Step 4 - Source corrections are computed for the other events so that the differential residuals are minimal.

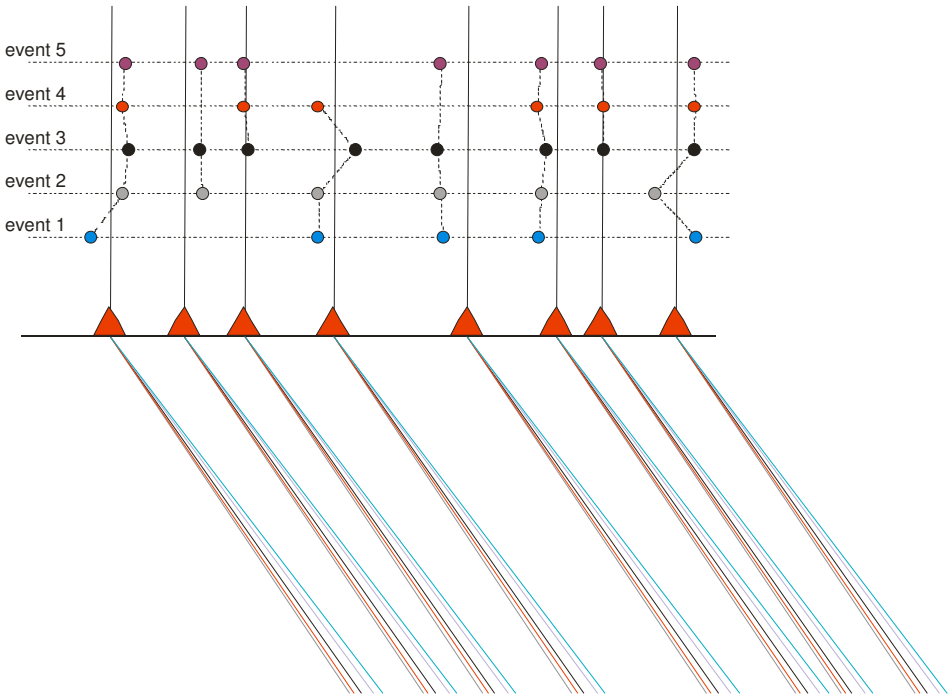

Step 5 - Records with large differential residuals are rejected as outliers.

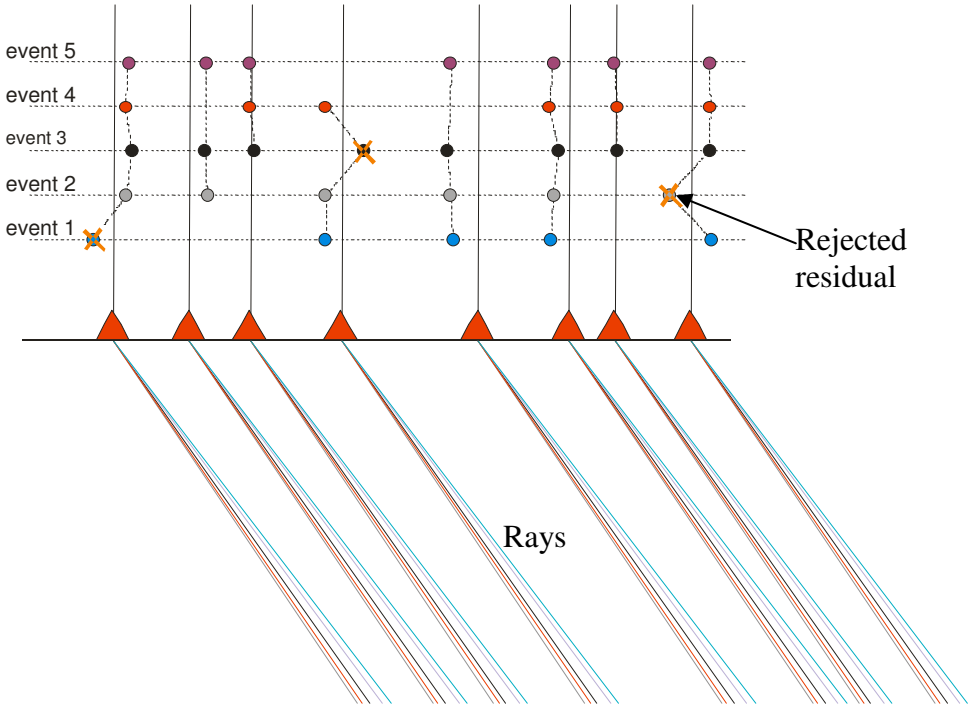

Step 6 - The procedure is repeated without the outliers

The reason for residuals described as outliers is usually related with problems in the selection of the first arrival of P- and S- waves. Other problems that influence the aspect of the residuals can be associated with timing errors due to low GPS coverage or the presence below the station of local anomalies that are not perceived in other neighbouring stations.

Average values of P-residuals for each station after this step and the ray paths of all recorded rays traced down to the depth of 320 km are shown in Figure 3.1A. In the Appendix (A.6.) the entire set of residuals is presented without the corrections according to their different back-azimuths.

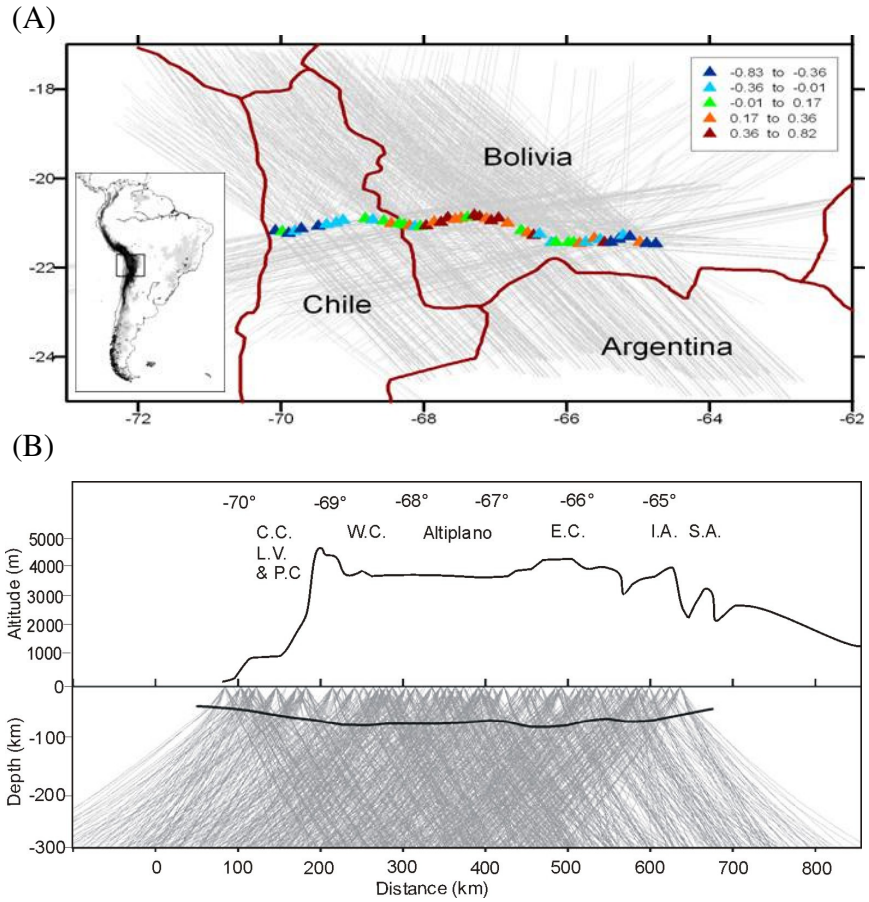

Figure 3.1: Configuration of the Altiplano seismological profile. (A): Map of the station distribution along 21°S. The colour scheme indicates the values of average residuals at the stations after corrections for topography and Moho discontinuity; positive residuals (red triangles) correspond to areas of low seismic velocities, negative residuals (blue triangles) correspond to high seismic velocities; ray paths down to 350 km are shown by grey lines. (B): Projection of the ray paths onto a vertical profile with an exaggerated topography scale along the stations profile. Morphological units along the profile are: C.C.: Coastal Cordillera; L.V.: Longitudinal Valley; P.C.: Precordillera; W.C.: Western Cordillera; E.C.: Eastern Cordillera; IA: Interandean and S.A.: Subandean. The bold black line in the vertical section shows the Moho depth (Yuan et al., 2000) used in this study to correct the residuals.

The resulting velocity model was computed in nodes of a parameterization grid distributed in the study volume according to the ray density. For the P- wave model, the uppermost level of the study volume was defined from 20 km as the minimum depth that is where a sufficient number of ray intersections between neighbouring stations occur. The bottom limit was fixed to 320 km depth, which is compatible with the length of the profile. The parameterization nodes consisted of 10 horizontal planes located at depth steps of 30 km. Examples of the grid construction according to the ray density at various depth levels are shown in Figure 3.2. To avoid an excessive concentration of nodes in the area of ray fluctuations, we fixed the minimal distance between the nodes at 25 km. Velocity distribution between nodes is defined using a bilinear

interpolation method. The number of nodes at each level depends upon the value of the fixed minimal spacing and varies from about 70 at the shallowest level to 100 at the deeper levels.

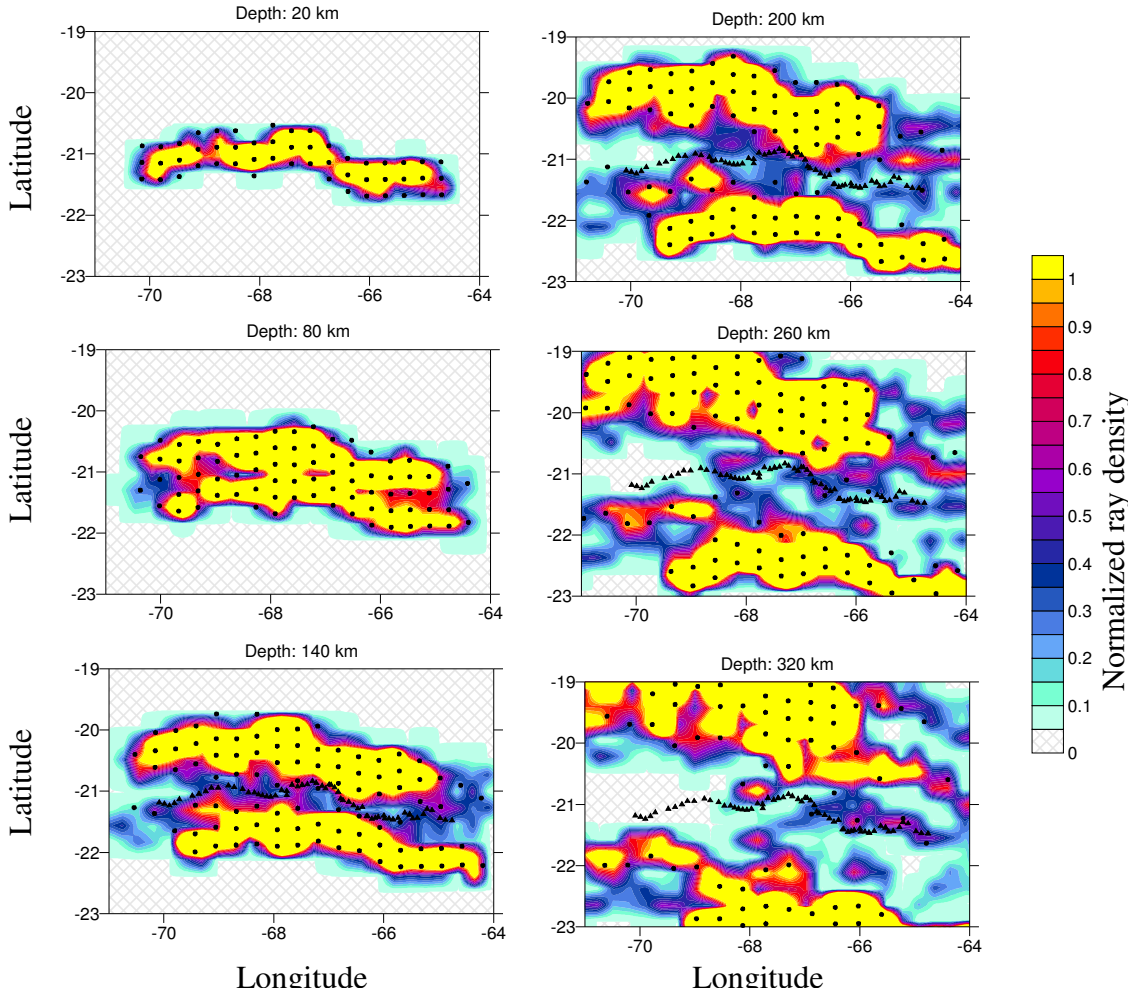

Figure 3.2: Examples of the grid construction according to ray density at various depth levels. Note the influence of the rays for depths greater than 200 km lack the resolution beneath the stations along the profile (Black triangles display the station locations when the rays start to split in their incidence angles from north and south). Colours show normalized values of the ray density.

For the S-wave model, and due to a significantly smaller number of observations, the parameterization grid was sparser than for the P- wave model. The nodes were distributed at 10 horizontal levels down to a depth of 320 km with steps of 30 km. The minimal distance between the nodes was 40 km and the number of nodes varied from 30 at the shallowest plane to 40 in the deepest one.

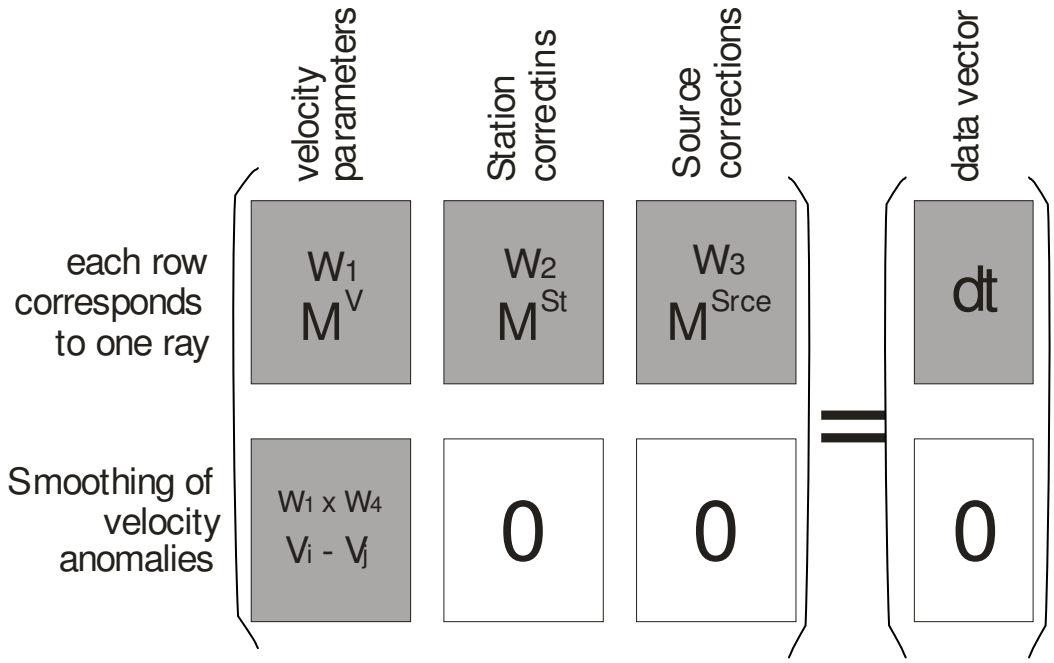

The structure of the matrix used to determine the velocity field and the source and station corrections is shown in the diagram above. The matrix elements responsible for the velocity variations, M^v, are computed on the basis of the ray segments located in the study volume. We use the ray paths computed using the 1D spherical-velocity model. For any point of a ray, eight nodes of the parameterization grid are selected, so that they form a parallelogram that contains the current point. Velocity inside the parallelogram is interpolated bilinearly. The elements of the matrix are computed as:

$$M_{ij}^{Vgp(s)} = -\frac{1}{\Delta V_j^{p(s)}} \int_{\gamma_i} \frac{\Delta U_j(s)}{V_0^2(s)} ds$$

where *i* is the ray number (row of the matrix), *j* is the parameter number (column of the matrix), γ_i is the ray path, S is a point on the ray, $\Delta V_j^{p(s)}$ is the unit velocity variation at the *j*-th node, $\Delta U_j(s)$ is the velocity variation at the current point of the ray due to velocity variations at the j-th node and $V_0^2(s)$ is the reference velocity at the current point.

An additional block of the matrix allows the regularization of the smoothness of the obtained 3D velocity distribution. Each row of this block contains only two non-zero elements with opposite signs that correspond to parameters in the neighbouring nodes. In this block, the data vector is

assigned zero.

The source corrections, M_{srce}, include all factors that affect the travel-times between the source and entry point of the study volume; e.g. mislocation and wrong origin time of the source, seismic anomalies along the ray path outside the study area, ellipticity of the Earth, inaccuracy of the reference model, etc. In each row of the matrix, there is one element responsible for the source correction, M_{srce}, which is constant and equal to 1.

The station corrections include all the unaccounted factors between the station and the upper limit of the study volume: velocity heterogeneities in the crust and in the uppermost mantle, Moho depth, sediments etc. Station corrections are determined using additional elements in every row of the matrix, $M_{st} = 1$.

The weight of the different parameters is controlled using four tuning parameters; W1 for the amplitude of the velocity model, W2 for the station correction, W3 for the source corrections and W4 for the tuning of the smoothness of the velocity model. The determination of these parameters is nevertheless an ambiguous and delicate problem. For example, increasing the role of station corrections causes the smoothing of the anomaly amplitudes in the uppermost part of the study area. Varying the source parameters can change velocity distribution in the lower part, although in practice those changes are not dramatic. All of these coefficients are estimated using a-priori knowledge about the expected values of the unknown parameters and the results of the synthetic tests.

3.2.1. Synthetic tests: Altiplano

The synthetic test is a very important step, which is performed in parallel to the real data inversion. By executing a synthetic test, it is possible to explore vertical and horizontal resolutions that provide essential information about the trustworthiness of the features in the final inversion of the real data. On the other hand, synthetic tests also provide optimal estimations of the parameters used for the real data inversion.

Here we present results for two types of tests, namely for horizontal and vertical anomalies, that

aim to reconstruct the presence of realistic anomalies expected in the study area (e.g. intra-crustal, lithospheric features and the slab). The synthetic tests are performed using the same geometry (earthquake/stations) as in the case of the real data set.

3.2.1.1. Horizontal tests

To check the capacity of the algorithm to reconstruct horizontal anomalies we performed the following tests using different-shape bodies to simulate the anomalies as shown in Figure 3.3. Data without noise is used to check the theoretical capacity of the observation system to reconstruct given anomalies. The anomalies are represented as prismatic bodies maintaining their shapes from the surface to a depth of 200 km

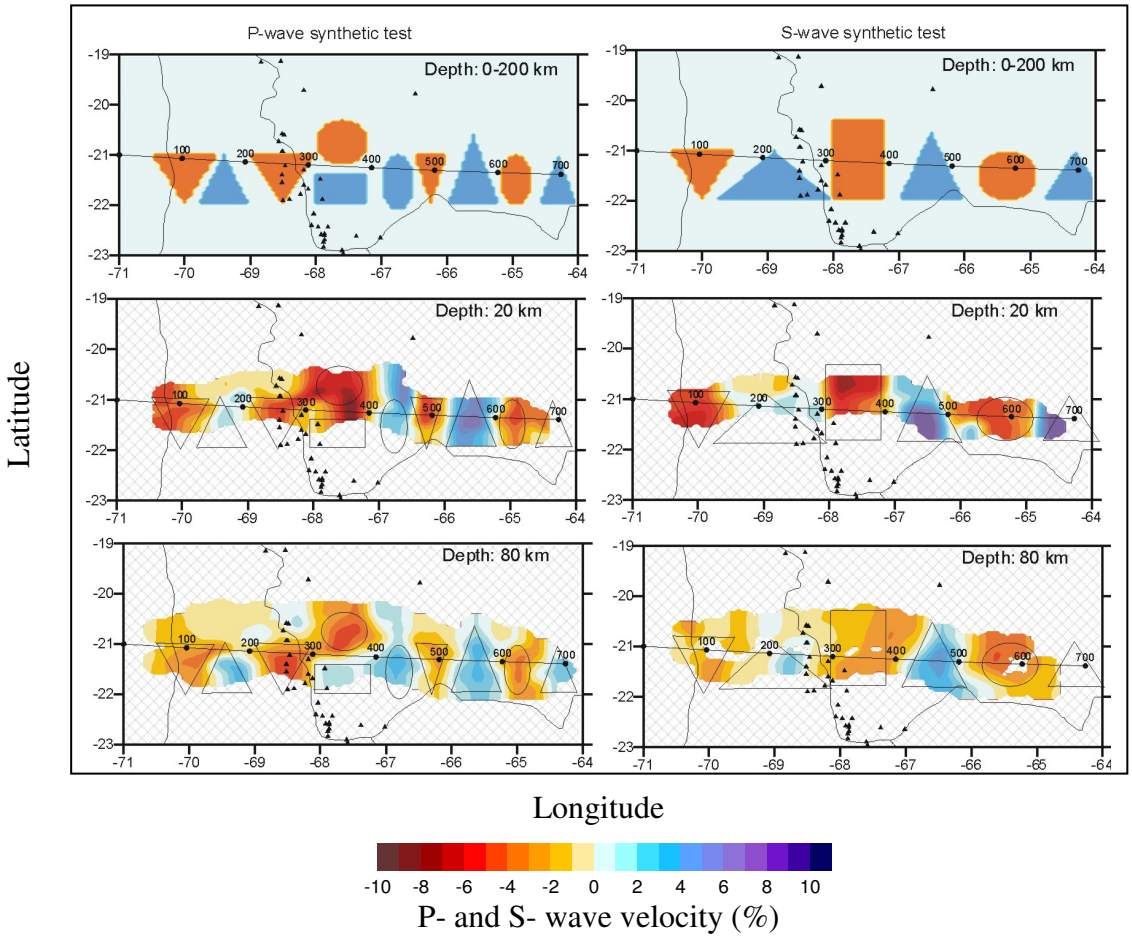

Figure 3.3: P- and S- wave horizontal synthetic anomalies (upper figures) for two depths (20 and 80 km) as an example of the resolution capacity of the algorithm. Inverted red triangles and circles represent low-velocity anomalies in the volcanic arc with amplitude of -4%; blue circles and triangles represent high-velocity units in the fore-arc, Altiplano and Eastern Cordillera with adjoining parts of the Brazilian Shield (+4%). The straight line represents the trace of the profile at ~21°S. Black triangles are volcanoes and the contour lines are political borders.

The horizontal synthetic tests show that the position of the anomalies can be well reconstructed, but their shapes are not well defined. Some features at both ends of the profile in the upper section (less than ~20 km) are ill resolved due to the absence of incident rays that appear in the successive depth steps. For more examples of synthetic tests see the Appendix where other anomaly shapes are used to evaluate their reconstruction (Appendix A.4.).

3.2.1.2. Vertical tests

The initial anomalies in this tests, described in Figure 3.4A, include a slab-shape anomaly with an amplitude of 4% and three crustal anomalies that represent a high-velocity block in the fore-arc (+6%), a low-velocity block of the Altiplano in the centre (-10%) and a high-velocity block in the East which models the position of the Brazilian shield (+4%). The residual times for these tests are computed along the real rays as:

$$dt = \int_{\gamma} \Delta\sigma(\gamma) dS + \tau^{stat} + \tau^{srce} + \varepsilon$$

where $\Delta\sigma(\gamma)$ is a perturbation of the slowness in the initial synthetic model at a point of the ray, τ^{stat} and τ^{srce} are the station and source terms, respectively, and ε is the random noise. Station and source terms are defined as:

$$\tau_i = ab_i$$

where a is a constant providing a predefined standard deviation of the corrections and b_i are random numbers. In our case, we used a periodic repetition of the following seven numbers: 3, -1, 2, -2, 1, -3, 0 which are normalized with a coefficient k that provides a predefined value of standard deviation for station corrections. The random noise ε is produced by a random number generator which provides a statistical distribution similar to that of the real residuals with a predefined average amplitude.

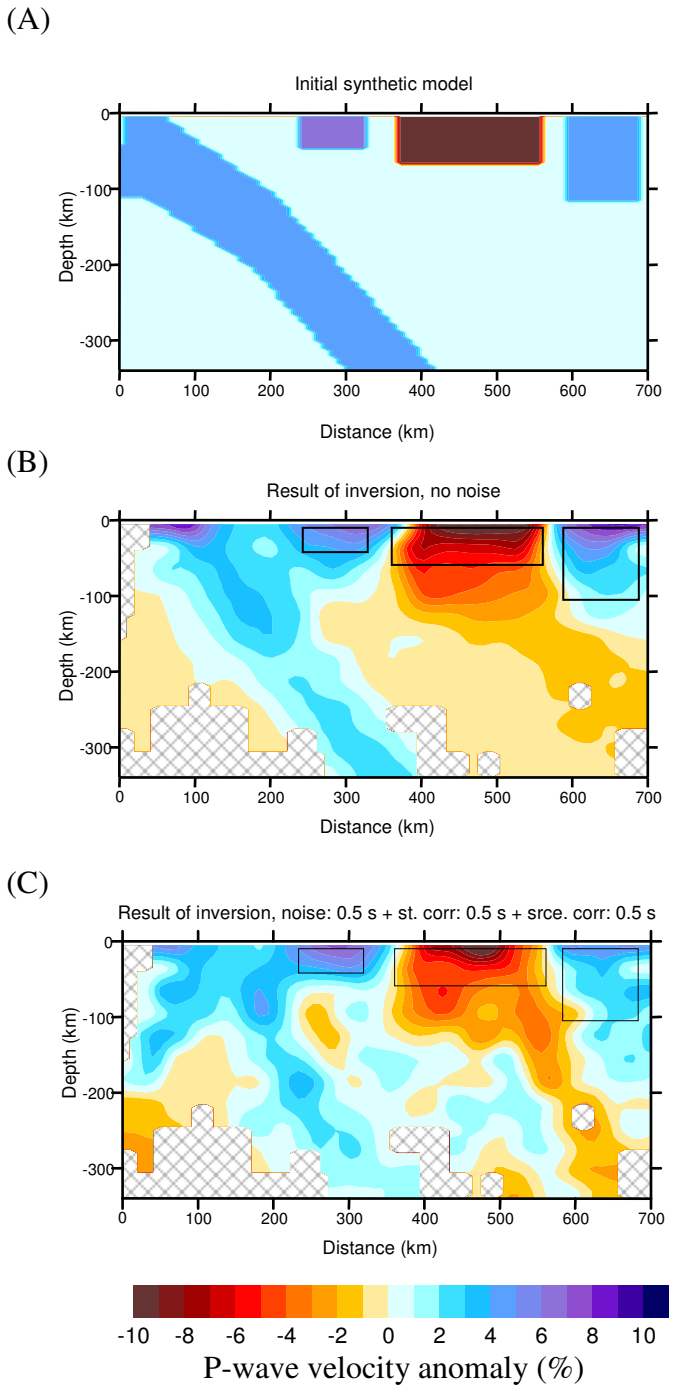

Figure 3.4: Vertical synthetic test showing the results for the reconstruction of synthetic anomalies with rays corresponding to the real data set. (A): Shape of the initial anomalies. (B): Reconstruction using the data without noise. (C): Reconstruction from data with noise. The average noise level is 0.9 s.

Carrying out the inversion without considering noise (Figure 3.4B) shows the algorithm's theoretical capacity to reconstruct the pre-defined shape of the anomalies. In this case, resolution is only limited by the ray coverage and parameterization spacing. This test shows that, despite

the high value of variance reduction, 92%, the teleseismic inversion provides fairly poor vertical resolution, in that not even the noise-free inversion shows a clear lower limit for the crustal blocks due to smearing. Greater vertical smearing is observed towards the eastern boundary of the profile, at depths between 100-300 km. Noisy data and related smearing are shown in Figure 3.3C with noise including station error (0.5 s of deviation), source error (0.5 s) and randomly distributed error (0.5 s). The summary standard deviation of this noise was as large as 0.9 s. Judging from the variance reduction obtained in this test (41%), this noise level is higher than in the real data set (60 % of variance reduction). This means that even a test with lower quality data (41%) than the real data (60%) still provide a reliable reconstruction of anomalies. The horizontal positions of the main anomalies are reconstructed correctly, although the vertical resolution is again disappointing.

3.2.1.3. The slab beneath Altiplano

Due to the poor resolution of the slab in the vertical section, it is necessary to analyze this outcome in detail as it must be considered in the next step of real data inversion. We have the possibility to improve the image of the slab as we use earthquake hypocenters to constrain a realistic shape of the subducted oceanic lithosphere. It should be noted that the slab in the vertical test above was much steeper than what we could observe from the distribution of intermediate depth seismicity in the study region. In the next test we attempt to reconstruct the realistic shape of the slab (Figure 3.5). The initial shape of the slab is shown in Figure 3.5A where the upper surface of the slab is defined as an envelope of the seismicity (hypocenters) located by Engdahl et al. (1998).

The thickness of the oceanic lithosphere was fixed at ~100 km according to a worldwide plot of age versus thickness for oceanic lithosphere from Turcotte and Shubert (1982). The reconstruction of the slab using the data without noise shows the limited capacity of the teleseismic algorithm to reconstruct such kinds of anomalies, which in our case, is strongly shifted upwards (Figure 3.5B). At the same time, the variance reduction after inversion proved to be 97%, meaning that, the initial and reconstructed anomalies provide practically the same values of residuals along the rays used in the data set. This fact can be used to test the effect of the slab anomaly on the interpreted data by reducing the influence of some parameters so that they can be evaluated from independent information during the real data inversion.

Additional vertical and horizontal synthetic tests for the Altiplano profile are presented in the where the results for P- and S- waves are given separately (Appendix A.4.)

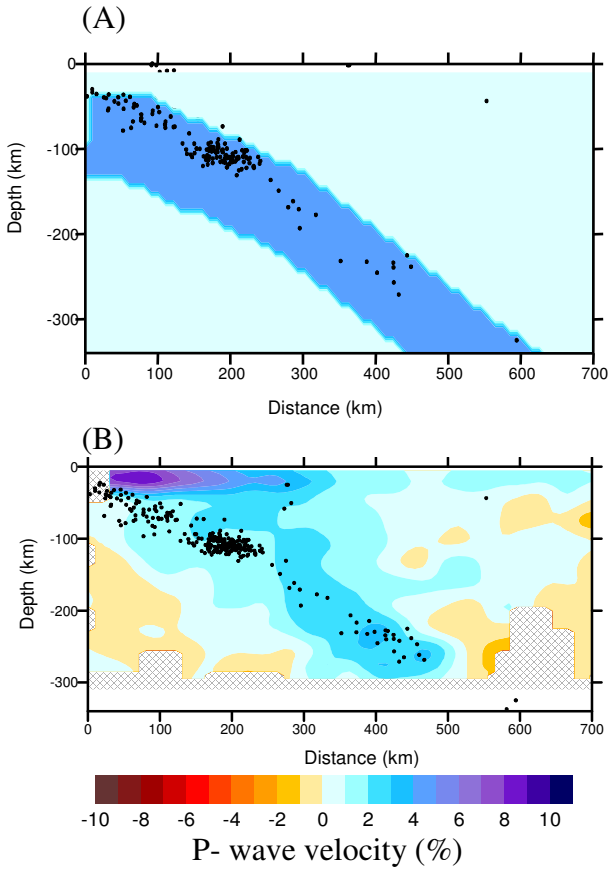

Figure 3.5: Synthetic test showing the poor capacity of the teleseismic approach to reconstruct the real shape of the slab. (A): Initial position of the slab. Earthquake hypocenters are taken from Engdahl et al. (1998). (B): Result of the reconstruction using data without noise, which provides 97% of variance reduction.

It is important to note that the slab, as with any sub-horizontal structure, cannot be reliably recovered. Not all rays reach the receiver by passing through the slab, so that the information about anomalies below, inside and above the slab is confusing. This effect is normally seen in the middle of the slab, where the centre is eviscerated and the ends are well modelled (Figure 3.5B), (Evans and Achauer, 1993).

3.2.2. Real data inversion: Altiplano

The poor resolution of the teleseismic inversion for reconstructing the slab-shaped anomaly shown in the previous test suggests that we will be unable to obtain a clear image of the slab from our data set. However, the a-priori information about the position of the slab can be used to

subtract the effect of the slab from the real data inversion. The formalism used to subtract the effect of the slab needs some additional explanations. The possibility of effecting such a subtraction is based on the linearity of the inverse and forward tomographic operators. It is, however, possible to do so if the values of the subtracted anomalies are not too large, so that they do not significantly change the trace of the ray paths. In linear approach, the inversion is performed on the basis of the rays constructed in the reference model (usually a 1D model).

The definition of a linear inversion operator A^{-1} is:

$$A^{-1}(X+Y) = A^{-1}(X)+A^{-1}(Y). \quad (1)$$

The operator of teleseismic tomographic inversion is assumed linear, so that:

$$dv_1=A^{-1}\, dt^{obs} \quad (2)$$

and

$$dv_3 = A^{-1}(dt^{obs} - dt^{slab})+A^{-1}(dt^{slab}). \quad (3)$$

are equal. The correspondence between $dv_1 \sim dv_3$ is illustrated in the Figure 3.6 (A and C). If we now apply a direct linear tomographic operator to these two velocity models, we obtain the following residuals:

$$dt_1 = A[dv_1]=A[A^{-1}\, dt^{obs}] \quad (4)$$

$$dt_3= A[dv_3]= A[\, A^{-1}(dt^{obs} - dt^{slab})]+A[A^{-1}(dt^{slab})] \quad (5)$$

which should also be equal; that is $dt_1 = dt_3$.

At the same time, in the synthetic test with reconstruction of the slab, we have shown that the variance reduction of such an inversion is 97%. This means that equation 5 may be rewritten as

$$dt^{slab} \sim A\,(A^{-1}\, dt^{slab}) \quad (6)$$

with an accuracy of 3%. However, we should note that

$$dv^{slab} \neq A^{-1}\, dt^{slab} \quad (7)$$

and that due to the poor vertical resolution, the slab is smeared upwards. If instead of the second

term in (3) we use dv^{slab}, we obtain a new velocity model:

$$dv_4 = A^{-1}(dt^{obs} - dt^{slab}) + dv^{slab} \qquad (8)$$

which is obviously not equal to dv_2 (due to the inequality shown in (7)). At the same time, the residuals after application of the direct tomographic operator because

$$dt_4 = A[dv_3] = A[A^{-1}(dt^{obs} - dt^{slab})] + A[dv^{slab}] \qquad (9)$$

and are approximately equal to dt_2 in (5) with an accuracy of 3% (97% of variance reduction). This means that three velocity models, dv_1, dv_2 and dv_3, provide similar residuals and therefore can be equally used to explain the observed residuals dt^{obs}. Since the approximate shape and amplitude of the velocity contrast of the slab present in our study area are known, this information can be used in our starting model. Hence, dv_3 in our case is the most realistic interpretation.

The result of the inversion of the initial observed residuals, dv_1, according to (2), is shown in Figure 3.6A. The high-velocity anomaly above the earthquake cluster apparently reflects the position of the slab shifted upwards because of the poor vertical resolution, as demonstrated in Figure 3.5. In the Figure 3.6B we present the results of the inversion for the residuals after subtracting the effect of the slab, $dv^{noslab} = A^{-1}(dt^{obs} - dt^{slab})$. The amplitude of the P- wave velocity anomaly in the slab was assumed to be 6%. In Figure 3.6C we present the final result which is a combination of the model presented in Figure 3.6B and the initial slab anomaly, dv^3, according to (3). In Figure 3.6D the model shows the combination of results of inversion for as dv^4 in (8)

Due to the linearity of the inversion operator A^{-1}, the difference in the residuals produced by the models dv_1 and dv_3 is only related to the difference between residuals computed in the reconstructed and initial slab models shown in Figure 3.5. Because the variance reductions from dv_1 and dv_3 are equivalent, both models can equally be used for explaining the observed residuals. However, the third and forth models (Figure 3.6C and D) appears to be more reasonable since it takes into account the a-priory position of the slab.

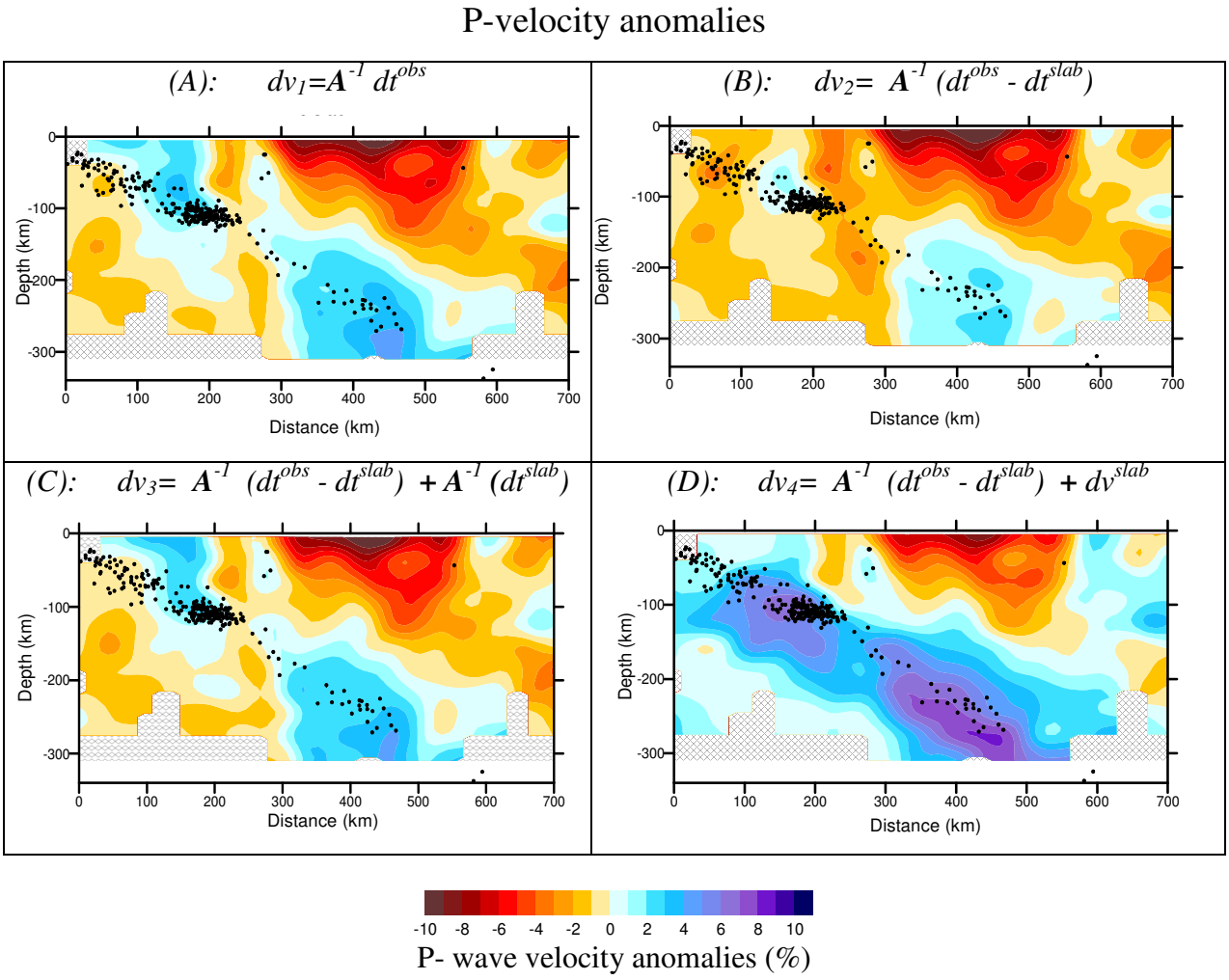

Figure 3.6: Results of the inversion for P-wave residuals with and without a-priori information, presented as vertical sections. (A): Inversion of the observed data for a 1D model. (B). Inversion of the observed data without slab residuals (C): Superposition of the inversion results for "no-slab" residuals with the addition of slab residuals. The models A and C are equivalent when explaining the observed residuals, but C contains a-priori information from the slab. (D): the final section showing the combination of the inversion results for "no-slab" residuals with the model for the slab.

The same strategy as for P- waves was applied for the inversion of the S- wave data. The total number of S- wave residuals (500) was significantly smaller compared to the P- wave data set (1500 rays) and might therefore show a lower resolution. Nevertheless, the results shown in Figures 3.7A, 3.7B and 3.7C, allows us to be optimistic about the reliability of the obtained patterns. As for the P-model, we performed the inversion with and without subtracting the effect of the slab. In the initial model, we used the slab with a velocity contrast of 4%. The results of the P- and S- wave real data inversion are presented as horizontal sections in the Appendix A.5.

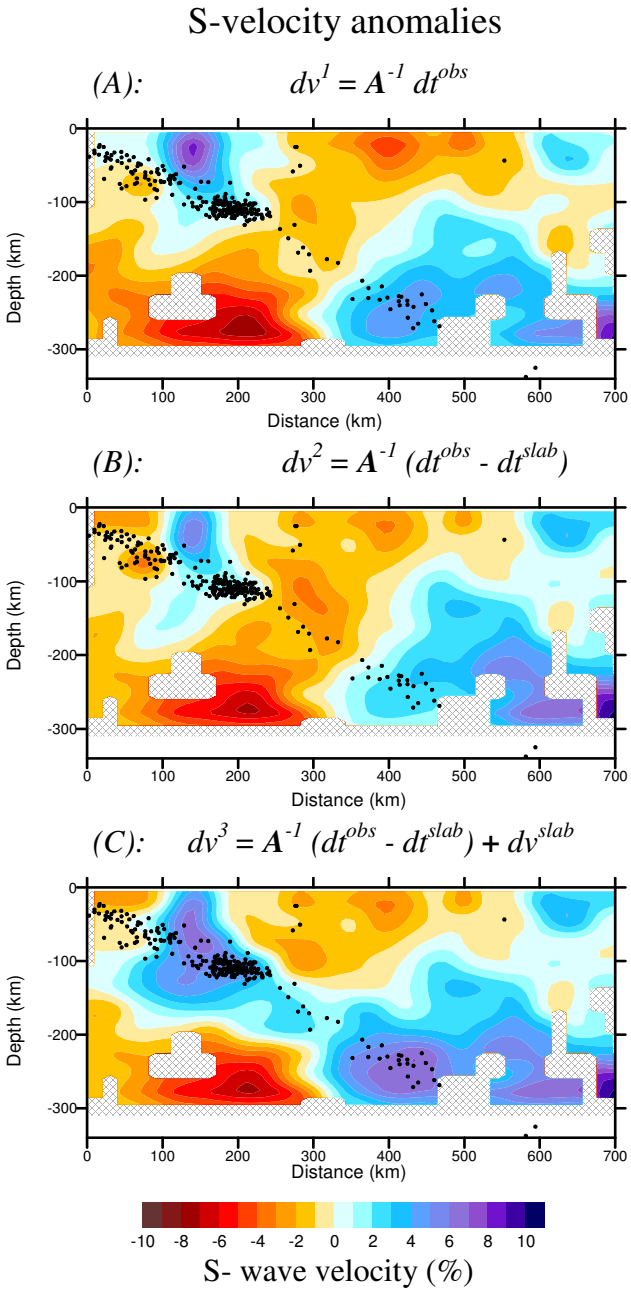

Figure 3.7: Results of the inversion for S- wave residuals with and without a-priori information (vertical sections) using the same strategy as shown in Figures 3.5 and 3.6. The smaller number of detected S- waves is reflected in the poor resolution of anomalies such as the slab. Nevertheless, it is still possible to recognize zones of low-velocity in the upper crust that are not clearly defined by the P- wave inversion.

3.3. Tomographic inversion: Puna

The same procedure as for the Altiplano was applied to the southern profile of 19 stations in the Argentine Puna. The stations were corrected for elevation above sea level and Moho depth along the profile. Average values of P-residuals for each station and the ray paths of all recorded rays

traced down to a depth of 260 km are shown in Figure 3.8, (in the Appendix, the residuals are presented without correction according to their back-azimuth – *A.6.*). The resulting velocity model was computed at the nodes of a parameterization grid distributed in the study volume according to ray density. Digital *P*- waveforms from 177 teleseismic events and 29 *S-waveforms* with $Mw \geq 5$ were used to obtain the tomographic images.

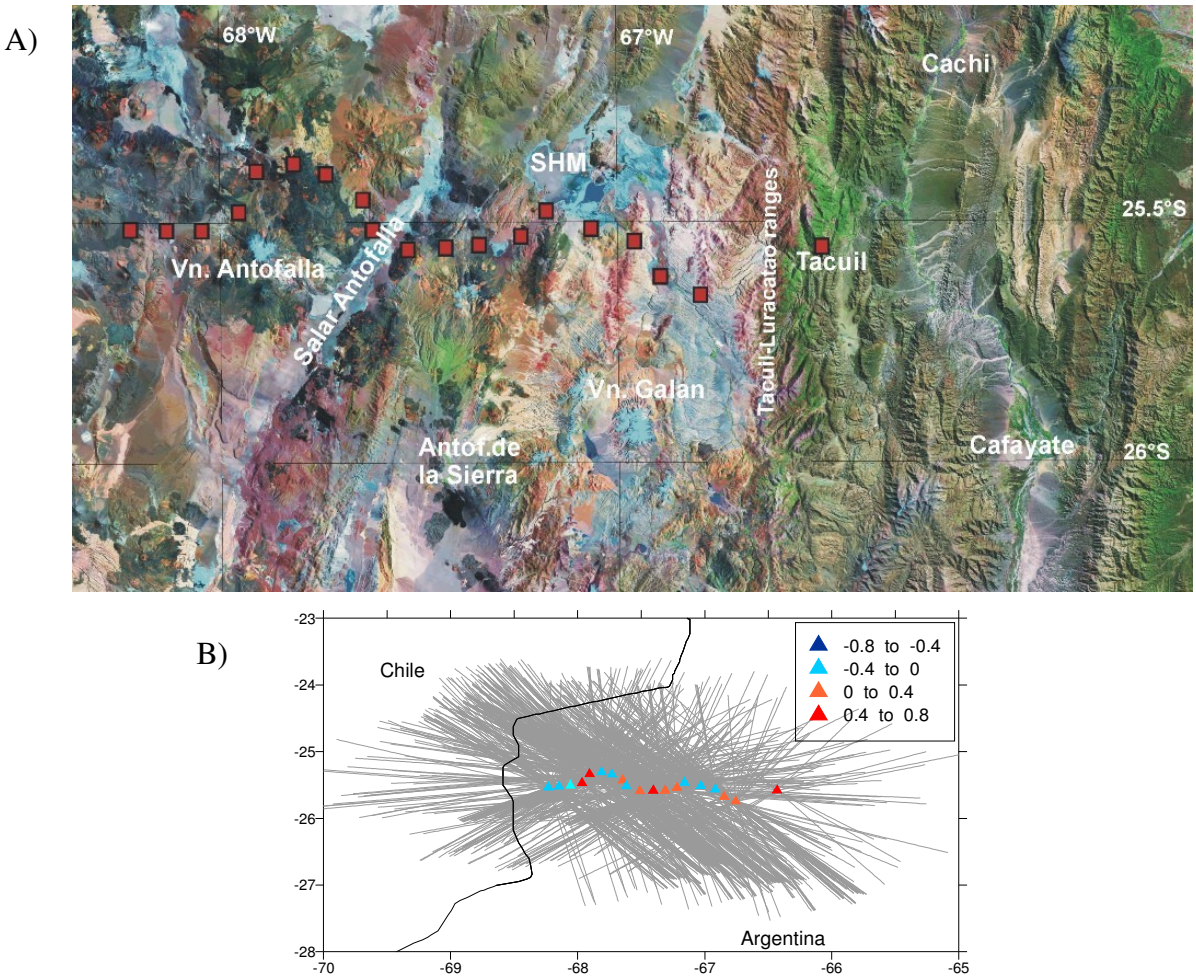

Figure 3.8: A: Landsat image showing the station distribution (red squares) as well as the position of the two prominent volcanic edifices along the profile (Vn. Antofalla and Vn. Galan volcanoes). B: Different colour triangles represent the average-residual values at the stations after corrections for topography and Moho depth; positive residuals (red triangles) correspond to areas of slow seismic velocities and negative residuals (blue) to fast relative velocities; ray paths are indicated by grey lines.

For P- and S- wave models, the uppermost level of the study volume was defined at 20 km depth, where sufficient intersections of rays from neighbouring stations are detected, with the lower limit fixed at 200 km depth. The parameterization nodes were constructed at 9 horizontal planes, located at depth steps of 30 km.

Examples of the grid construction according to the ray density at various depths are shown in Figure 3.9. To avoid an excessive concentration of nodes in the area of ray fluctuations, the minimal distance between nodes was fixed at 25 km. Velocity distribution between nodes is defined by bilinear interpolation. The number of nodes at each level depends on the value of the fixed minimal spacing and varies from about 20 at the shallowest level to 80 at the deeper levels. The same procedure was followed for S-wave velocity model.

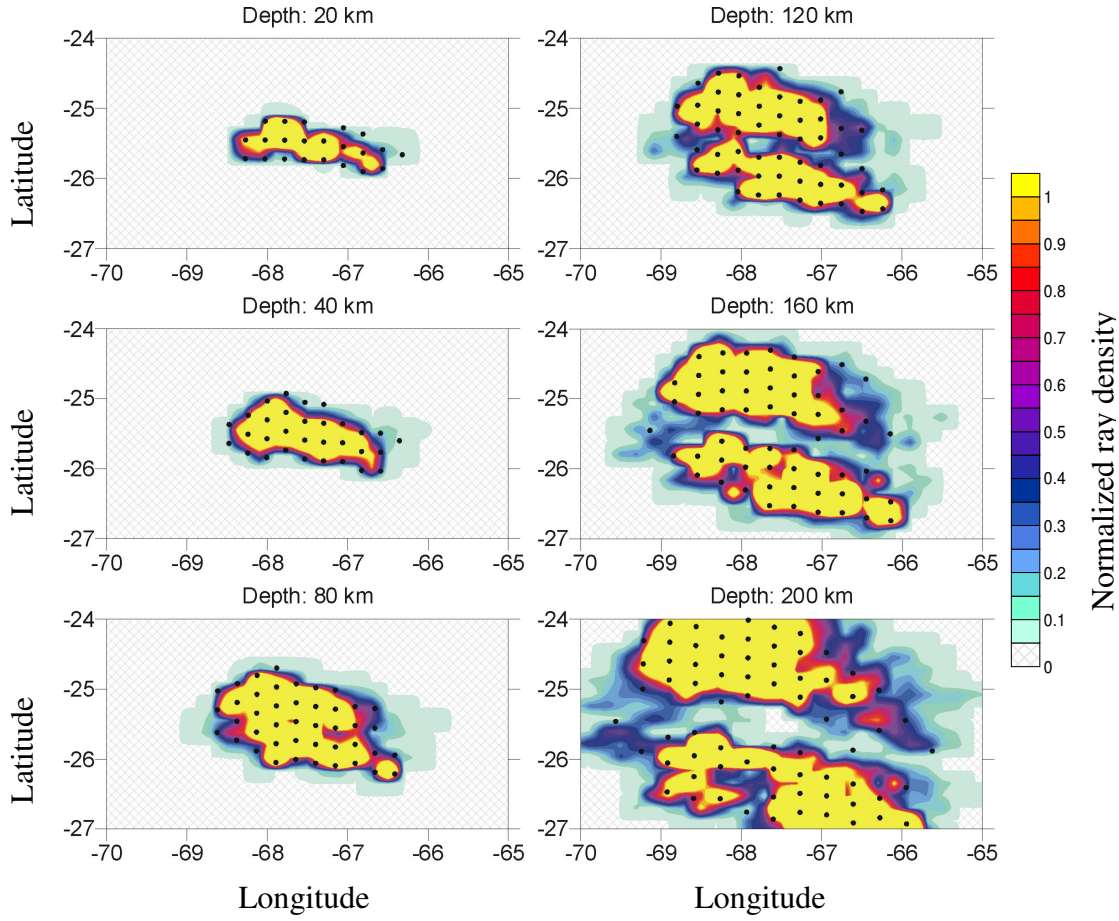

Figure 3.9: Ray density and parameterization grid for Puna profile. Colors show normalized values of the ray density

3.3.1. Synthetic tests: Puna

As mentioned before the synthetic tests are very important to explore vertical and horizontal resolutions and provide optimal estimations of the parameters used for the real data inversion. The synthetic tests are performed using the same geometry (earthquake/stations) as in the case of the real data set. The general procedure for the Puna synthetic tests follows that for the Altiplano explained in more detail in section 3.2.1.

3.3.1.1. Horizontal tests: Puna

To check the algorithm's ability to reconstruct horizontal anomalies, we performed the following tests using different-shaped bodies to simulate the anomalies, as shown in Figure 3.10. The anomalies are represented by prismatic bodies that conserve their shape form the surface to a depth of 200 km.

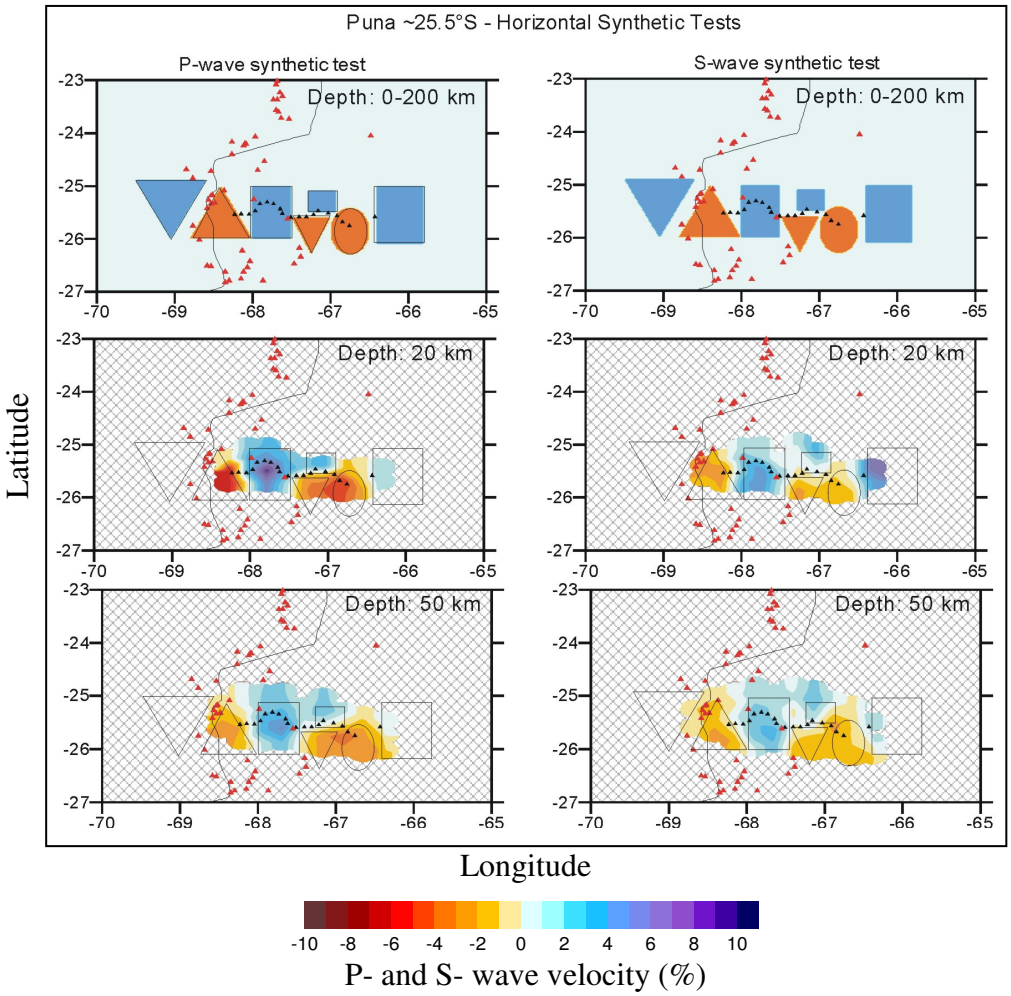

Figure 3.10: P- and S- waves horizontal synthetic anomalies (upper figures) for two depths (20 and 80 km) as an example of resolution capacity of the algorithm. Orange figures (triangles and circles) represent low-velocity anomalies as the volcanic arc with amplitude of -4%; blue squares represent high-velocity units in the fore-arc, Puna plateau and Eastern Cordillera. Black triangles represent stations at ~25.5°S. Small red triangles are volcanoes. Contour line: political border between Argentina and Chile (see Fig.3.8B).

The synthetic test results show that the position of the anomalies is well reconstructed. The shape of the figures, however, remain not so well constrained, but considering the small number of stations and the length of the profile (~200 km), it is still possible to detect the anomalies at depth. In the upper section, some features that are located at both ends of the profile (west and east) are not resolved due to the absence of incident rays. In this case, it is impossible to make

assumptions about regions in the fore-arc as was done for the Altiplano. For more examples of the horizontal synthetic test see the Appendix A.4.

3.3.1.2. Vertical tests

Here we present the results for two tests that are based on real anomalies expected in the area of the Puna profile for P- wave velocity anomalies. The initial anomalies shown in Figure 3.11 include three crustal anomalies that should represent a low-velocity block (-6%) in the volcanic arc, a high-velocity block of the Puna in the centre (+8%), and a low-velocity block in the East which models the presence of some back-arc volcanoes and the eastern border from the plateau (-6%). An additional low-velocity block (-3%) has been included below the crust between 80 km and 150 km depth. The results show that the shapes of the crustal anomalies are well reconstructed and that the smearing is only seen vertically.

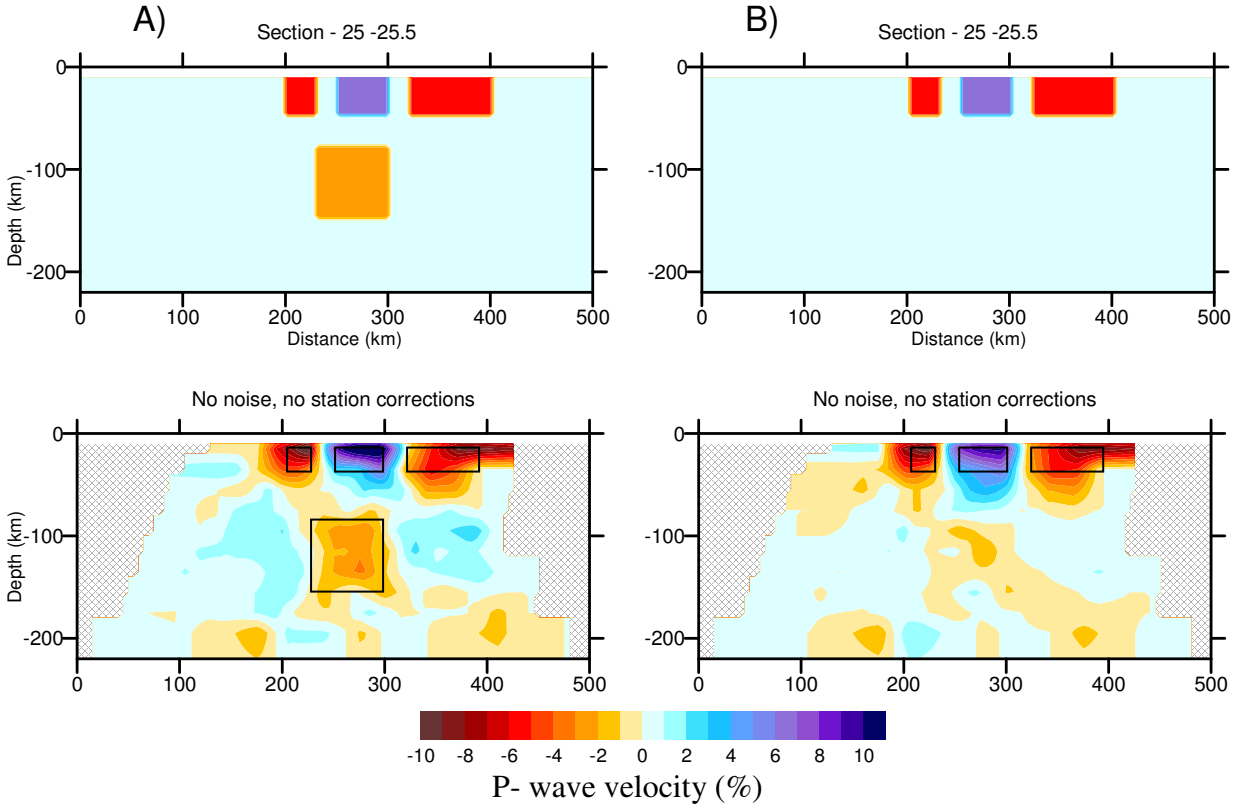

Figure 3.11: Synthetic test for the Puna profile showing the results of the reconstruction of synthetic anomalies with the rays corresponding to the real data set. A): Shape of the initial anomalies, 4 in this case, simulating upper crustal anomalies and an internal anomaly represented as a block between 80 and 150 km. (B): The block anomaly is subtracted from the simulation and reconstruction is made using data without noise and stations corrections. The west-east profile between 70°W (0km) and 64°W (500km) shows the distribution of anomalies at deeper levels according to the ray coverage.

After the first approach shown in Figure 3.11, some changes were introduced to include a slab-shaped anomaly with an amplitude of 4% and just two bigger anomalies instead of the previous three or four anomalies (Figure 3.11). In this case, we have one anomaly in the east, representing the low-velocity CVZ or Western Cordillera where the arc volcanoes are located with an amplitude of -7% and a low-velocity block on the eastern border of the Puna plateau (-5%). This was done to test the proposal that back-arc magmatic activity is related to delamination processes (e.g. Kay et al., 1993 and 1997; Schurr, 2000). Vertical smearing is again present but the horizontal position of the anomalies is well reconstructed (Figure 3.12). For more examples of the vertical synthetic tests see the Appendix A.4.

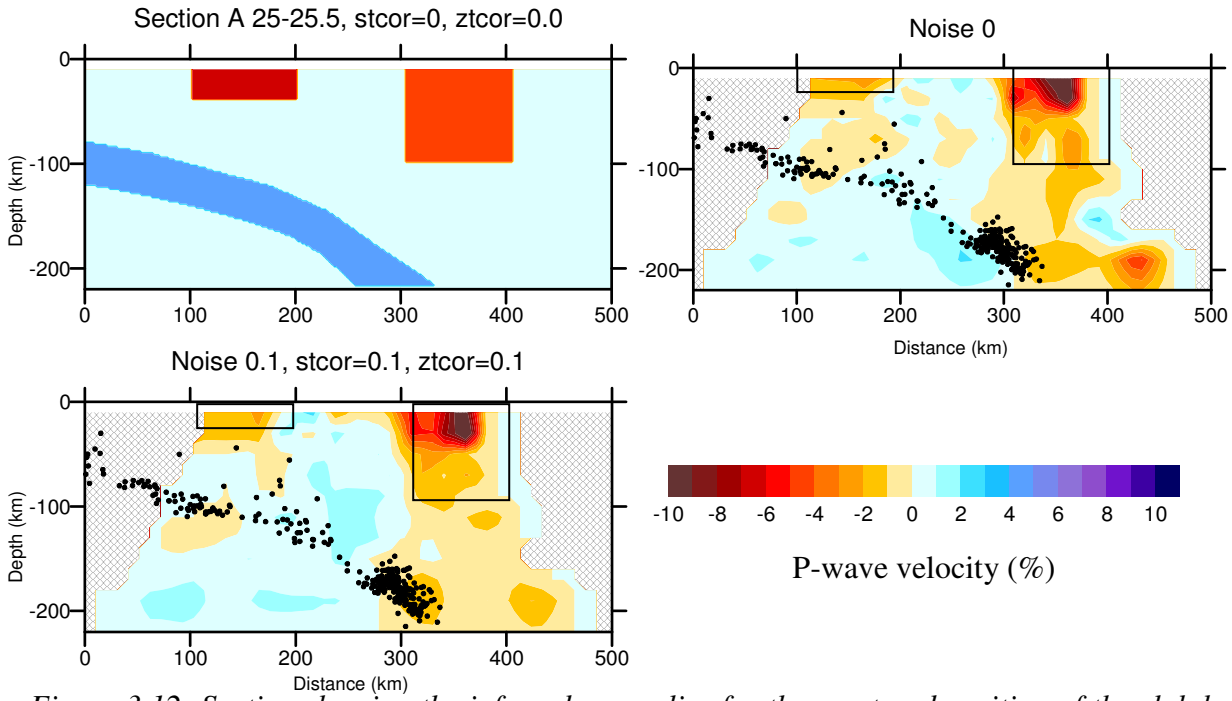

Figure 3.12: Section showing the inferred anomalies for the crust and position of the slab based on seismicity from Engdahl et al. (1998). Note that the smearing arising from using data without noise is strong in the vertical resolution of the eastern block. When applying small amounts of noise, station (stcor) and source (ztcor) corrections, the smearing is reduced but the anomalies remain in their proper positions. The slab anomaly can not be reconstructed, even when no noise is applied to the model. Colour scale represents relative velocity in %.

3.3.1.3. The slab beneath Puna

The image with the position of the slab in Figure 3.12 shows results that this feature is not resolved while the upper-crust anomalies are well reconstructed. The slab's identification needs to be improved and this is done in the following step. As explained in section 3.2.1 (Figure 3.5),

we do not have a good resolution of the slab. At this latitude, the presence and position of the slab has always been a subject of controversy since this is a zone of transition between normal subduction to the north (~30° is the dipping angle of the slab) and flat subduction (~10-15°) to the south of our study area (Wigger et al., 1991; Cahill and Isacks, 1992; Withman et al., 1996; Allmendinger et al., 1997; Kay and Kay, 1993 and 1994; Kay et al., 1999). Remember that sub-horizontal structures cannot be reliably recovered (Evans and Achauer, 1993). The approach used to image the slab is similar to that introduced in section 3.2.

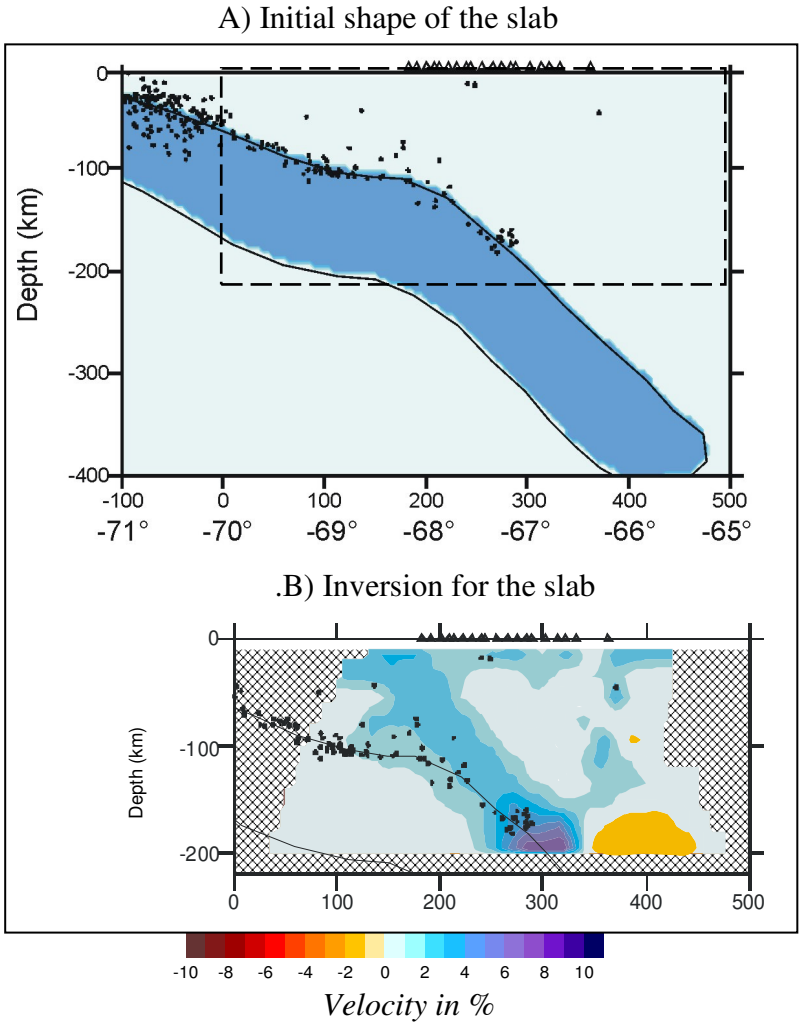

Figure 3.13: A) Initial shape of the slab. Note that this is carried out for a slab down to 400 km depth while the inversion of the data is performed to 200 km depth. The anomaly of the slab is + 6%. Triangles represent the stations along the Puna profile. B) Inversion showing results after correcting for the slab.

As shown in Figure 3.13, the inversion after corrections for the slab is performed for a velocity contrast of 6% for the slab anomaly. The initial model and position of the slab is shown in the way that dt^{slab} are computed along the ray paths down to the depth of 400 km while the inversion is performed for the depth interval 0-200 km. This fact enables the plotting of the slab so that the

upwards shift is not too strong in our study area. It must be observed that this produces an undesired effect that can be seen in the concentration of rays at the bottom of the slab (where it becomes nearly vertical). This effect is usually represented by the development of low-velocity anomalies near the high-velocity end of the slab, as seen in figure 3.13 B at a depth of ~200 km.

3.3.2. Real data inversion: Puna

The inversion results for the initially observed residuals are performed along the profile at 25.5°S. The Argentine Puna profile is relatively short (~200 km), with the depth of investigation, according to the incident rays tracing, reaching 200 km. Below this depth we lack the necessary resolution with smearing tending to be larger (Figure 3.14). We have also the chance to compare our results with those from other seismological projects such as PUNA 97 (Schurr et al., 1999 and Schurr, 2000) in the north of our study area.

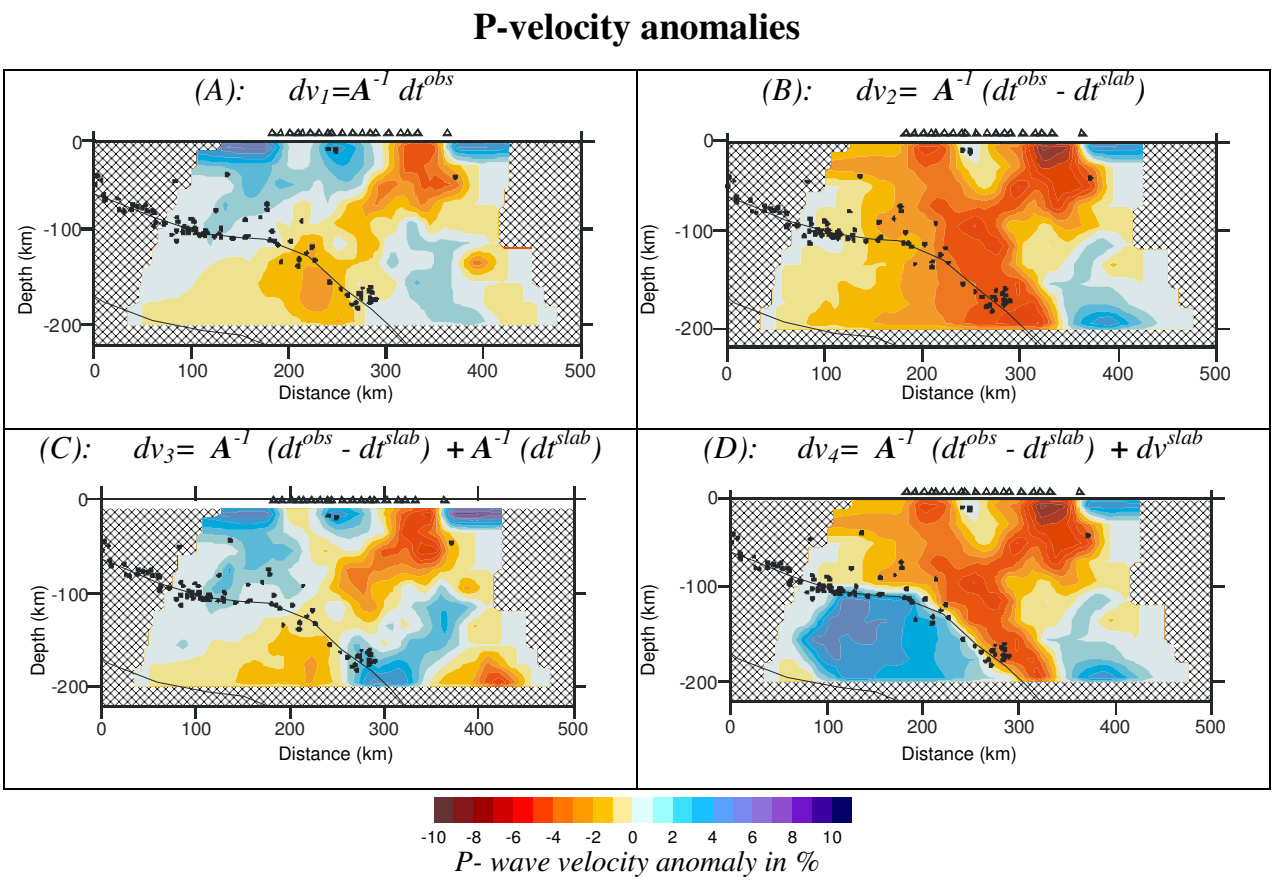

Figure 3.14: Results of the inversion for P- wave residuals with and without information about the slab in three vertical sections. (A): 1-D model inversion without the slab, (B): Inversion for data after the subtraction of the slab, (C): Superposition of the inversion results for "no-slab" residuals with the addition of slab residuals. The models A and C are equivalent when explaining the observed residuals, but C contains a-priori information about the slab. (D): Final section showing the combination of inversion results for "no-slab" residuals with the model of the slab.

The real data inversion results for the Puna profile are shown in Figure 3.14. The model presented in Figure 3.14D: $dv_4 = \mathbf{A}^{-1} (dt^{obs} - dt^{slab}) + dv^{slab}$ is preferred for our interpretation as the image resolves the position of the slab.

The same strategy as discussed in section 3.2. was applied for the inversion of the S-wave data. The total number of S- wave residuals was about 300, compared to the P- wave data set of 1100 rays. The results are shown in Figure 3.15A, 3.15B and 3.15C. Results for inversion with and without subtraction of the slab are presented. One image is not being displayed (case presented in Figure 3.14C for P- waves). In the initial model, a slab with the velocity contrast of 4% is used. The inversion results for the Puna are presented as horizontal sections in the Appendix A.5.

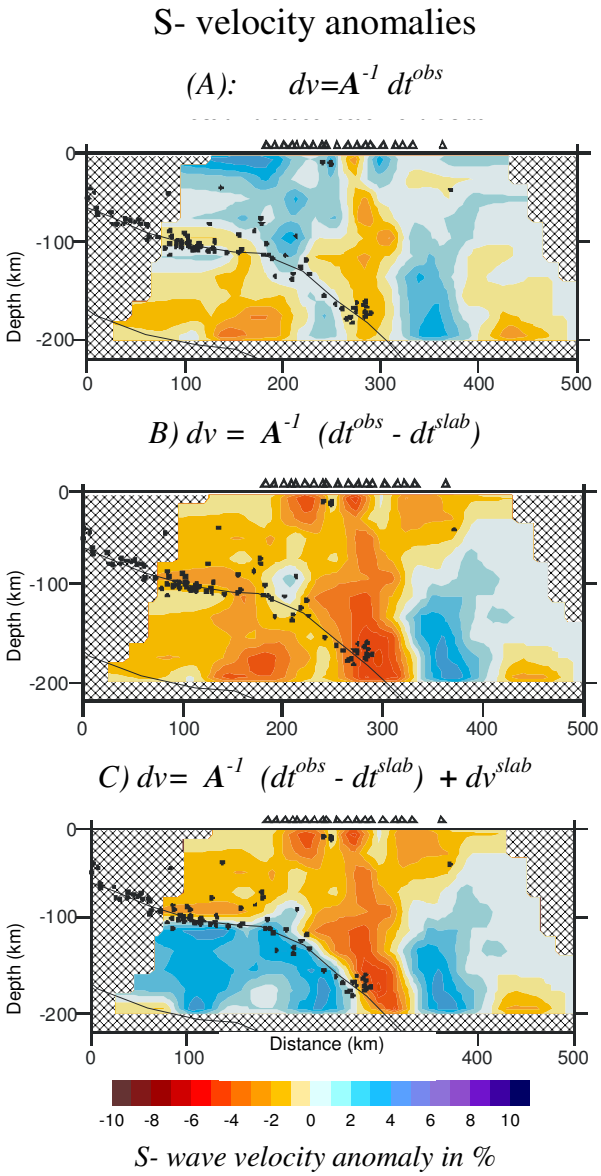

Figure 3.15: Results showing the inversion for S-residuals, with and without the slab on vertical sections using the same strategy as in Figure 3.14. Triangles represent the stations.

Chapter 4

The Altiplano Plateau

4.1. The Central Andes at 21°S and the Altiplano plateau

4.1.1. Geotectonic setting of the Altiplano

As mentioned in the Introduction, the Andes mountain belt represent an area that has been formed as a result of convergence and subduction of an oceanic plate (Nazca Plate) under a continental plate (South American Plate). The Central Andes (between ~14°S and ~24°S) are located where the subduction of the Nazca Plate occurs at angles near 20-30°, at a rate of 65mm/yr (e.g. Cahill and Isacks, 1992, Angermann et al., 1999) and are the widest segment of the mountain range (Figure 1.1).

The variable thickness of the crust and the different dipping angles of the subducting plate along strike have created an elevated plateau in the central segment of the Andean orogeny with geological, morphological and magmatic characteristics that enable a differentiation of the plateau between the Altiplano in the north (Bolivia and Peru) and the Puna in the south (north-western Argentina) (e.g. Allmendinger et al., 1997).

With an average elevation of ~4 km and a width of ~400 km, the Andean plateau is limited to the west by an active volcanic arc (Western Cordillera) and to the east by an active westward verging thin-skinned foreland thrust belt (Eastern Cordillera) (e.g. Whitman et al, 1996). To the east, the topography descends by steps at the Interandean Zone, the currently active Subandean fold-thrust Belt and the Chaco Plain that progressively overlaps with the Precambrian Brazilian shield (also called Guaporé Shield) (Figure 3.1B).

4.1.2. Geophysical investigations in the Central Andes

A series of projects have integrated geophysical methods and geological observations to investigate subduction related features. Steep-angle and wide-angle reflection surveys (Wigger et al., 1994; Ancorp Working Group, 1999 and 2003; Haberland and Rietbrock, 2001; Lueth, 2000) and PISCO 94 (Schmitz et al., 1999; Graeber and Asch, 1999), CINCA 95 (Husen et al., 1999; Patzig, 2000), ANCORP 96 (Haberland and Rietbrock, 2001; Ancorp Working Group, 2003), PUNA97 (Schurr et al., 1999 and 2003; Schurr, 2000; Schurr and Rietbrock, 2004) passive seismological networks were operated to obtain receiver function and local tomography images.

The ANCORP project integrated steep angle reflection and refraction at 21°S with a network of passive seismic stations to image the subduction zone and related volcanism, crustal thickness and other subduction related structures. The first results presented by the Ancorp Working Group (1999) imaged the subduction and extension of the Benioff zone (Nazca reflector down to 100 km depth) and detected the presence of another reflector at a depth of 20 to 30 km (~68.5°W) that was given the name of Quebrada Blanca Bright Spot reflector anomaly (QBBS, also in Ancorp Working Group, 2003). The origin and composition of the QBBS in not clear but it has been suggested to be caused by the presence of fluids (results of ANCORP are summarized in Figure 4.1). Although magneto-telluric soundings have not detected the QBBS anomaly, an important conductivity anomaly (Altiplano Conductivity Anomaly) below the Altiplano has been

detected while the presence of free fluids is proposed due to high electrical conductivity values (up to 1 S/m) (Brasse et al., 2002; Haberland et al., 2003). At the same time this high reflective anomaly (QBBS) has not been observed in gravity data (Götze and Kirchner, 1997). To the east, a reflector was also detected coinciding with the approximately position of the Altiplano Low-Velocity Zone (e.g. Wigger et al 1994; Yuan et al., 2000).

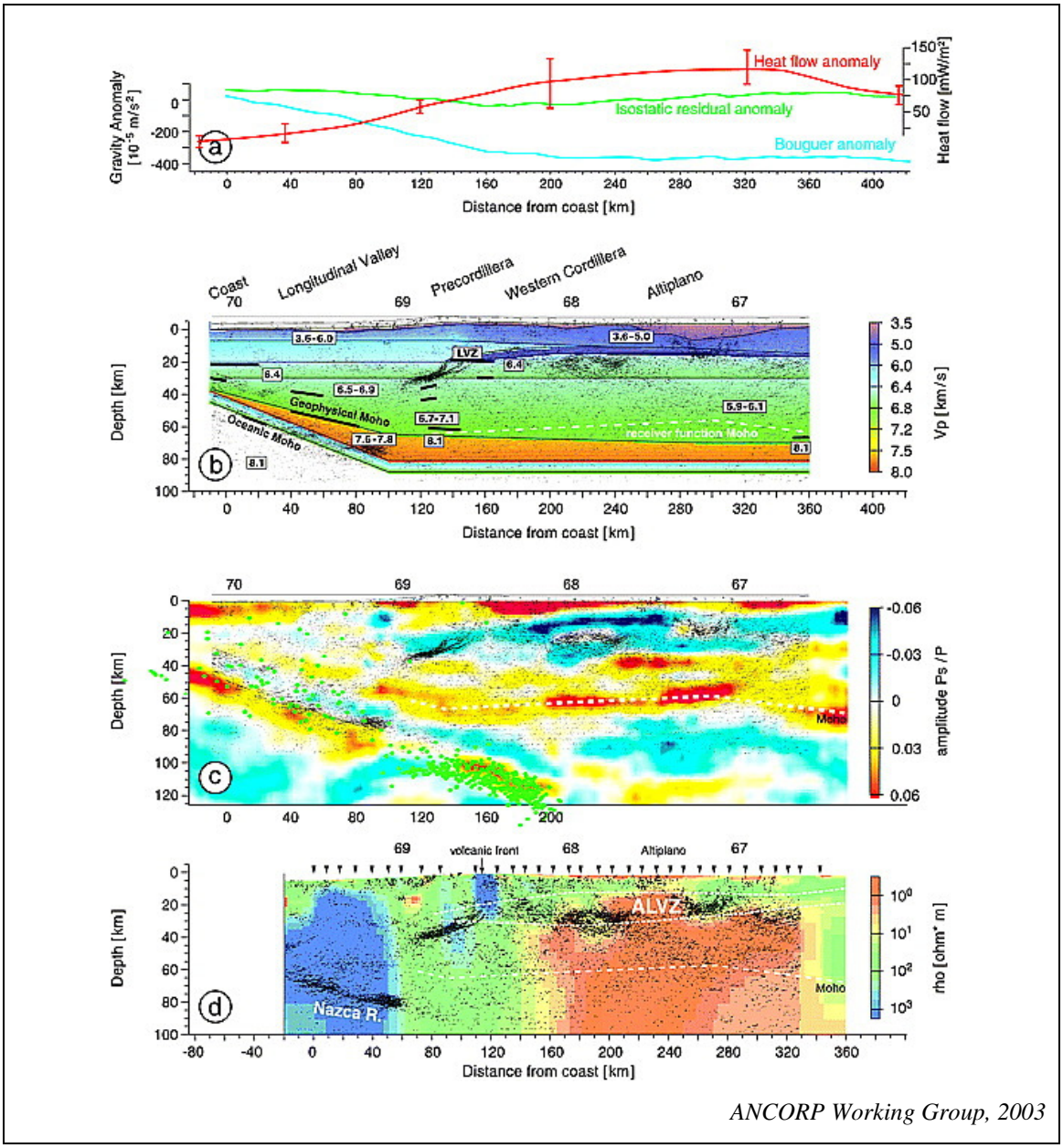

Figure 4.1: The main results for the central Andes transect at 21° S as presented by the ANCORP Working Group (2003) a): gravity data - Bouguer anomaly ~ -400 mGal. and heat flow data (from Goetze and Kirchner, 1997 and others); b): wide angle results from ANCORP data; c): receiver function results from Yuan et al., 2000; d) electrical resistivity model (Brasse et al., 2002). Note the position of the ALVZ in figures c) and d). The ANCORP line extended from the coast in Chile at ~70.3°W to 66.5°W in Bolivia. Our Refuca profile extended the ANCORP line ~200 km to the east.

At a depth of 80 km, a reflector above the oceanic slab has been interpreted as the serpentinization front that delivers rising fluids (Ancorp Working Group, 1999; Schilling et al., 1997 and 2000). Beneath the Altiplano-Puna region, a crustal low-velocity layer has been detected by receiver functions and magneto-telluric studies and is explained as being related to the presence of partially melted material (Wigger et al., 1994; Yuan et al., 2000; Brasse et al., 2002; Chmielowski et al., 1999; Zandt et al., 2003).

Related to the subduction zone, teleseismic receiver function analysis imaged the oceanic Moho down to a depth of 120 km (Yuan et al., 2000) which coincides with a reduction in seismicity in the slab. Short-period conversions from local earthquakes extend these observations to depths of 160 km (Bock et al., 2000). Guided wave studies (Martin et al., 2003) trace a thin wave guide channel above the subducted slab down to a depth of at least 160 km.

Other projects carried out in the region provided important results about the lithospheric structure and crustal-thickness variations. The Broadband Andean Joint (BANJO) and Seismic Exploration of the Deep Andes (SEDA) experiments operated broadband seismometers to record local and teleseismic earthquakes. BANJO was a west-east oriented array of 16 stations from Chile to Bolivia between 19° and 20°S. The SEDA array was oriented mainly north-south through the transition region between Altiplano and the Eastern Cordillera from 17° to 20°S. The results obtained provided information about travel-times and attenuation of P- and S- waves for regional mantle earthquakes and greatly improved the knowledge of the Central Andean crust and mantle lithosphere (Beck et al., 1996; Myers et al., 1998; Dorbath and Mason, 2000; Beck and Zandt, 2002).

A map of the Altiplano lithosphere obtained from attenuation tomography inferred from regional mantle earthquakes shows variations in the thickness of mantle lithosphere interpreted as a reaction to lithospheric thinning and shortening (Figure 4.2), (Myers et al., 1998).

Other authors (e.g. Beck and Zandt 2002) combined teleseismic and deep regional events for receiver function analysis and suggested that the thick crust supporting the high elevations should be of felsic to intermediate composition. They support the results of Wigger et al. (1994) and also suggest that the Brazilian lithosphere is underthrusting part of the western side of the

Eastern Cordillera. According to their results, basal parts of the lithosphere could be delaminating at the Altiplano-Eastern Cordillera boundary area.

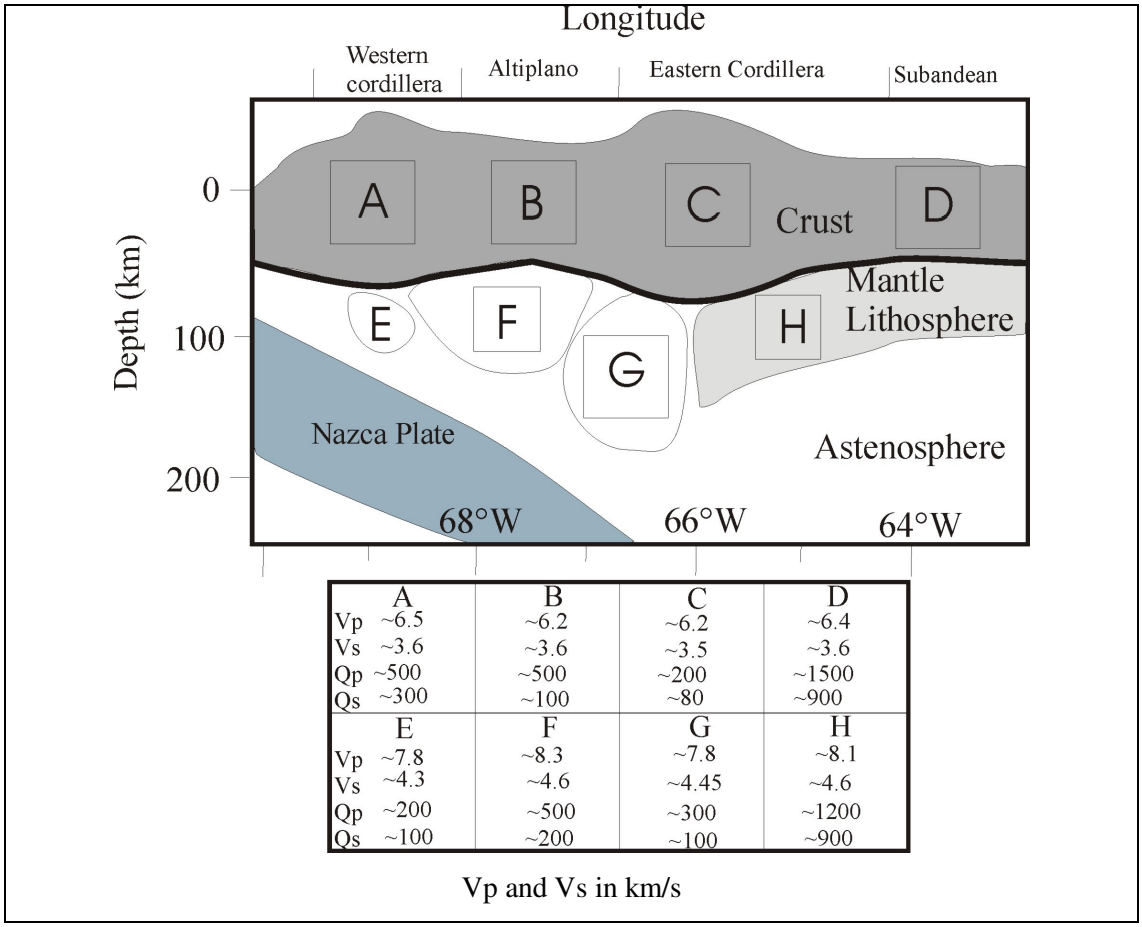

Figure 4.2: A map of the Altiplano lithosphere inferred from a tomographic inversion and evaluated seismic attenuation based on data recorded by the BANJO and SEDA arrays. Note the low Vp and Vs and low Qp-Qs for G at 100 km depth (Modified from Myers et al., 1998).

Data integrating some of the before mentioned temporary broadband networks (BANJO, SEDA, PISCO) recorded teleseismic and local waves, providing information from above and below the subducted slab. Shear wave splitting analysis shows fast polarization velocities from north to south (trench parallel). A change of anisotropy to fast velocities from west to east at ~65°W (Polet, 2000) has been related to the old and cold Brazilian lithosphere.

Results from global teleseismic inversions have provided a clear image of the subduction zone for the Altiplano plateau area along ~21°S (Figure 4.3) and show low-velocities in the area of the continental crust and relatively high velocities for the subducted slab (Bijwaard et al., 1998). However, global tomographic images lack the resolution necessary to investigate the upper portions of the asthenosphere-lithosphere region.

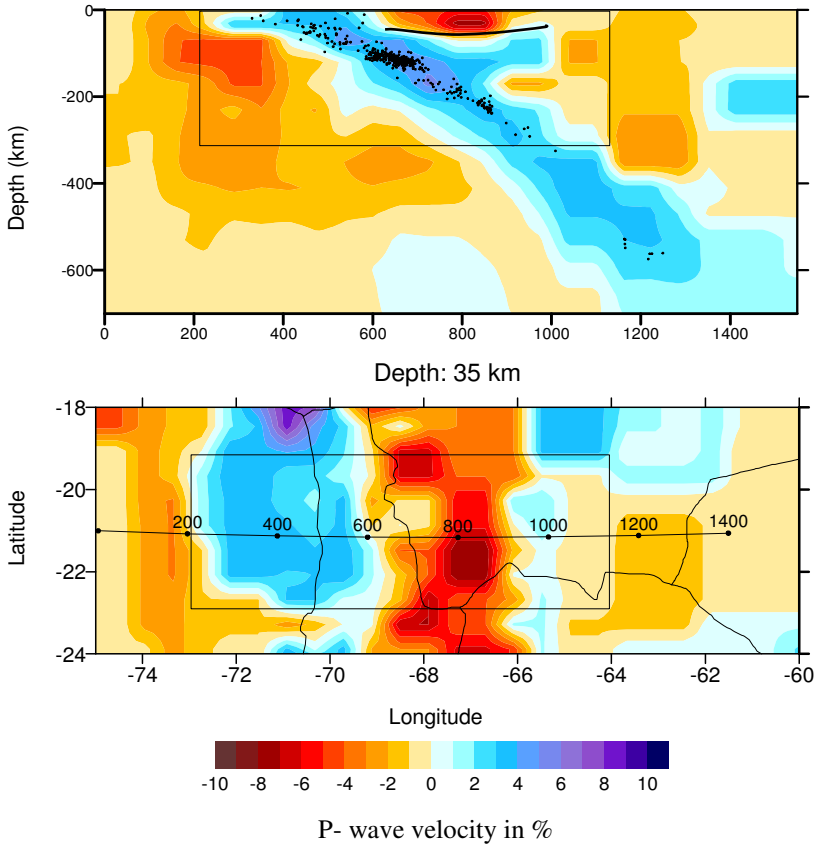

Figure 4.3: Results of the global tomography inversion after Bijwaard et al. (1998) for a vertical (top) and horizontal section (bottom). Positions of our vertical and horizontal sections shown in figures 2.1 and 3.1 are highlighted by rectangles and the line in the vertical section is the Moho topography. Colour scale is the same as in previous figures (see also Fig. 3.3 to 3.6).

4.1.3. Crustal thickness beneath Altiplano

The crustal structure of the Central Andes has usually been presented as one of the main aspects to consider when attempting to understand the evolution of the plateau. Hence, the crustal thickness has become a major subject of discussion over the last few decades (e.g. Isacks, 1988; Jordan et al, 1983; Allmendinger et al., 1997).

Among the first studies that estimated the crustal thickness of the Western Cordillera were those using surface waves (e.g. James, 1971). Later, wide angle active experiments provided results for the entire continental crust from the Pacific coast to the Chaco plain (e.g. Wigger et al., 1994; Schmitz et al., 1999).

Making use of regional gravity studies, Goetze et al. (1994) estimated the crustal depth for the entire plateau between 20°S and 26°S to be less than 70 km, while other authors obtained crustal thicknesses of ~70-75 km under the Altiplano (Wigger et al., 1994; Zandt et al., 1996; Beck et al., 1996; Scheuber and Giese, 1999; Schmitz et al., 1999; Yuan et al., 2000).

Yuan et al. (2002) produced a detailed map of the crustal thickness of the Central Andes based on receiver function analysis and showed that the depth to the Moho varies from 25-30 km at the coast, to 70-75 km beneath the volcanic arc and the Altiplano, while thining to about 30 km beneath the Subandean and Chaco plain. In comparison, the southern part of the Puna plateau has a Moho that is, on average, 10-15 km shallower and has a topographic elevation at least 500 m higher than the Altiplano. Other processes such as magmatic addition, tectonic underplating or upper mantle hydration may contribute to the thickening of the crust (Allmendinger et al., 1997).

4.1.4. Crustal shortening

Crustal shortening has been usually proposed to explain much of the thickness of the continental crust in the Central Andes (Zandt et al, 1994; Beck et al., 1996). About 250 km of crustal shortening which occurred mainly in the Eastern Cordillera (EC) and Subandean region is likely to be responsible for the thickened crust beneath the Altiplano (Baby et al., 1992; Schmitz, 1994; Allmendinger et al., 1997; Kley and Monaldi, 1998).

Watts et al. (1995) analyzed the elastic thickness of the lithosphere in the Central Andes and proposed a model for explaining the large amount of shortening in the bend region at ~20°S. They suggest that where the lithosphere is flexurally strong (i.e. with a large elastic thickness) foreland deformation is concentrated on the Subandean thin skinned and fold and thrust belt that has absorbed more than 100 km of shortening. North and south of this "symmetry axis" (bend region) the flexurally weaker lithosphere has a more complex deformation that involves the basement and hence, has absorbed less shortening.

On the eastern border of the Altiplano, Wigger et al. (1994) identified west-dipping structures in the crust, also confirmed by other workers (Allmendinger et al., 1997; Watts et al., 1995; Lamb

et al., 1997; Yuan et al., 2000) that are possibly related to the underthrusting of the Brazilian shield beneath the Subandean and Eastern Cordillera provinces (Figure 4.4).

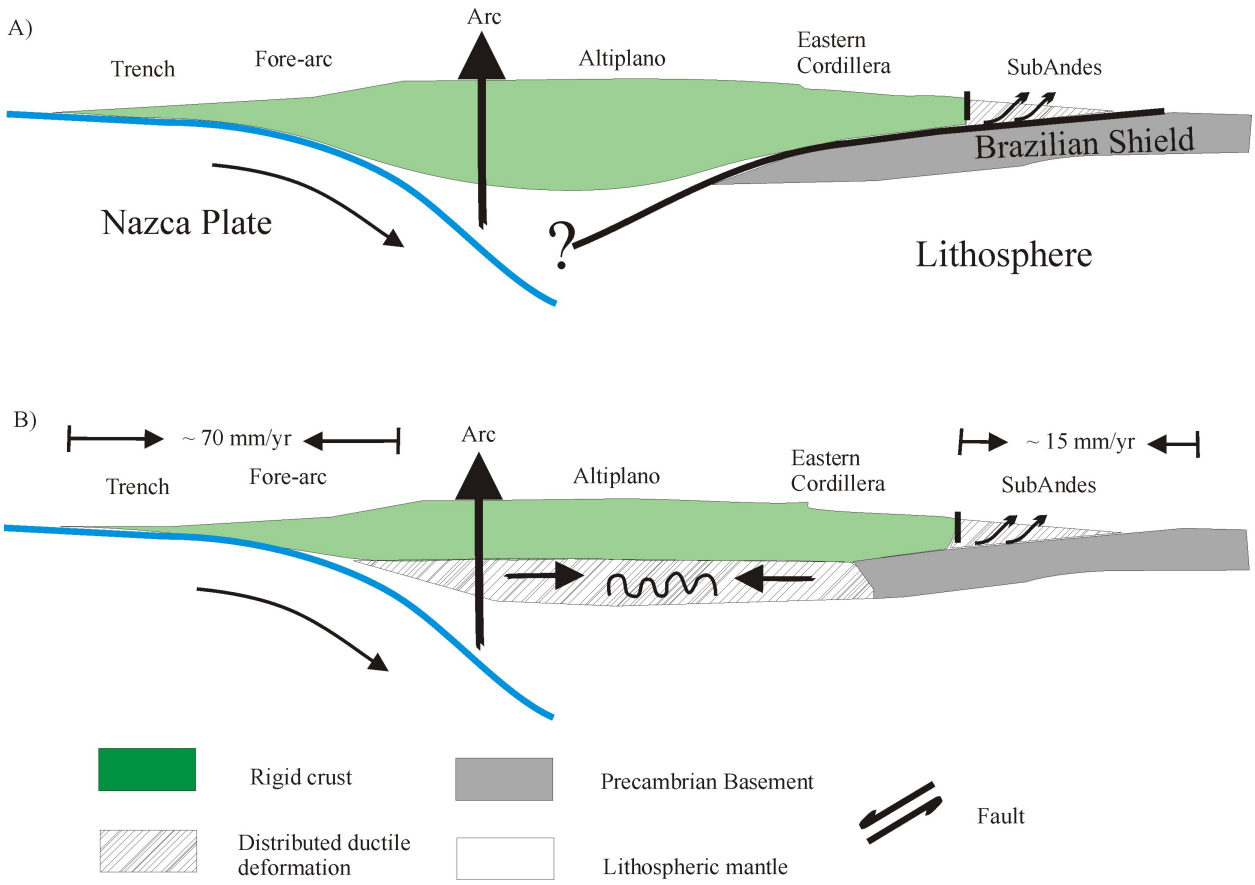

Figure 4.4: Two models for deformation at the border of Altiplano and Eastern Cordillera. The first model (top) suggests that thin-skinned deformation in the Subandean is responsible for a detachment zone that affects the entire upper crust. The second model (bottom) shows that the thermally affected lower crust is responsible for a ductile zone of deformation; in this case the Altiplano behaves like a rigid lid (after Lamb and Hoke 1997).

Identification of the fault systems or thrusts that penetrate the entire crust is still needed to image the distribution of crustal shortening along the eastern part of the Andes. Until now, there were no geophysical data available that could help us image this area over crustal scales. Geological and structural models based on kinematic studies suggest that the main thrusts could penetrate as far as the western part of the Eastern Cordillera (Kley and Monaldi, 2002).

4.1.5. Fluids and thermal structure of the plateau.

The presence of fluids and melts is assumed beneath the active volcanic front and the Altiplano-Puna plateau. Their possible pathways in the lithosphere have been traced by different authors (e.g. Ancorp Working Group, 1999; Schurr et al., 2003). Model calculations based on heat-flow density are the only type of investigation that can provide a realistic image of the Central Andes thermal state. Some authors have presented models based on surface heat-flow density data at lithospheric scales that show little thermal variation along strike and larger variations across the orogen. Local heat sources in the volcanic arc and the background heat-flow effect of the subduction process are both explained by the presence of asthenospheric mantle at shallow depths. These temperature variations would be responsible for geophysical anomalies beneath the volcanoes (local magma chambers - on a local scale) and beneath the Altiplano region on a large scale (Springer and Förster, 1998; Springer, 1999).

4.2. Results and Observations

Tomographic images for both P- and S- waves are shown in vertical and horizontal sections in the Appendix at the end of this work. The morphological units and their geodynamic relevant locations are displayed on a schematic cartoon along with the interpreted anomalies at depth, where the present results are discussed (Figure 6.1, chapter 6). As explained in chapter 3, the limitations imposed by the resolution of horizontal structures along a profile of stations do not provide adequate constraints to determine the extension of the anomalies on plan view. We will concentrate therefore mainly on the following vertical anomalies due to their position and importance (Figure. 4.5). They are described from west to east as follows.

1- The region west of the Precordillera is characterized by the presence of a pronounced high velocity anomaly seen by both P- and S- waves, to a depth of 60 km, representing the Chilean Coastal Cordillera and is part of the Longitudinal Valley. This anomaly could be related to the presence of the Jurassic arc which developed on Precambrian-Paleozoic crust (Troeng et al., 1994; Lamb and Hoke, 1997).

2- The limit between high-velocity anomalies to the west and low-velocities towards the east, at approximately 69°W, corresponds with the location of the West Fissure (WF) on the surface, representing the western limit of the Precordillera. The change in relative velocities west and east of the West Fissure indicates variations in the composition and state of the rocks along this fault. To the east of the West Fissure the presence of an anomalous reflective body has been described at a depth of 15 and 25 km and interpreted as the Quebrada Blanca Bright Spot (e.g. QBBS in Ancorp Working Group, 1999). We also interpret the position of this low-velocity anomaly as the QBBS at approximately ~68°W probably indicating the presence of fluids or magmatic bodies related to the volcanic front (Central Volcanic Zone, CVZ). Underneath the receiver function Moho (Yuan et al., 2000) we detected what we interpret to be magmatic additions at the base of the continental crust. These additions should play, in combination with other geological and geotectonic processes, an important role in crustal growth. Although the Moho topography supports this idea, it has long been estimated that magmatic addition from arc production represents ~1 % of the crustal thickness (Trumbull, pers. comm.)

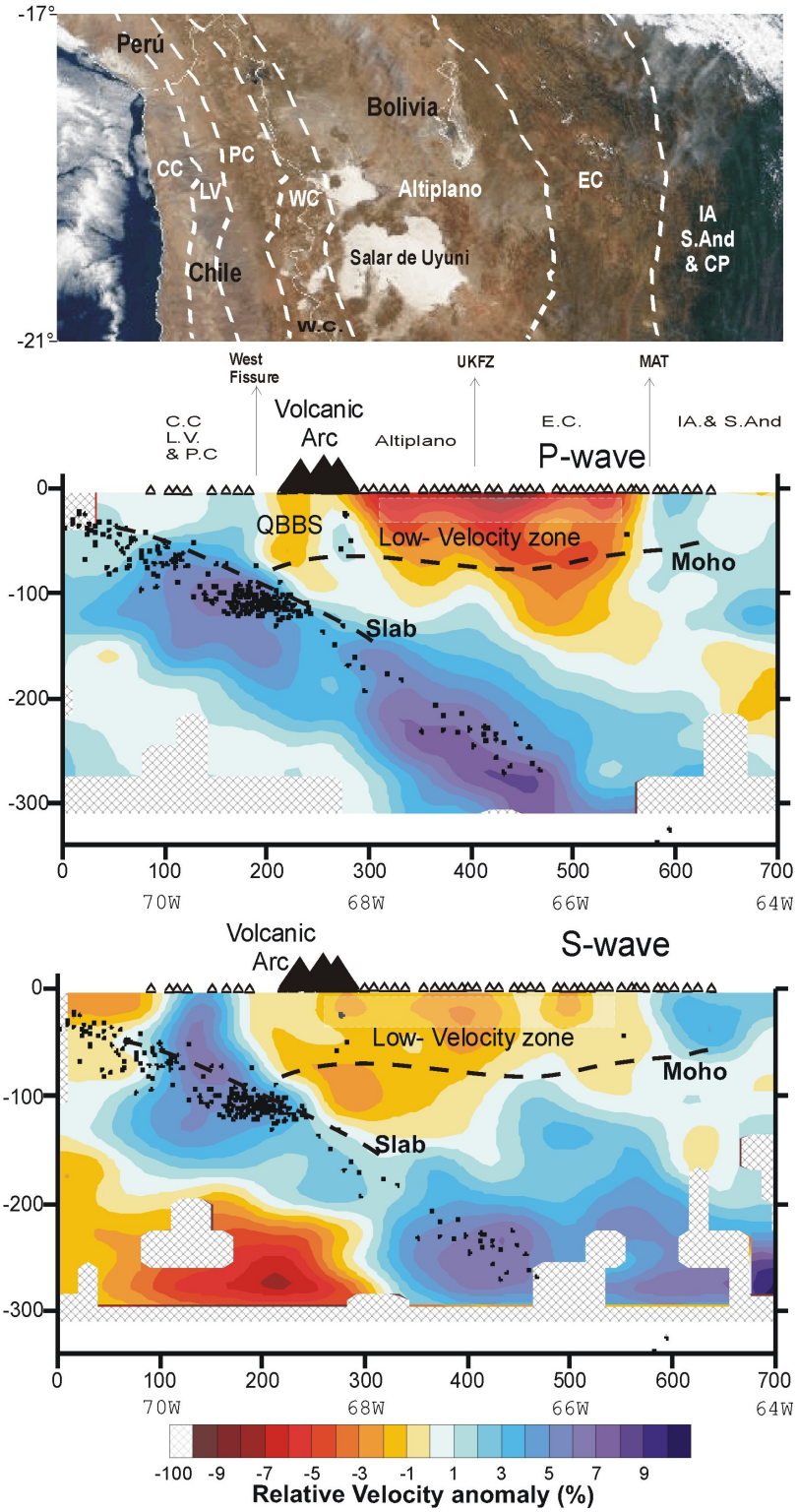

Figure 4.5: (Top) Satellite image showing morphological units along 21°S, C.C.: Coastal Cordillera; L.V.: Longitudinal Valley; PC: Precordillera; WC: Western Cordillera; EC: Eastern Cordillera; IA: Interandean; SAnd: Subandean; CP: Chaco Plain. Centre and bottom: P- and S-wave results; receiver function Moho (present data, see chapter 6); QBBS: Quebrada Blanca Bright Spot; UKFZ: Uyuni-Kenayani Fault Zone; MAT: Main Andean Trust. Low Velocity Zone is the same ALVZ Altiplano Low Velocity Zone mentioned before.

3- The Altiplano plateau is characterized by a prominent low-velocity anomaly in the east, for both P- and S-waves. The shape and position of the Altiplano anomaly seems to be strongly controlled by the presence of the Uyuni-Kenayani Fault Zone (UKFZ) at ~67°W. The presence of a low-velocity layer or Altiplano Low-Velocity Zone (ALVZ) has already been described under the Altiplano and adjacent areas (Wigger et al., 1994; Yuan et al., 2000) and is also present in our data, having a west-east extent from ~67.5°W to ~65°W. It has been generally accepted that the ALVZ represents a partially molten zone. The extension and presence of this layer of probably partially melted material may be explained in accordance with geological observations such as the Main Andean Thrust (MAT) also called Interandean Thrust (e.g. Mertmann et al., 2001; Scheuber et al., submitted). The MAT is a prominent detachment zone located at the border between EC and the Inter- Subandean units (e.g. Allmendinger et al., 1997) that could be affecting the entire portion of the upper crust (Figure 4.6). It should also be considered that such a response from the crust could be related to, at least, two possible situations:

a) Strong upper crust, strong lower crust, weak upper mantle: the first two are deformed together while the upper mantle acts as an accompanying unit where deformation is hardly recognized.

b) Strong upper crust, weak lower crust, strong upper mantle: the lower crust is deformed together with the upper crust while the upper mantle does not react and remains stable and undeformed.

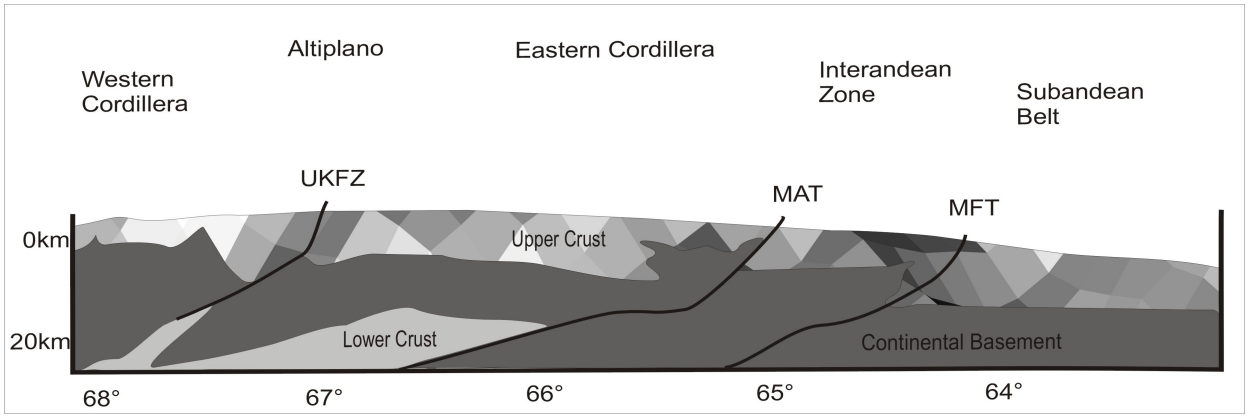

Figure 4.6: Structural cross section along 21°S. The presence of the MAT (Main Andean Trust) along the section at 21°S, affects the entire structure of the upper crust and reaches portions of the lower crust where we detect the low-velocity anomalies at the border between Altiplano and the Eastern Cordillera. Simplified after Mertmann et al.,(2001) and Scheuber et al. (Submitted).

The detachments described in this study have been clearly imaged by seismic refraction (Wigger et al., 1994) and could be responsible for zones where changes in lithostatic pressure, material state of the rocks and temperature variations affect the configuration of melts and fluids that move along these structures in the interior of the crust.

4- The Eastern Cordillera presents what we interpret as an extension of the low-velocity zone towards the east of the Altiplano (Yuan et al., 2000; Brasse at al., 2002; Haberland, et al., 2003). The anomaly is located between ~66.5°W and ~65.5°W.

At ~66°W we detect on S- wave tomographic image (see Fig. 4.5), an influx-like structure with high velocities underlain by a high-velocity body between 100 and 150 km depth that is proposed to be part of the old cold lithosphere (Lithospheric Block? in chapter 6-Figure 6.1) that might have separated from the base of the crust.

5- East of the Eastern Cordillera and the position of the Main Andean Thrust (MAT), we detect the presence of a strong, high-velocity anomaly in both P- and S-wave analyses, that we interpret as the Brazilian shield - also called the Guaporé shield covered by Neogene sediments filling the basins from the Interandean, Subandean and Chaco Plain provinces. We assume that the presence of the Brazilian shield (BS), as a cold and old unit underlying the before mentioned sediments, is responsible for the observed anomaly. Unfortunately, the resolution of the upper and deeper parts of the anomaly is not sufficient to determine if there is some type of deformation structure present. Therefore, underthrusting of the Brazilian lithosphere can not be recognized in the tomographic results. The limit between the Brazilian shield with high velocities and the Eastern Cordillera with low velocities appears to indicate that shortening occurred mainly in this region. A flexurally strong lithosphere, as suggested by Watts et al. (1995), should play a key role in the configuration of the BS anomaly and explain foreland deformation in the thin-skinned fold-and-thrust belt. The Interandean, the Subandean and Chaco morphological units could therefore be situated above a series of detachments where great amounts of shortening has taken place.

Chapter 5

The Puna Plateau

5.1. The Central Andes at 25.5°S and the Puna Plateau

5.1.1. Puna and Altiplano plateaus

As already discussed in chapter 4, the Altiplano and Puna high plateaus in the central segment of the Andean orogen represent local variations in the geological history of uplift, amount of shortening, magmatism with related volcanism and changes in topography (e.g. Reutter et al., 1988; Allmendinger et al., 1997). These changes in characteristics enable a differentiation between Altiplano and Puna and can be recognized approximately north and south of the parallel 22°S, near the Bolivian-Argentine border, coinciding with the trend of an impressive fault system (Lipez lineament NW-SE – Figure 5.1).

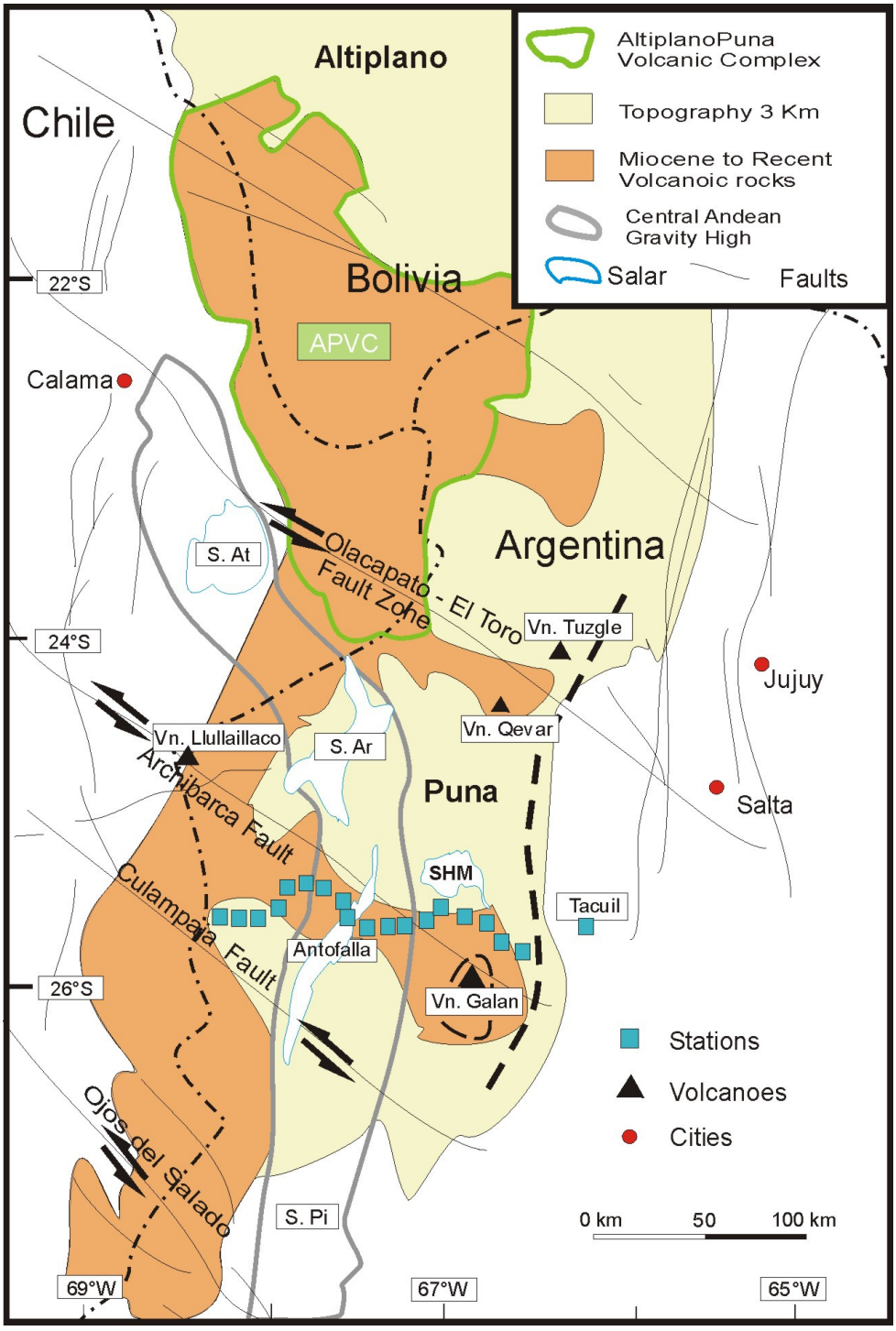

Figure 5.1: Map showing the principal lineaments of the Puna (Lipez, Olacapato-Toro, Archibarca, Culampaja and Ojos del Salado). The position of our profile in the southern end of the Puna at ~25.5°S is also plotted (blue squares). Green area: (APVC) Altiplano-Puna Volcanic Complex from deSilva (1989); S. At: Salar de Atacama, S.Ar: Salar de Arizaro, SHM: Salar del Hombre Muerto, S. Pi: Salar de Pipanaco. Gray line: encloses the region of the Central Andean Gravity High (Goetze and Krause, 2002). Black dashed line represents the eastern border of the Puna plateau where an apparent change in the temperature of the rocks in the crust is detected (Ocloyic fold and thrust belt?). (Modified after Riller et al., 2001)

The presence of the Altiplano-Puna-Volcanic-Complex (APVC by de Silva, 1989) between both parts of the plateau at the triple junction between Argentina, Bolivia and Chile has been suggested to be responsible for late Miocene to Recent ignimbrite deposits (Figure 5.1.). The APVC overlies a large part of the ALVZ which is suggested to behave as a migmatite zone in the middle-upper part of the crust (Trumbull, pers. com.). Below the APVC, the presence of a very low-velocity layer at depths between 10 and 30 km has been interpreted as a sill-like magma body named the Altiplano-Puna Magma Body (APMB) (Chmielowski et al., 1999; Zandt et al., 2003) Along the APVC area, a transition based on the chemistry of Tertiary rocks, topography and structural changes north and south of 22°S that differentiates Altiplano and Puna has also been proposed by many authors (e.g. Allmendinger et al., 1983 and 1997; Allmendinger and Gubbles, 1994; Coira et al., 1993; Whitman et al., 1996) (Figure 5.1).

The volcanic arc has been migrating to the east since the Jurassic to its actual position at the CVZ. The magmatism changes form andesitic to dacitic with some expressions of shoshonitic and basaltic rocks in the southern end of the Puna. Large volumes of silicic ignimbrites are associated with the terminal volcanic activities represented by collapse of calderas (e.g. La Pacana in Chile, Cerro Galan and Cerro Blanco in Argentina).

In general, the plateau is limited to the west by an active volcanic arc consisting of Tertiary volcanic rocks (Western Cordillera, WC or Central Volcanic Zone, CVZ) and to the east by an active westward verging thin-skinned foreland thrust belt (deformed Paleozoic rocks of the Eastern Cordillera).

By comparing the elevations of the entire plateau from 20°S to 26°S it is also possible to detect some differences. The Puna plateau in Argentina, for example, has an average altitude of ~4.2km above sea level and is about 1 km higher than the Altiplano plateau of Bolivia and Peru (~3.2km). In contrast to the Altiplano, the units that follow the Eastern Cordillera to the east are in addition, the Santa Barbara System and the Sierras Pampeanas thick-skinned foreland provinces.

The crustal structure of the Puna was studied using the seismic refraction method by Wigger et al. (1991). The crustal thickness, another feature for differentiating the Puna and Altiplano plateaus, was estimated by receiver function analysis as being ~ 55-60 km underneath the northern Puna, which is 10-15 km thinner than that of the Altiplano (Yuan et al., 2000). These

results agree with those of Götze et al., (1994) who postulated that the crustal thickness of the Puna should be less than that of the Altiplano, based on regional gravity models obtained for the Central Andes.

The presence of the Central Andean Gravity High (CAGH) (see Figure 5.1) has been also detected along the Cambro-Ordovician magmatic arc (Faja Eruptiva de la Puna Occidental in Coira et al., 1982). The extension of this anomaly, interpreted from isostatic residual values, represents an elongated ~N-S area that covers the city of Calama in Chile, the Salar de Arizaro and Salar de Antofalla salt pans and ends in the Salar de Pipanaco depression in the southern Puna (Goetze and Krause, 2002).

Young mafic magmatism in the southern part of the Puna has been one of the arguments proposed for distinguishing between both plateaus, supported by processes related to the delamination of a part of the lower crust and upper mantle, to explain a higher topography and a thinner lithosphere (Kay et al., 1994; Whitman et al., 1996).

The Puna also differs from the Altiplano in the fact that it does not present a well developed thin-skinned thrust belt to the east and has a more irregular surface (Allmendinger et al, 1997). The fact that the Puna surface is so irregular (Figure 6.5 -Chapter 6) has to do with a system of small closed basins that started to develop during Neogene times. A model presented by Riller and Oncken (2003) suggest that crustal segmentation of the Puna plateau into rhomb-shaped areas where the closed basins developed is responsible for localized shortening and surface uplift at both margins of the plateau. Such segmentation has produced a series of strike-slip faults limiting the structural blocks of the plateau. Some of these faults still show some seismic activity (Schurr et al., 1999; Schurr, 2000), mainly concentrated along the eastern border of the plateau and the OTL (Olacapato-Toro Lineament, displayed in Figure 5.1 as Olacapato-El Toro Fault Zone), a prominent shear zone that extends from the coast of Chile to the southeast in the proximity of Salta city in Argentina, that has registered historical seismicity on several occasions.

The addition of accretion wedges and marginal basins has not been an influence on the orogenic evolution. The uplift related to compression and crustal shortening of the Puna plateau was attributed to the increasing convergence rate and flattening subduction of the oceanic Nazca Plate, which started around ~20Ma and continued until the late Pliocene.

The plateau of NW Argentina has an early Paleozoic metamorphic basement composed by different sedimentary and magmatic units. Following compression and uplift of the plateau, a series of Palaeogene sediments deposited in the Puna foreland orogenic basins.

The filling of evaporite basins in the Puna Plateau occurred between the Neogene and the Holocene. In the Neogene magmatic arc two main types of volcanic activity developed. The andesitic and dacitic volcanism was continuous since about 20 Ma until the Quaternary and produced many of the well-known strato-volcanic complexes of the southern Central Andes. In the Central Andes between ~25 Ma and ~18 Ma the volcanic centres are well distributed across the arc and back-arc regions north of 22°S; south of 25°S the centres are confined to the arc front. Based on this distribution and the absence of volcanism during this time some authors have suggested a gap in magmatism between ~22°S and ~25°S (Coira *et al.*, 1993; Allmendinger *et al.*, 1997). The volcanic centres dating from Middle Miocene to Pliocene, are distributed over the whole Argentine Puna. The onset of large-volume dacitic to rhyolitic ignimbrite eruptions began in the late Miocene (ca. 12 Ma) (de Silva, 1989; Coira et al., 1993).

5.1.2. The Southern Puna

In the case of the Puna plateau, there are also some internal differences that enable a separation in northern and southern Puna. The northern Puna region, between ~22°S–24·5°S, is structurally separated from the southern Puna, ~25°S–28°S, by the NW–SE-trending Olacapato-Toro (OTL) lineament. North and south of the OTL, a system of parallel shear zones, considered to be zones of lithospheric weakness (Allmendinger et al., 1983, 1997), are responsible for a series of strato-volcanic edifices that account for the largest volcanoes of the Puna plateau (e.g. Llullailaco, Socompa, Ojos del Salado in the volcanic arc and Antofalla, Tuzgle in the back-arc) and include the highest volcanoes on Earth. In between these lineaments, back-arc volcanic activity is still present but not with prominent edifices (Figure 5.1).

The most significant north-south structural change in the back arc, along the eastern border of the plateau is the termination of the thin-skinned Subandean belt near 23°S. This change correlates with the end of Paleozoic basins and the superposition of the Upper Cretaceous rift

basins in the foreland south of 24°S (Allmendinger et al., 1983; Allmendinger et al., 1997), where the thick-skinned Santa Barbara System replaces the thin-skinned Subandean belt and south of 26°S where northern Sierras Pampeanas replace the Eastern Cordillera. Most of the Puna basement consists of Paleozoic rocks that exhibit several phases of deformation usually known as reworked pre-Cenozoic continental crust.

In the area of our profile at 25.5°S the Salar de Antofalla (SA), located to the east of the Antofalla volcanic complex, forms an elongated basin of salt filing deposits with important topographical differences with the rest of the plateau. Before the crustal thickening and uplift of the Central Andes during Neogene times, the SA area was part of the Andean foreland. The Southern Puna may have been part of a large region with low relief in which only minor sedimentation occurred until the Late Eocene. Later, the SA was incorporated to the Andean orogen, to the east of the magmatic arc of the early Tertiary subduction system. Pilger (1984) suggested the subduction of lower density, young and hot oceanic crust, to explain the flat subduction angle during this time, although today this idea is not completely accepted.

An increase in the convergence rate from ~28.3-25.8 Ma (Somoza, 1998) normal to the trench due to reorganization of the Pacific plate suggest a subduction angle less than 30° at this time (Kay et al., 1988 and 1991; Mpodozis et al., 1995). Between ~20-12 Ma regional compression and the onset of volcanic activity dominated in the Antofalla area. According to geochemical data, the melts erupted through a crust with a thickness of at least ~40 km. This indicates that regional uplift was in progress. For the period between 12 and 4 Ma, a series of intra-arc basins developed due to tectonic shortening while the strato-volcanic centres were still active. During Late Miocene to Pliocene times (< 9 Ma), alluvial fan sedimentation was interrupted by a period of relative tectonic quiescence. Between 6 and 4 Ma, the relative tectonic quiescence was accompanied by the eruption of intraplate-like basaltic andesitic magmas at monogenetic centres.

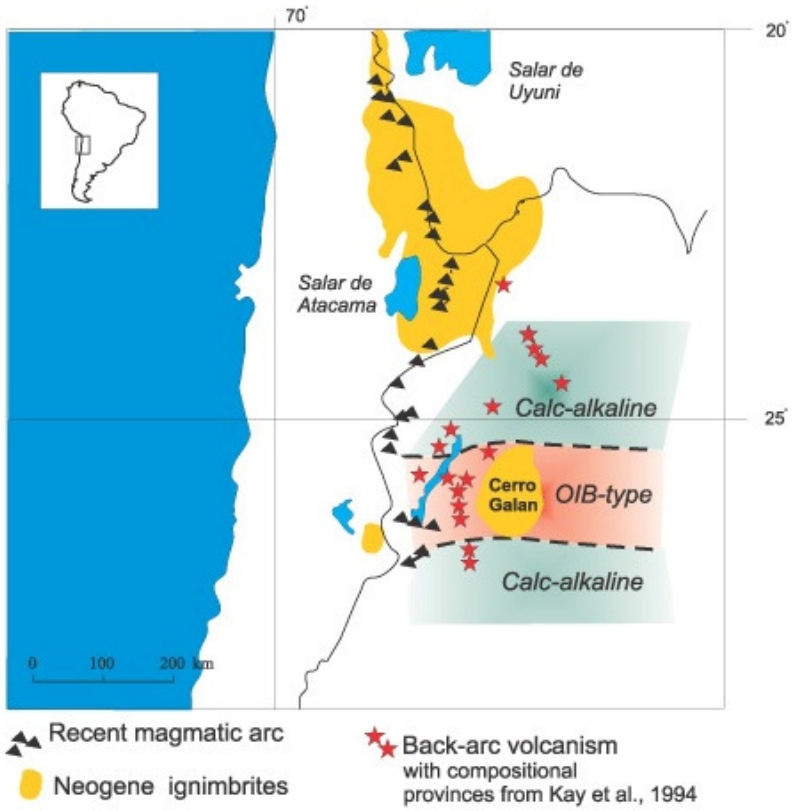

Figure 5.2: Map showing the distribution of volcanism in the Puna plateau where the lithospheric delamination is supposed to be strongest (beneath the OIB region) according to Kay et al. (1994).

The occurrence of intraplate-like volcanism has been usually associated with crustal heating, the generally higher topography and a thinner lithosphere of the Southern Puna compared with the Altiplano. From 4 Ma until the present, crustal thickening and uplift resulted from renewed contractional movements. Da Silva (1989), Francis et al. (1989) and later Kraemer et al. (1999) interpreted the large-volume ignimbrites as reflecting large-scale crustal melting due to crustal thickening and heating by basaltic intrusions The presence of the Cerro Galan collapse Caldera and its associated large ignimbrite deposits have been suggested by Kay and Kay (1993) and Kay et al. (1994) as a region for understanding delamination processes (Figure 5.2). Among the characteristics the authors consider, are the combination of factors such as uplift, stress regime and the different magmatic signatures compared with the rest of the plateau in the Galan area.

A difference in the composition of the extrusives parallel to the CVZ as used in figure 5.2 to explain basic type-volcanic deposits in the back-arc area may reflect the chemical characteristics of the fluids involved in upper-crustal melting. For the ascent of melts, Schurr et al. (1999 and

2003) proposed a model for the Puna at ~24°S where the ascending path for the fluids causes melting of the overlying mantle and suggested a strong horizontal component for melt ascent (Figure 5.3). This model was obtained from local tomography data from the PUNA 97 (Puna Untersuchung Nord Argentinien) seismological project. Results that correlate the Puna magmatic evolution with associated shortening on the Eastern Cordillera, and their influence on crustal thickness variations from north to south are still required to understand the present state of the plateau within the context of deformational processes.

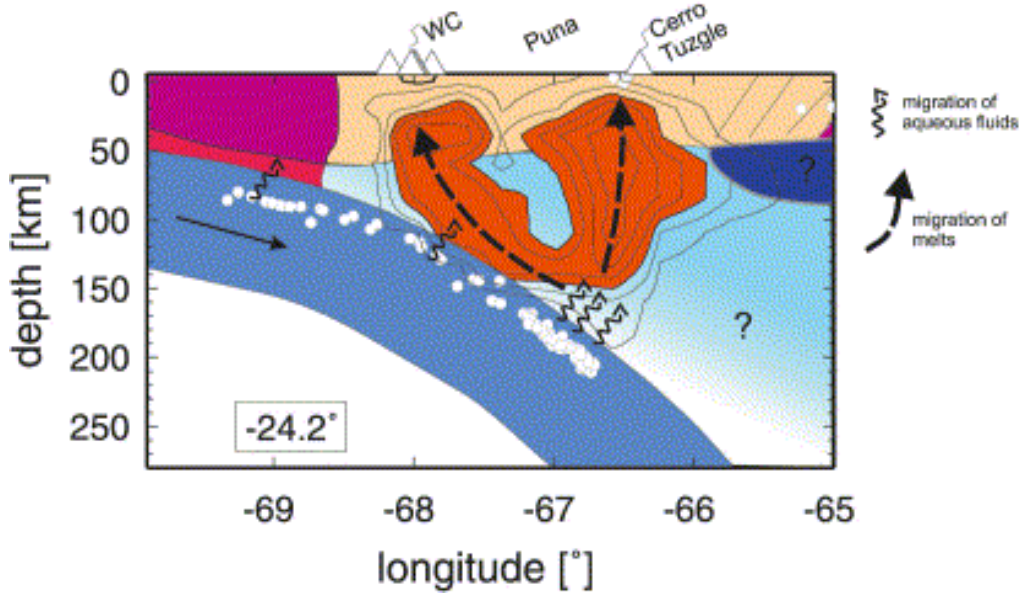

Figure 5.3: Fluid movement based on interpretations from of the PUNA project data. The ascent paths for melts that migrate through the mantle are shown in orange. Note the bifurcation of fluid patterns from the cluster of earthquakes between 150 and 200 km depth (From Schurr, 2000 and Schurr et al., 2003).

5.2. Results and Observations for the Puna plateau

The position of the profile and the most important salt-lakes (Salar) and volcanoes are displayed in Figure 5.4, along with the results from the inversion of P- and S- waves. Other tomographic results for P- and S- waves are presented in vertical and horizontal sections in the Appendix The morpho-structural units involved in the study area of the Puna plateau and its bordering regions are: the volcanic arc (CVZ) to the west at ~68° and the Eastern Cordillera (EC) to the east at ~66° (Tacuil).

The images obtained for the Puna plateau at 25.5° S show a strong low-velocity anomaly that virtually "emanates" from depths near ~200 km. This negative anomaly reaches the Moho discontinuity (~60km obtained with receiver function) as a single zone and then bifurcates or separates into two branches; one at the position of the CVZ and the other where the border of the plateau to the east is represented by some back-arc volcanoes (e.g. Galan). At the depth of the Moho discontinuity a broadening of the low-velocity anomaly is detected. The difference in temperature and composition below and above the Moho where accumulation of melts may occur, should cause heating of the lower crust leaving internal zones of weakness. The weakened crust affected by ductile deformation is then affected by the movement of partially melted material towards the surface.

From west to east it is possible to describe the following anomalies (Figure 5.4).

1- The region between 69°W and 68°W west of the Salar de Antofalla (SA) is characterized by low-velocities for P- waves. The anomaly region is located in the upper crust.

The low-velocities area; west of the Antofalla volcano seem to extend towards the main volcanic arc on the west and can be associated with a group of earthquakes at a depth of ~100 km. Unfortunately the upper part of this region can not be well resolved due to the limitations of the profile, but nevertheless, the shape of the anomalies suggests the presence of materials with low-relative velocities ascending towards the volcanoes of the CVZ (not displayed in Figure 5.4). An additional strong low- velocity anomaly in the upper crust at a depth of ~20 km is interpreted as part of a melting zone beneath the Antofalla strato-volcanic complex.

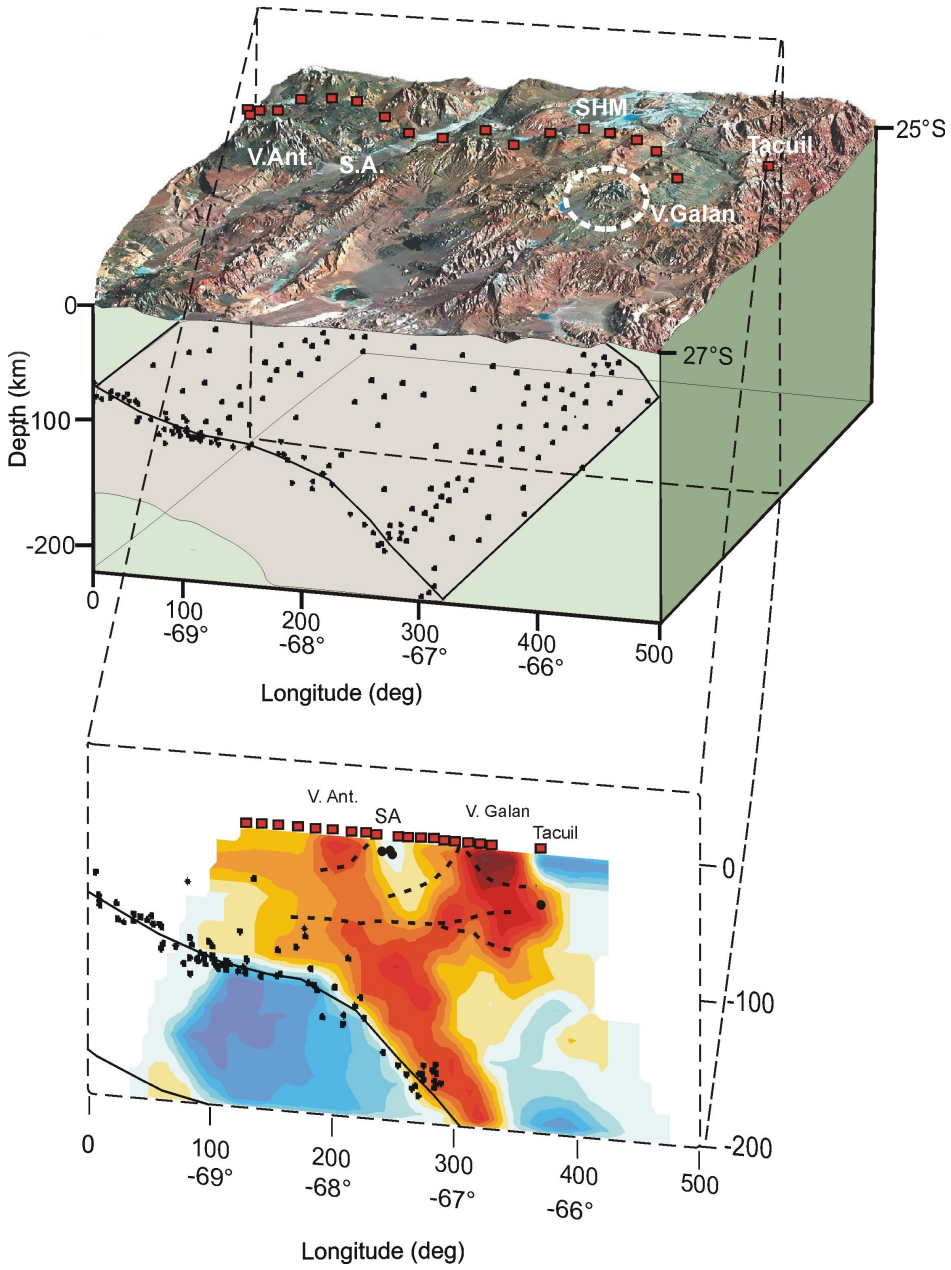

Figure 5.4: Block diagram showing the distribution of stations at 25.5°S (red squares) and the position of the slab inferred from earthquake hypocenters (Engdahl et al, 1995). The tomographic section represents P- wave results. Receiver function Moho and crustal discontinuities are plotted along this section. V. Ant.: Antofalla Volcano, SA: Salar Antofalla, V. Galan: Galan Volcano.

2- The Salar de Antofalla is related to a high-velocity anomaly in the upper crust and is located between low-velocity anomalies. The long shape of this NE-SW trending salt pan, the topographic differences between the surface of the salar (~3400m), the surrounding ranges (~4000m) -*see Figure 6.5, chapter 6* - and its narrow basin (max. 10 km) could be related to deep reaching structures delimiting not only the presence of this block but inducing the

divergence in velocity anomalies at this latitude. The location of intra-crustal seismicity is also plotted and interpreted as consequence of deep reaching structures (faults) limiting the salar.

3- A low-velocity anomaly is located at ~67°W and seems to correlate well with the presence of the Cerro Galan volcano on the surface. The extension and depth of this anomaly is probably interrupted due to the presence of a high-velocity structure on the eastern border of the plateau.

4- The high-velocity anomaly beneath the Tacuil station, at the eastern end of the profile, is interpreted as the western ranges of the Eastern Cordillera, which seem to indicate a sharp change in velocities. The limit between positive and negative velocity anomalies west and east of this range is clearly represented by Palaeozoic granitic and metamorphic units in the upper crust, with higher velocities to the east of 66.5W.

Chapter 6

Discussion and Conclusions

As outlined in chapter 3, the present data analysis is based on the teleseismic tomography approach in which a slice from a three–dimensional (3-D) object gives us information about its two-dimensional (2-D) properties. The discussion here presented is based on the interpretation of these "slices" along two profiles in the Central Andes. The described properties and velocity anomalies are restricted to our observation profiles. Therefore, no 3-D interpretation is performed for the present data as it is not possible to speculate about the extension these anomalies have north and south of our study areas at 21°S and 25.5°S.

6.1. The Altiplano anomalies

The results for both *P*- and *S-wave* analysis correlate well and show good agreement with the low- relative velocities at zones of incipient melting (Heit et al., submitted). We see a strong low-velocity anomaly that has the aspect of a layer extending from the west to the east beneath the Central Volcanic Zone (CVZ), the Altiplano plateau and the Eastern Cordillera. This anomaly is flanked by two high-velocity anomalies: one on the western side, corresponding to portions of the interacting Nazca and South American plates (fore-arc) and the other on the east related to the boundary between the Eastern Cordillera and the Interandean, Subandean, Chaco Plain and parts of the non-exposed Brazilian shield (Figure 6.1).

Between the CVZ and the West Fissure (WF), a low-velocity anomaly (QBBS) is observed and interpreted as the origin of fluids associated with the melting in the mid-crust responsible for volcanism in this part of the subduction zone. The ascent of fluids at the border of the Altiplano (Schurr et al., 2003) around the CVZ could be related to the presence of the WF that acts as a natural thermic border between blocks of different temperature. Schurr et al. (2003) found similar results for the Atacama Block in the south of our study area. The rising fluids associated with faults delimiting the QBBS are interpreted by ANCORP Working Group (2003) as the origin of this highly-reflective anomaly.

It is also possible to detect, above the subduction zone and below the Moho at ~68°W, a low-velocity zone interpreted here as partially melted mantle material (see Figure 6.1) possibly generated as a consequence of dehydration of the subducting slab and hydration-melting of a heterogeneous mantle wedge. The progressive heating of the base of the crust should affect the interior of the crust where MASH processes may occur. The MASH standing for Melting Assimilation Storage and Homogenization process was defined by Hildreth and Moorbath (1988) for those zones of possible remelting in the lower crust that produce tonalitic magmas that may differentiate later on their way through the continental crust. Results obtained by other authors also support the presence of this "underplating-like" structure (Lamb and Hoke, 1997). Another possibility for the existence of this anomaly is the presence of hot asthenospheric mantle material that accumulated at the base of the crust

The Uyuni-Kenayani Fault Zone (UKFZ) is a prominent fault system that penetrates the upper portions of the crust and reaches segments of the lower crust (in Mertmann et al., 2001 – see Figure 4.6) and correlates with a low-velocity anomaly observed at 67° W, in accordance with the results presented here and those of other authors (Yuan et al., 2000; ANCORP Working Group, 2003; Haberland et al., 2003). This low-velocity anomaly may be related to the upper limit of a partially melted intra-crustal body that coincides with the prominent layer called the Low-Velocity Zone or Altiplano Low Velocity Zone (LVZ or ALVZ) (Yuan et al., 2000).

A continuation of the ALVZ to the west correlates very well with the presence of the volcanic arc but nevertheless the most important fluid portions appear to be present underneath the Altiplano-EC border region. The anomalies in the west between ~68°W and ~68.5°W could be interpreted as a part of the ALVZ, probably not well defined due to the low resolution of the

detected anomaly at depth. To the east, this LVZ appears to reach as far as 65.5° W at the easternmost part of the EC. The extension and presence of this layer of melted material could be explained in accordance with geological features such as the Main Andean Thrust (MAT) (e.g. Allmendinger et al., 1997; Mertmann et al., 2001; Scheuber et al., Submitted). The MAT is a prominent detachment zone located at the border between the EC and the Inter- Subandean provinces and could be affecting the entire portion of the upper crust (see Figure 4.6). We can speculate that the MAT represents a fault zone where changes in lithostatic pressure, temperature and mineralogical variations take place, encouraging, the movement of fluids and melts at greater depths. The role of the QBBS and the ALVZ as a potential decoupling surface and the thermally controlled weakening of the crust were suggested by other authors (e.g. Elger, 2003; Victor et al., 2004; Elger et al., 2005) as a possible subhorizontal shear zone transferring shortening eastward along a decoupling surface. In this case the MAT seems to be acting as a decoupling surface, probably reaching the ALVZ.

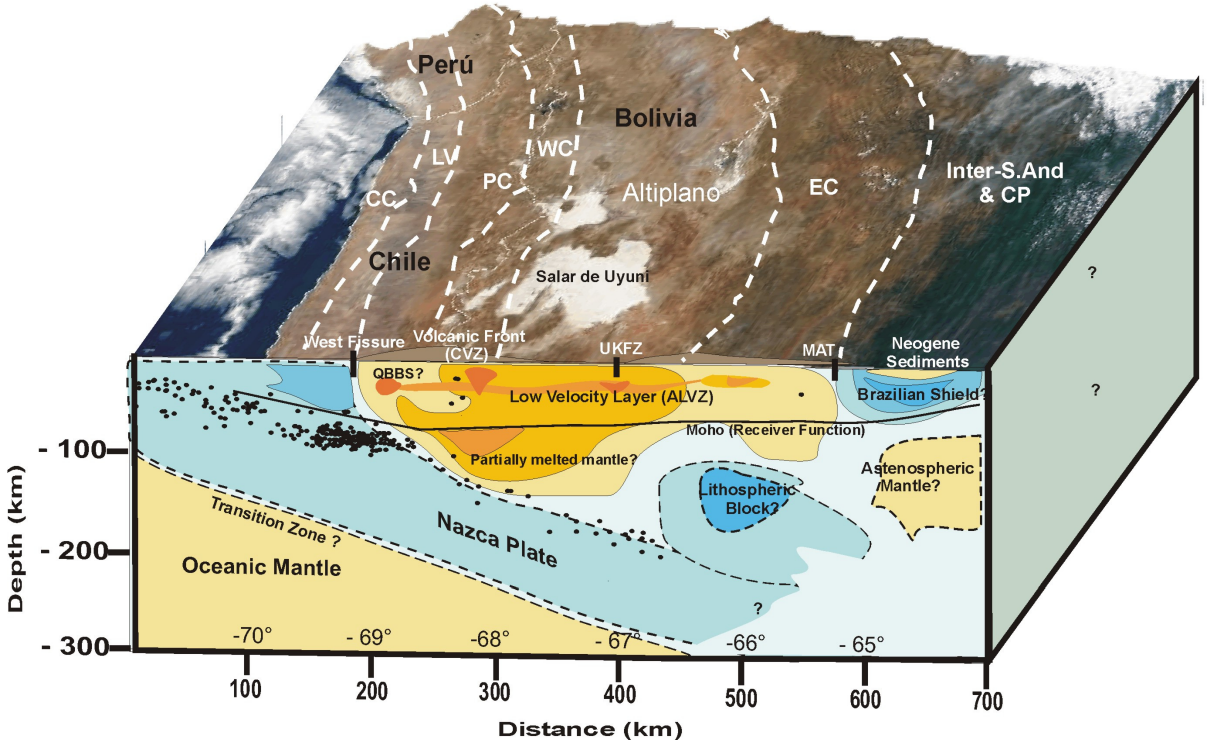

Figure 6.1: Schematic cartoon at 21°, representing the combined P- and S- wave results. Receiver function Moho (Yuan et al., 2000). CVZ: Central Volcanic Zone; QBBS: Quebrada Blanca Bright Spot; UKFZ: Uyuni-Kenayani Fault Zone; MAT: Main Andean Trust; ALVZ: Altiplano Low Velocity Zone. The positive anomaly to the east of the profile has been interpreted as the Brazilian Shield covered by Neogene and Quaternary sediments. The necessity of a Transition Zone above the oceanic mantle, beneath the subducting slab, is deduced from the variations in both P- and S-wave analysis. The Morphological units: CC: Coastal Cordillera; LV: Longitudinal Valley; PC: Precordillera; WC: Western Cordillera; EC: Eastern Cordillera; IA: Interandean; S.And: Subandean; CP: Chaco Plain.

To the east of our study area, we detected the presence of a high relative-velocity anomaly at ~65°W correlating well with the eastern end of the EC. This cold, high velocity unit could be indicating the presence of the Brazilian shield underlying the Interandean, Subandean and Chaco Basin provinces. The presence at this longitude of the Brazilian shield (BS) has also been proposed by other authors (Wigger et al., 1994; Watts et al., 1995; Lamb, et al., 1997; Lamb and Hoke, 1997; Beck and Zandt, 2002) and we believe that the strong Brazilian shield is the basement that supports the eastern morphological units and acts as a backstop that imposed shortening-uplift at the eastern border of the Andean chain.

The evolution of the Altiplano (e.g. Isacks, 1988; Gubbels et al., 1993; Allmendinger and Gubbels, 1996; Allmendinger et al., 1997) started at about 25Ma and went through a series of diastrophic phases that ended with the last uplift and deformation of the plateau at about 9-5Ma (e.g. Allmendinger et al., 1997). The shortening ceased in the Altiplano and shifted to the east, where the Brazilian shield is located, having a counter-effect that could be responsible for the final closing stage of the Altiplano basin and the present-day aspect of the plateau. At the same time, shortening in the Puna plateau continued up to 1-2 Ma (Allmendinger and Gubbels, 1996; Allmendinger et al., 1997) and could be interpreted as a delayed tectonic reaction proving, in this case, that the distance that separated the Puna plateau from the shield may have been bigger than in the case of the Altiplano. In other words the Puna had more time and space to continue its evolution.

However, we are unable to see the subduction of the Brazilian lithosphere as suggested by other authors (Wigger et al., 1994; Watts et al., 1995; Allmendinger et al., 1997; Lamb et al., 1997). The ideas of a subducting lithosphere can not be confirmed with the present data. The strong changes in velocities observed in the upper crust indicate that the transition between the Precambrian Brazilian shield and the morpho-units to the east is abrupt and probably related to major structures in the upper crust.

Many authors interpret Andean uplift as being the result of various interacting factors (Isacks, 1988; Cahill and Isacks, 1992; Wigger et al., 1994; Allmendinger et al., 1997; Lamb et al., 1997; Lamb and Hoke, 1997) but the remaining issues concerning lithospheric thinning, magmatic addition, stability of the plateau and the amount of shortening are still not well constrained. The movement or displacement of the basal parts of the lithosphere is usually proposed to explain the

high elevation of plateaus. We believe that the high-velocity anomaly for the Lithospheric Block (100 km -150 km depth) between ~67°W and ~66°W in fact indicates the removal of the base of the lithosphere.

Observations by Hoke et al. (1994) postulated the existence of a thin lithosphere at 20°S for parts of the Eastern Cordillera, to explain the elevated ^{3}He signature in the geothermal systems. The distribution of velocities at the base of the crust and upper mantle suggest that there could be an influx of materials from the asthenosphere that affects the base of the continental crust. Myers et al. (1998) detected the presence of a zone of low Qs (~100), in the same area, that they interpreted as being evidence of near solidus conditions. If this is the case, we will expect to see a shift of the isotherms at this point, probably related to the removal of the high density base of the lithosphere(e.g. Beck and Zandt, 2002). Delamination has already been proposed by other authors (Bird, 1979; Housemann et al., 1981; Kay and Kay, 1993; 1994; Withman et al., 1996; Kay et al., 1999; Schurr, 2000) to explain the absence of a mantle lid and the rapid uplift of the Tibetan and Puna regions that produced stable plateaus over a long period of time. With this type of model, thick and cold lithosphere delaminates from the base of the crust and sinks into the mantle. Our model, presented in Figure 6.1, supports this idea for the Altiplano area. We will discuss about this particular phenomena of *delamination* in section 6.4.

6.2. The Puna anomalies

The Argentine Puna is a key region for understanding the evolution of the Central Andes and particular characteristics that are observed in our profile bring to light some questions concerning the distribution of anomalies in correlation with morphological units.

A similar distribution of positive and negative relative velocity anomalies are observed as for the Altiplano previously discussed area: low-velocity anomalies at both flanks of the Puna and a high-velocity structure on the eastern border of the plateau. However, a difference from the Altiplano is observed in the central part of the Puna plateau where a high-velocity zone is present beneath the area of Salar de Antofalla (SA) (Figure 5.4). This high-velocity anomaly has been interpreted by Goetze and Krause (2002) as a part of the Central Andean Gravity High (CAGH) that is believed to include some of the ultrabasic rocks that form the “Faja Eruptiva Occidental”

(an Early Paleozoic magmatic arc) (in Coira et al., 1982).

The CAGH is a dense body about 400 km long and 100 km wide that lies at depths between ~10 and ~40 km (see Figure 5.1). A good correlation is observed for the tomographic section where low-velocities coincide with negative residual anomaly values (under volcanoes) and high-velocities correlate with positive residual anomalies (between the Antofalla and Galan volcanoes). The negative anomalies reflect reduced densities related to fluids and/or melting below the volcanoes. The positive anomalies are related to places where there is no melting/fluids, i.e. between the volcanoes where the Salar de Antofalla is located (Hackney, *pers. comm.*) (Figure 5.4).

The western border of the Puna profile shows what we interpret as the effects of ascending melts that correlate well with the position of the volcanic arc (CVZ). The negative anomalies on the eastern border of the Puna plateau may be related to a trend of volcanic edifices from north to south where some of the back-arc volcanoes are located (e.g. Tuzgle, Qevar, Galan). Observations by Schurr et al. (1999 and 2000) found high attenuation (low Qp) beneath the Tuzgle volcano to the north of our study area that may be included in the before mentioned trend.

The variations that are observed on the eastern side of the profile (border region between the Puna plateau and the Eastern Cordillera) could be related to a ductile lower crust that becomes thicker under a compressional regime. This has been also proposed by Kley and Monaldi (1998) to explain shortening in the north of Argentina and the south of Bolivia. The high velocity in the east is then related to the presence of intrusive and metamorphic Paleozoic rocks that "separate" the plateau from the Eastern Cordillera. The limit imposed by such an old structure could be responsible for the sharp difference in relative velocities west and east of the Luracatao-Tacuil ranges. A difference in temperature for intra-crustal rocks would play a role in the distribution of weak-zones for the ascent of fluids and magmatism that is observed in the back-arc volcanoes (e.g. Tuzgle, Qevar, Galan), where the signature and distribution of volcanic activity on the eastern side of the plateau suggests this situation.

In Figure 5.1 the edge of the Puna plateau is plotted and correlates well with the change in velocities and temperatures observed for both P- and S- waves. The most important back-arc

volcanoes are located where these NW-SE trending lineaments intersect the structure that represents the border of the plateau (~NE-SW). Hence, we suggest that deep reaching fault systems associated with shortening, on the east of the plateau, are the conduits for back-arc volcanism concentrated on the eastern margin of the plateau. The fault systems originate in the brittle zone of the crust and propagate to the ductile zone or vice versa.

To explain the shape of the branched anomalies emanating from both clusters of events at ~100 and ~200 km (Figure 6.2), it is necessary to consider the geodynamic location of the southern Puna that represents the final portions of the plateau and is located in a transitional area involving flat-slab subduction.

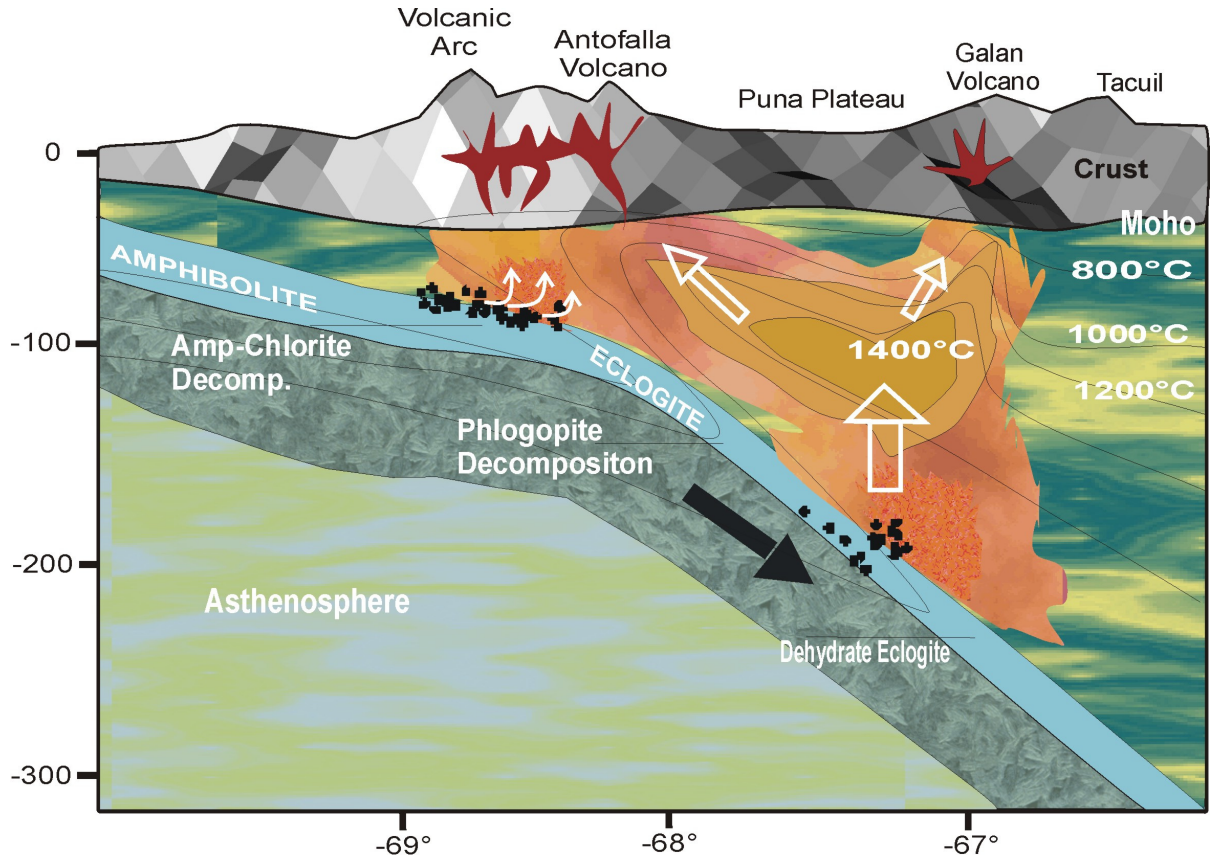

Figure 6.2: Cartoon showing the interpretation of the combined results from P- and S- wave tomography with a branched ascent path for fluids/melts rising from the Benioff zone (clusters of earthquakes) at depths of ~100 km and ~200 km. The anomalies detected in our study suggest that the presence of a highly hydrated oceanic crust is related to the thermal variation caused by an incipient flat area that enables the release of fluids at greater depths than usual. The aspect of the ascent paths can be the associated with a return flow type model for setting the fluids in movement. The position and distribution of isotherms play a very important role, as the high-T° isotherm of 1400°C should induce a flux of melted material towards the volcanic arc or nearby volcanoes as Antofalla.

The reasons for the presence and evolution of a flat-slab are still not well understood. A possible cause usually suggested for explaining this situation is the fact that the Nazca oceanic plate and its lithosphere are relatively young, thin and possibly buoyant. Other results associate the flat-slab areas on both flanks of the Central Andes with the buoyancy of anomalously thick oceanic crust where the aseismic ridges are present (e.g. Carnegie, Nazca and Juan Fernandez (e.g. Cahill and Isacks, 1992; Kay and Abbuzzi, 1996; Gutscher et al., 2000). In contrast, Lamb and Davis (2003) suggest that the flat-slab zone in the Andes is associated with climatic changes along-strike that leave zones of low shear stress where trench-sediment fill lubricates the subduction system, leading to a low angle subduction zone. Meanwhile, zones of high shear stress where the trench sediments are absent lead to normal subduction. In any case, the presence of the flat-slab area to the south of the Puna plateau indicates that the thermal state and heat-flow models for the lithosphere and asthenosphere must be affected by the presence of an unusually shallow oceanic lithosphere. It is also expected that these thermal variations associated with a down-going slab that remains at shallow depths will retain more water that can be later released at progressively greater depths (Figure 6.2).

6.2.1. Fluids and temperature in the mantle under the Puna.

The role of water is important for lowering the melting point of the overlying rocks particularly in those regions where a hydrated slab release water due to phase transformations such as amphibolite to eclogite at 100 km depth. The dehydration of amphiboles is however, a pressure-dependent effect more than a temperature dependent one (Schmidt and Poli, 1998). In all cases, the oceanic lithosphere experience progressive heating and pressure changes due to the subduction and releases the remaining portions of water from the eclogite at a depth of ~200-250 km, where the initial melting should also take place at these depths (Schmidt and Poli, 1998). By successively adding H_2O to the overlying mantle, the partially molten zone must grow upwards. Assuming the position of a high temperature isotherm (e.g. 1400°C), one would expect to see a movement of mantle material towards the volcanic arc. Some of the models of thermal activity in subduction zones show that high temperature isotherms, about 1300ºC, must be located beneath the volcanic arcs and that the depths of the subducting slab surface beneath the volcanic front are in accordance with such isotherms (Schmidt and Poli, 1998).

In the case of the Puna, all andesites and some ingnimbrites always have some mantle material for arc and back-arc volcanoes, such as the Tuzgle and Cerro Galan areas (Lucassen, *pers. comm.*). For explaining the presence of mantle material in volcanic rocks, a thermal anomaly in the asthenosphere is suggested as in Figure 6.2 (e.g. 1400°C isotherm). This thermal anomalous zone would also be responsible for the aspect and distribution of the ascending paths for melts that separate into two branches where the lithosphere-asthenosphere boundary is expected (100-130 km). The presence of a return-flow for fluids leaving the slab at the Benioff zone can be described on the basis of our interpretations and hence, fluids that leave the Benioff zone will ascend parallel to the surface of the oceanic slab, due to physical forces associated with subduction and temperature variations and/or make their way to the surface (or base of the crust) in a more or less vertical manner (Figure 6.2).

Is it possible that water remains in the eclogite that reaches the final step of dehydration at depths of ~200 km? This depends mainly on the thermal stability of the hydrous minerals. At a given temperature the mantle does not need too much fluid to trigger large amounts of melting. The suggested position of the isotherms showed in Figure 6.2 should reflect the behaviour of the peridotite at the lithosphere-asthenosphere boundary (LAB). Small amounts of water in olivine will change the physical properties of this major component in mantle rocks, in the way that changes in viscosity and ductile flow may occur at much lower temperature than indicated in most standard subduction zone models (Schmidt and Poli, 1998). Having near-solidus or melted material in the mantle does not necessarily imply having a defined large scale flow pattern, since thermal or density inhomogeneities can also define local small scale flow patterns that transmit the movement to other portions of the mantle where the final transformations deliver fluids that ascent towards the base of the crust. The plateau will therefore be affected by a thermal influx from below, induced by water movement that lowers the melting point of the neighbouring rocks. These thermal anomalies in the asthenosphere keeps the plateau elevated over a long period of time without the necessity of delamination. On their way to the surface, the melts and fluids can form melting zones in the upper crust below ~20 km. Information about the thermal expansion of the Central Andes might still be needed to confirm this statement.

It has been suggested that only a small portion of the water initially contained in the subducting lithosphere will escape from the slab in the depth range suitable for magma formation and that a large portion of the water will be dehydrated at relatively shallow levels (Schmidt and Poli,

1998). This effect should occur in the oceanic crust at depths of ~80 km, depending on the temperature of the subduction zone, where certain phase transformations allow minerals to retain some percentage of water (e.g. minerals as lawsonite-eclogites in cold subduction areas and zoisite-eclogite in warm subduction areas). If any of these minerals, according to their stability, is able to reach deeper portions of the asthenosphere, then a part of the water will also be able to descend to greater depths and will be lost for arc volcanism (Schmidt and Poli, 1998). In our case, for the Puna plateau we speculate that the water delivered to the system from the subducted slab at about 200 km is related to the decomposition of minerals that takes place between the phlogopite decomposition depths (~150 km) and the final dehydration of the eclogite (lawsonite and phengite phases) at depths of ~300 km.

In cold subduction zones, where the stability fields of some hydrous phases and serpentine overlap, water will be transported to greater depths and will not be available for arc magmatism (phlogopite decomposition in Figure 6.3), playing maybe a role in the evolution of back-arc volcanism as observed in the Central Andes. In relatively warm subduction zones fluids will be delivered from the dehydration of serpentine (Schmidt and Poli, 1998).

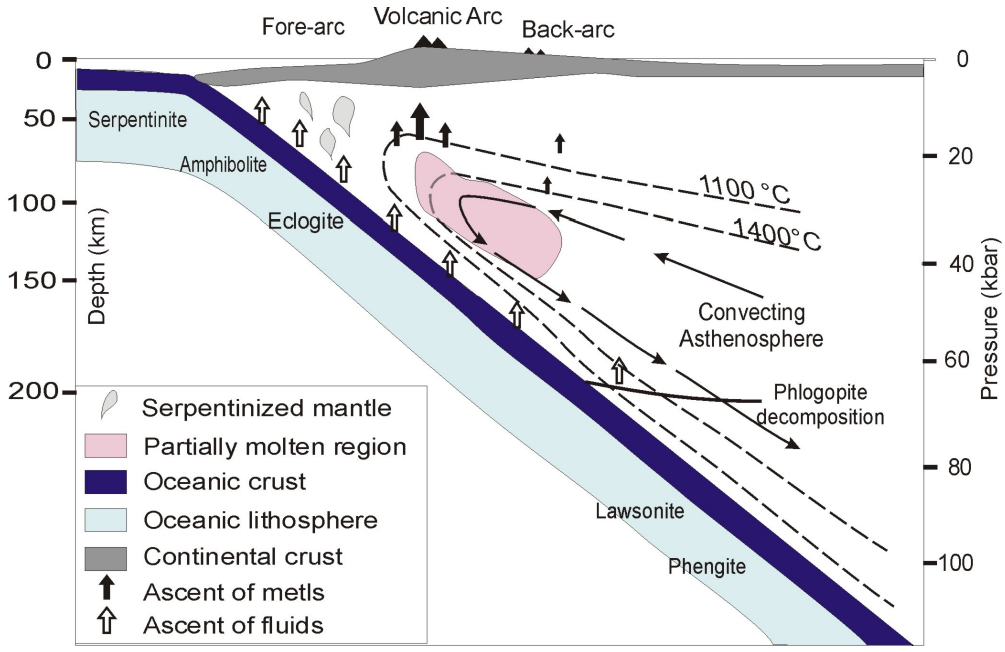

Figure 6.3: this diagram after Schmidt and Poli (1998), shows a possible model for the formation of a volcanic front. Open arrows indicate the rise of fluid, short solid arrows indicate rise of melts. Long arrows indicate flow in the mantle wedge. The diapirs represent a partly serpentinized mantle. Phase transformations at 200 km depth are directly related to the thermal state of the subducting plate.

As shown in Figure 6.3, the dehydration from peridotite and oceanic crust occurs at almost any depth to ca. 150–200 km, with water generally available above the subducting lithosphere. The region in the mantle, where partial melt is indicated, will therefore play a significant role in the movements of the melts towards the crust, so that the volcanic arc will develop above those areas where the amount of melt is sufficient to give rise to arc magmatism.

Continuous water release to depths greater than 200 km due to the breakdown of lawsonite and phengite will ensure the formation of hydrous peridotite in the mantle wedge via the direct release of fluids towards the overlying mantle (Poli and Schmidt, 1995) as suggested in our cartoon (Figure 6.2). A return-flow type model for the Andes, based on our observations seems to be the most possible case for explaining the movement of fluids towards the crust, while other authors suggest, that a corner-flow model as the driving mechanism for the type of tectonics can be discarded as it induces an excessive stress regime on the overriding plate (Husson and Ricard, 2004); without a significant corner-flow below the volcanic fronts mantle wedge temperatures would rapidly cool down and arc magmatism would cease (Schmidt and Poli, 1998). Both examples reflect how little these mechanisms are understood.

Romanyuk and Rebetsky (2000) analyzed the density and rheology of the down going oceanic crust of the Nazca plate and the importance of fluids in the weakening of mantle minerals. They suggested a model where the subducting plate is composed of two layers, one mainly of basalt and the other of gabbro being the later denser than the first (2.8-g/cm ^{3} basalt and 2.95-g/cm^3 gabbro); with density increasing with plate depth. The Nazca plate mantle is believed to consist of harzburgite, which is gradually replaced by spinel-lherzolite at greater depths. Where the oceanic crust experiences dehydration and metamorphism, the basalt–eclogite transition provides significant amounts of fluid that are released by the oceanic plate. This fluid leads to the serpentinization of the mantle and to the “wet” melting of the mantle wedge peridotites that form the volcanic arc (Davies and Stevenson, 1992). These ideas also support our interpretation cartoon from Figure 6.2.

The analysis of noble gases (e.g. Helium) released as bubbles in geothermal springs or contained in olivine crystals of mafic rocks, provide a clue as to the volatile components origin. This simple method illustrates the degassing signature of ^{3}He and shows that there are two main factors that govern the helium degassing rate and isotopic evolution in a mantle undergoing

whole mantle convection: (1) the ocean crust formation rate, and (2) the concentration of helium in the mantle (Class and Goldstein, 2005). Therefore, a distinctive signature for volatiles that have a mantle or crustal origin can be obtained.

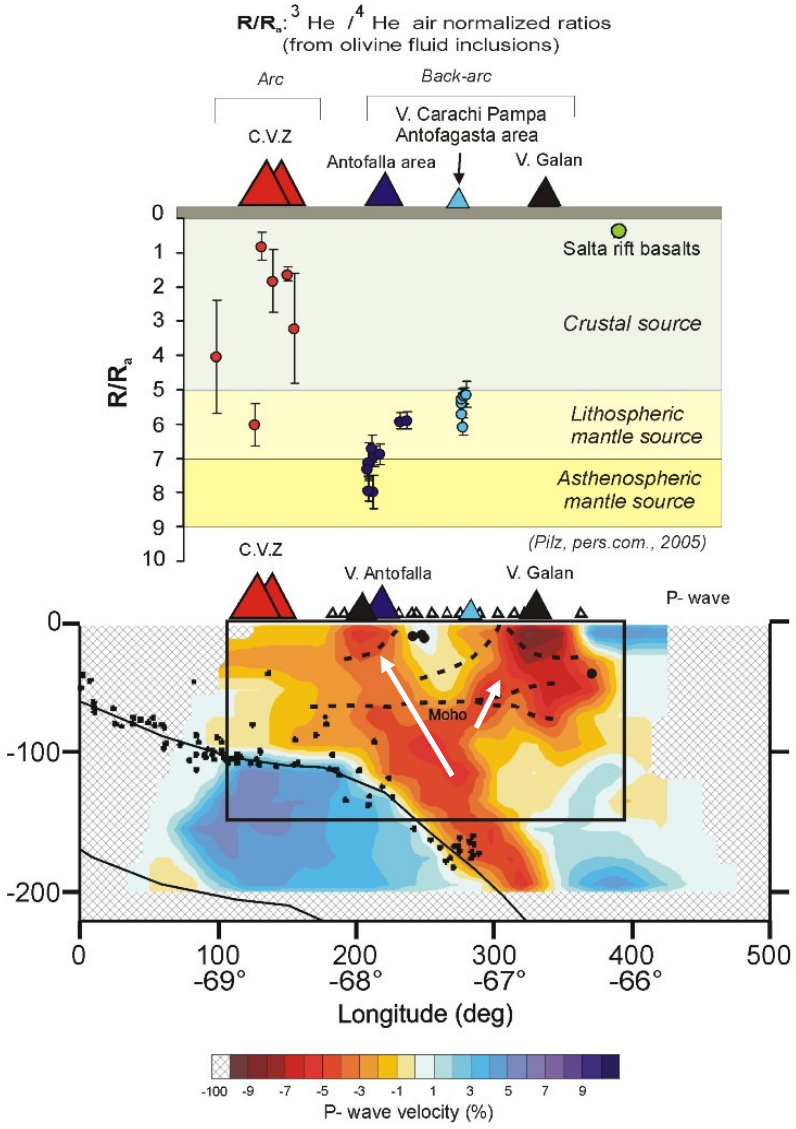

Figure 6.4: ^{3} He / ^{4}He analysis from olivine inclusion (Pilz, pers. comm., 2005) and one of our teleseismic tomography sections (P- waves). Long white arrow: fast ascent of hot melts with little contamination; Short white arrow: slow ascent of colder melts with higher crustal contamination. Rectangle shows the area of comparison. Moho topography and crustal structures from receiver function data.

By comparing our results with ^{3} He / ^{4}He air normalized ratios, we see a strong correlation between the plotted values for the area of the volcanic arc that suggest a crustal source of the volatiles with our interpretations of the observed anomalies related to the group of earthquakes at ~100 km. Towards the east of the CVZ, ^{3} He values for the Antofalla volcano show a deeper

source located in the asthenospheric mantle, with a few values indicating a shallower origin. East of the block from Salar de Antofalla, where the Carachi Pampa volcano is located, the ratios indicate lithospheric to crustal sources. This evidence can be used to reinforce our previous explanation that the branched-shape anomaly represents melt ascent paths towards the volcanic arc that in some cases reach the surface with less crustal contamination caused by the influence of unusual high temperatures (1400°C isotherm) or by favourable fault zones guided ascent. To the east, the materials reach the base of the crust at lower temperatures (~800°C) and experiences greater crustal contamination (Figure 6.4)

We are not able to observe clear evidence for delamination or its remnants in the analyzed section. Receiver function data (RF) for our profile does not show crustal variations that could be interpreted as being affected by such a process. The Moho depth remains more or less constant between 60 and 65 km. The eastern side of the RF profile shows a double layered Moho interface, with one surface above and the other below 65 km. Since this is the border area of the Puna plateau, we interpret this as a place where the shortening of the Eastern Cordillera affects portions of the entire crust.

6.3. The Role of Delamination in Andean Evolution

The role of lithospheric delamination has been proposed in recent years to explain the rapid uplift and thin lithosphere with the associated magmatism in the Puna Plateau (Kay and Kay, 1993; Kay et al., 1994; Schurr, 2000; Schurr et al., 2003). This process remains controversial as it involves the removal from lower portions of the crust and upper-most lithosphere that “detach or delaminate” and sinks into the asthenosphere. The process of delamination must be related to density increase in the mafic lower crust (basaltic crust at the Moho discontinuity), changes in mineral composition and thermally-anomalous materials.

When modelling the South American subduction zone, Sobolev and Babeyko (2005) presented lithospheric delamination as being triggered by the gabbro-eclogite transformation in a thickened continental lower crust. Mechanical failure of the sediment cover at the margin of the plateau, where the BS is located, should be the leading process in the mechanical weakening of the overriding plate during tectonic shortening. Active delamination, in their opinion, impedes corner-flow by delaminated material that intensifies shortening as a result of increased coupling

between the plates and the mechanical weakening of the overriding plate. In their model, the trench (roll-back) has also been migrating westward, contributing to the delamination and shortening that they interpret as a major factor on controlling Andean orogeny.

In our study we are able to see the effects of some sort of delamination in the Altiplano plateau (Figure 6.1) where we interpret the presence of a lithospheric block for explaining high-velocities at depths of ~150 km. The shape of the high-velocity anomaly detected below the Altiplano can be supported by the model showed in Figure 6.5. For the Puna region, at 25.5°S, we are not able to see a similar effect that could be interpreted as delamination of the lithosphere.

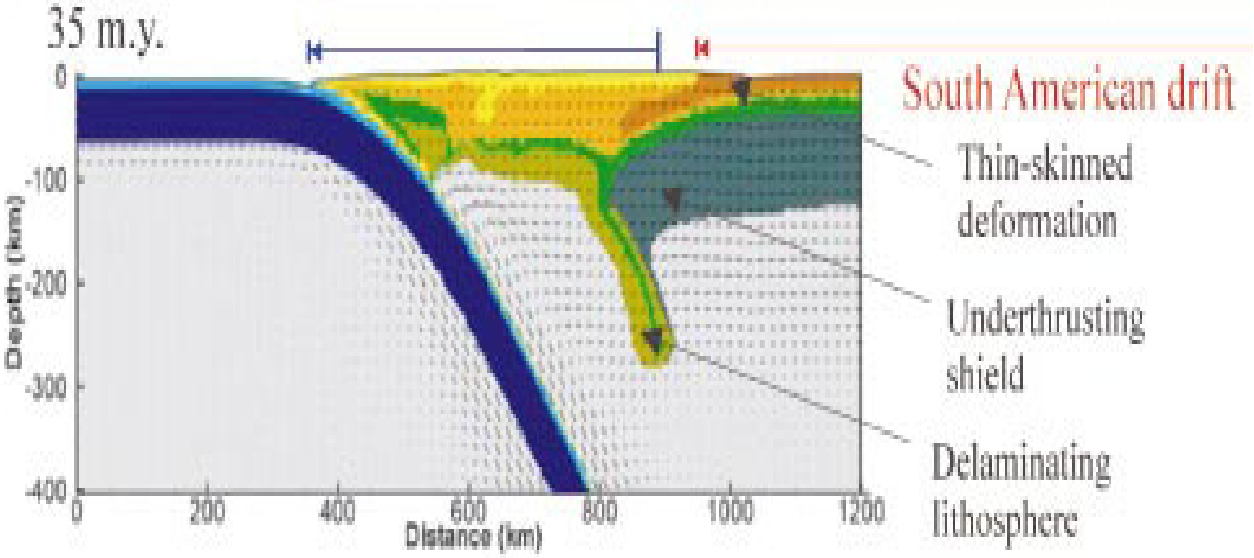

Figure 6.5: After 35 Ma the evolution of the Central Andes show an important drift of the continental plate to the west and effects of delamination in the back-arc area. An incipient underthrusting of the shield can also be seen (Sobolev and Babeyko, 2005)

For considerations about the thickness of the crust for both plateaus –a thicker Altiplano crust was usually proposed for differentiating between Altiplano and Puna- we use the receiver function images obtained from present data as explained in the next section.

6.4. Receiver Function data and the tomographic images

The receiver function (RF) method is based on the fact that teleseismic waves passing through a seismic discontinuity convert part of their energy to S- waves which arrive at the station after the onset of the P- wave within the P- wave coda. By analyzing the energy released during the conversion from P- to S- waves it is possible to detect some discontinuities beneath the station,

for example the Moho. The different aspects of the receiver function method and the quantification of the data is outside of the focus of this work. For more information the reader is referred to the literature cited at the end of this work (e.g. Yuan, 1999; Yuan et al., 2000; Yuan et al., 2002).

The results from teleseismic tomography are compared with receiver function images obtained from the analysis carried out in our group at the GFZ using the same data set. For the first time, the final results of the Moho discontinuity at ~21°S (Altiplano) and ~25.5°S (Puna) are obtained from our data and show a good correlation with tomographic images and previously obtained RF images (Yuan et al., 2000; Yuan et al., 2002).

In the case of the Altiplano, it is possible to see a uniform Moho discontinuity that goes from depths of ~75 km beneath the volcanic arc, thins beneath the Altiplano to ~65 km and thickens again below the Eastern Cordillera region to 75-80 km. To the east the Moho flattens to depths of ~50 km between 65°W and 64°W. The subducted slab can be clearly seen down to a depth of ~120 km, while at greater depths it is only inferred by the position of some interfaces that are not properly defined. The presence of a low-velocity anomaly in the upper crust can be seen as a zone of horizontal extension along a large part of the profile (Figure 6.6, centre and bottom in the case of the Altiplano).

For the Puna area, the Moho discontinuity beneath the plateau remains flat at about ~60 km. We are not able to see the portions of the Moho beneath the volcanic arc due to the limited extent of the profile. To the east, below the border between Puna and the Eastern Cordillera, the Moho is not well resolved, but a thickening beneath the Galan volcano area at ~67°W is expected, as in the case for the Altiplano profile. The slab cannot be detected in this RF image. Meanwhile, the presence of internal structures in the crust remains a subject of discussion, but nevertheless, there is a good correlation between those structures and the limits of low- and high- velocities in the tomographic images (Figure 6.6).

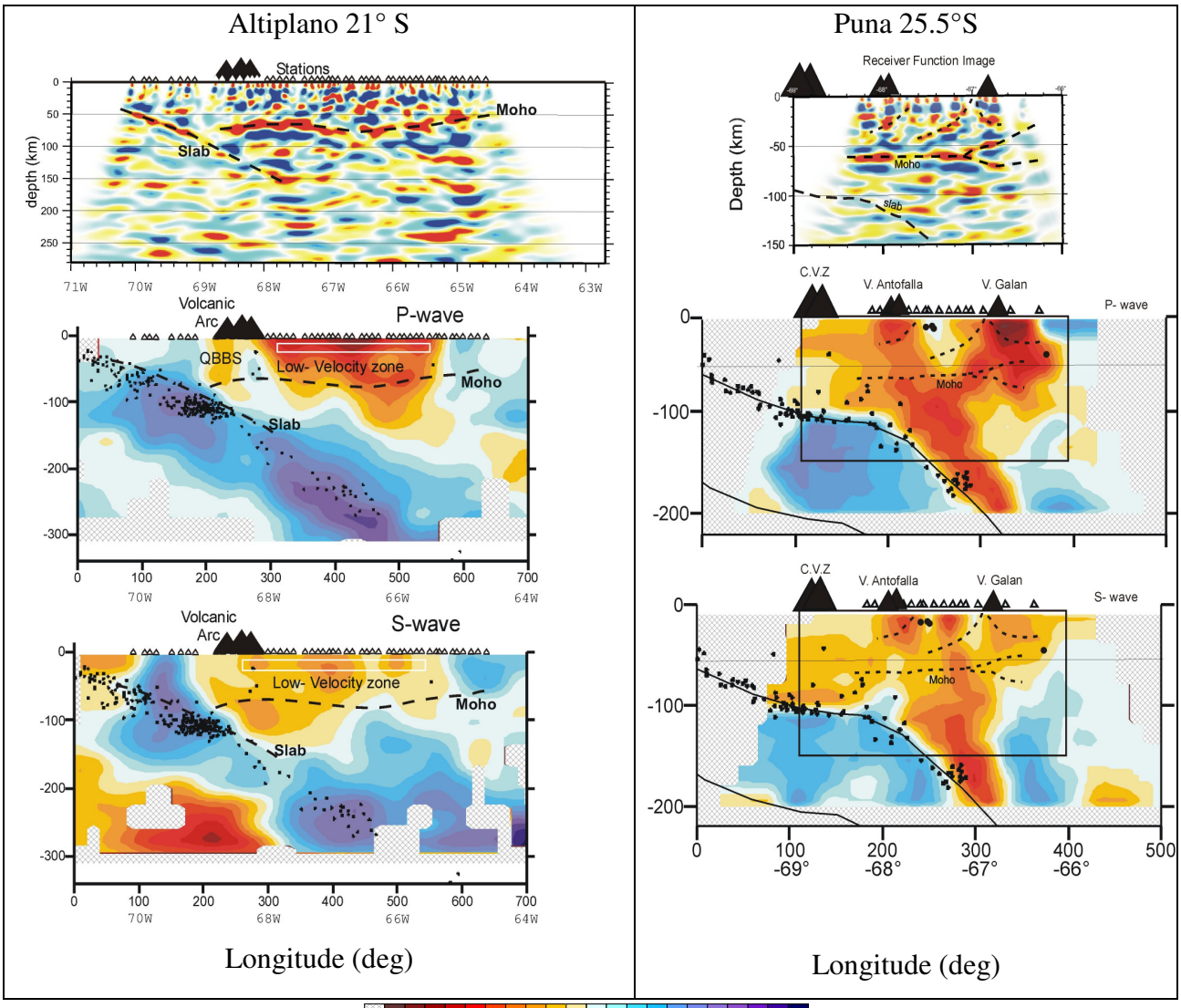

Figure 6.6: Top: Results from receiver function (RF) data, indicating the Moho and oceanic slab discontinuities for both Altiplano and Puna. Centre and bottom: P- and S- wave teleseismic tomography with information from RF. The white rectangle for Altiplano highlights the position of the low-velocity zone beneath the Altiplano.

By comparing receiver function data from both plateaus (Figure 6.7), particularly information about the Moho topography and depth, it is possible to see that there are small differences between both profiles at 21°S (Altiplano) and 25.5°S (Puna). In the case of Altiplano the Moho beneath the central part of the plateau can be seen at ~65 km depth while for the Puna the depth of the same feature is some ~60 km. Internal structures detected by receiver functions suggest a very similar response for both plateaus along major crustal faults (e.g. MAT).

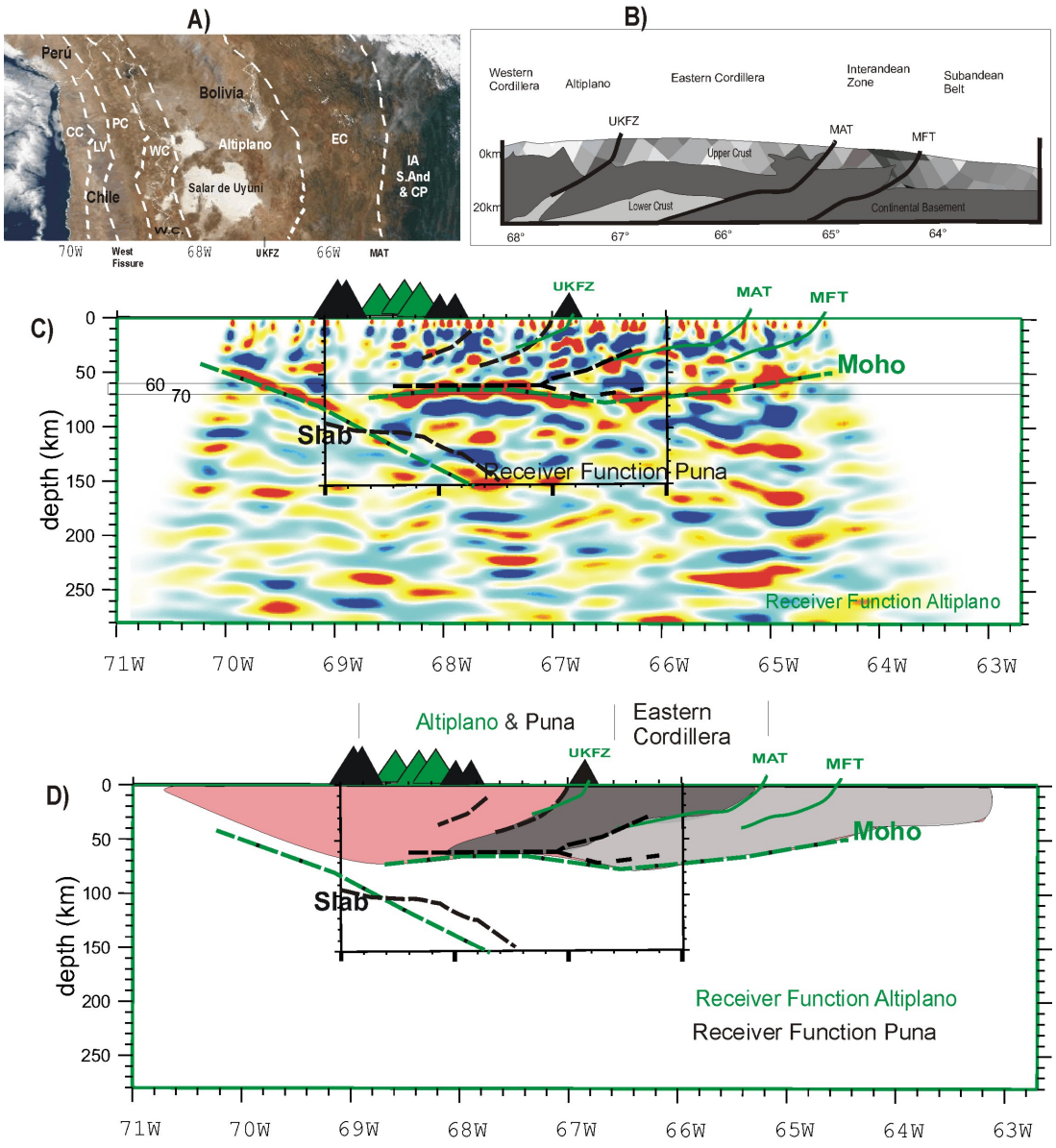

Figure 6.7: A) The Morphological units: CC: Coastal Cordillera; LV: Longitudinal Valley; PC: Precordillera; WC: Western Cordillera; EC: Eastern Cordillera; IA: Interandean; S.And: Subandean; CPlain: Chaco Plain along Altiplano profile at 21°S. UKFZ: Uyuni-Kenayani Fault Zone; MAT: Main Andean Trust. B) The MAT (Main Andean Trust), along the section at 21°S, which affects the entire structure of the upper crust and reaches portions of the lower crust Simplified after Mertmann et al., 2001 and Scheuber et al., submitted. C) Receiver Function Altiplano showing the crustal structures and the Moho (green lines) plotted together with Puna RF data (black lines). D) Diagram integrating RF crustal discontinuities with slab for Altiplano (green line) and Puna data (black line and small rectangle in figure). The different colours (pink and greys) are suggested structural blocks that can be identified and reflect the similarities along both profiles.

The distribution and aspect of the Moho topography shows changes that occur at both latitudes that are probably related with the limits between morphological units on the surface. In Figure

6.7D the position of some crustal discontinuities reflect the similarities between both plateaus, and may be indirectly, the influence such structures had in the geodynamical history of the Central Andes. There is a possible relationship between magmatism in the upper plate and deformation that suggests that, the formation of the Altiplano Plateau was initiated by magmatically-controlled thermal weakening of the crust (Elger, 2003 and Elger et al., 2005). The presence of this thermal effect may indicate that the major deformation structures are related to the low-velocities in the upper-crust detected in our study.

It is not possible to see variations in Moho topography that suggest a variation in lithospheric thicknesses in both cases. From the tomographic images it is possible to see that Puna profile presents a more "hot" material that can be interpreted as astenospheric influx that could affect the thickness of the lithosphere but evidence supporting this idea is still missing. If this is the case, the effect of a thinner lithosphere beneath the Puna can be questioned as our data suggests. In the future, S-wave receiver function analysis of the present data should clarify the position of the LAB as this is the only method that can provide information about the LAB discontinuity.

6.5. Puna and Altiplano: a space problem?

This section discusses the results obtained by the tomographic analysis where it is possible to observe the presence of the Precambrian Brazilian shield on the east of the Altiplano profile. The correlation between the position of the BS and mayor structures limiting this unit should have played a role that influenced the plateau formation and evolution.

Why did a plateau developed in the Central Andes? Why is the history of both the Altiplano and Puna so different in many ways and similar in others? If we compare topographic sections, as noted by other authors in the past years (Whitman et al., 1996; Allmendinger et al., 1997), both Puna and Altiplano differ in the distribution and shape of the basins and in their altitude above sea level (Figure 6.8). The Altiplano presents a more or less regular surface with no major changes in topography inside the plateau. The Puna on the other hand shows a more irregular aspect and displays large topographic variations delimiting the internal closed basins.

One possibility is that plateau growth is a result of the Brazilian craton compressing the weak lower crust under the Altiplano from the east (Beck and Zandt, 2002), while from the west there

is the ENE movement of the Nazca plate. As the Altiplano was compressed, the remaining portions of the plateau in the south (where the Puna is located) were left as a triangle-shaped block that experienced additional uplift, and has been active for a longer time than the northern parts. As discussed before, the uplift in the Altiplano started ~25 Ma and had stopped by ~10-9 Ma, while in the Puna this process continued until ~2Ma.

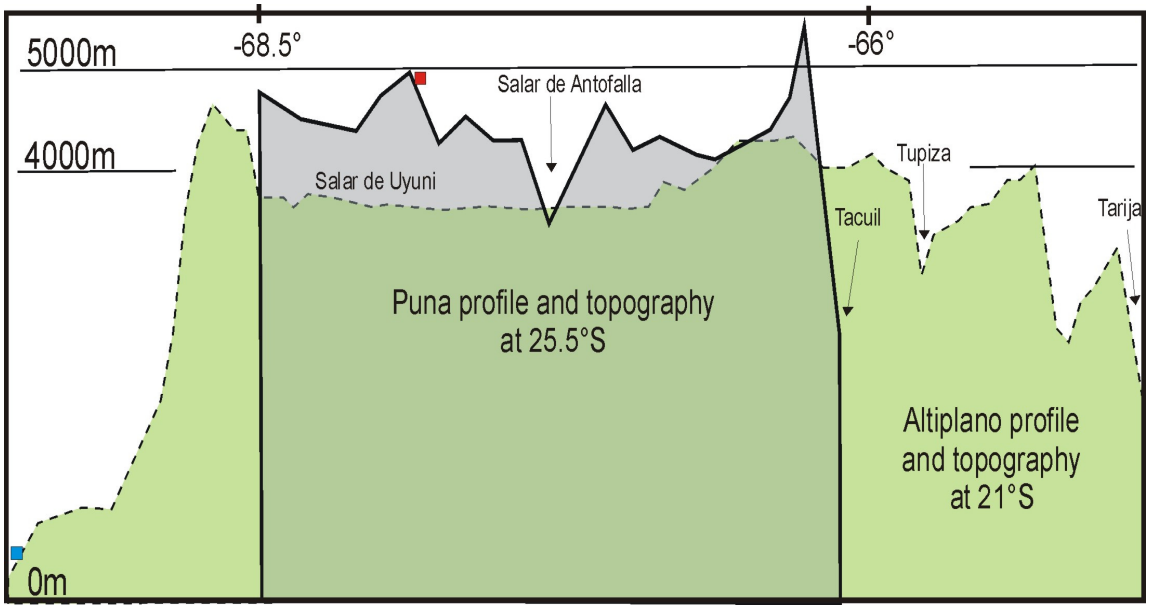

Figure 6.8: On the green background the topography along the profile at 21°S (dashed line). The topography of the Puna profile (grey background and thick bold line) shows the differences in altitude and the irregularities along ~25.5°S. The red square shows the position of the highest station of the project (PC04, ~4800 m). The blue square shows the position of the lowest station (RF01~360 m).

One question that comes out when studying the Andes is related to the different dipping angles of the Nazca oceanic plate during the geodynamical history of the subduction zone and its variation with latitude from the Colombian Andes in the north to the south of Chile. The differences in subduction angles may be associated with thickness variations of the oceanic plate (with a possible direct impact in the confluence rate of the plates) and particularly with buoyant subducting lithosphere (Gutscher, et al., 2000; van Hunen et al., 2002a,b). In this context, the position of the Altiplano-Puna plateau is emplaced in a particular geographic position with respect to other major morphological units in the South American continent, e.g. old, cold Precambrian Brazilian Shield (Figure 6.9). We may therefore, establish a parallel between the existence of flat-slab regions where those fragments of old, cold units are not present or at least have been displaced by the presence of some mayor lineaments (i.e., TBL: Trans-Brazilian Lineament in Cordani and Sato, 1999).

Along with the TBL in the south it is possible to find another major suture or lineament present in the area between the Guyana and Brazilian shields, which is located beneath the Amazonian Basin, where the presence of a proto-rift has been suggested (Burke and Lytwyn, 1993). At the same time, those parts of the Andes that developed large-scale volcanic activity, mountain uplift and a plateau, in the case of Bolivia and northern Argentina, are located in areas where subduction has found opposition, in some way represented by old stable regions such as the BS (Figure 6.9). The presence of the remaining parts of the shield and the lineaments that separate its portions could also be responsible for the differences in morphology between the Altiplano and Puna plateaus.

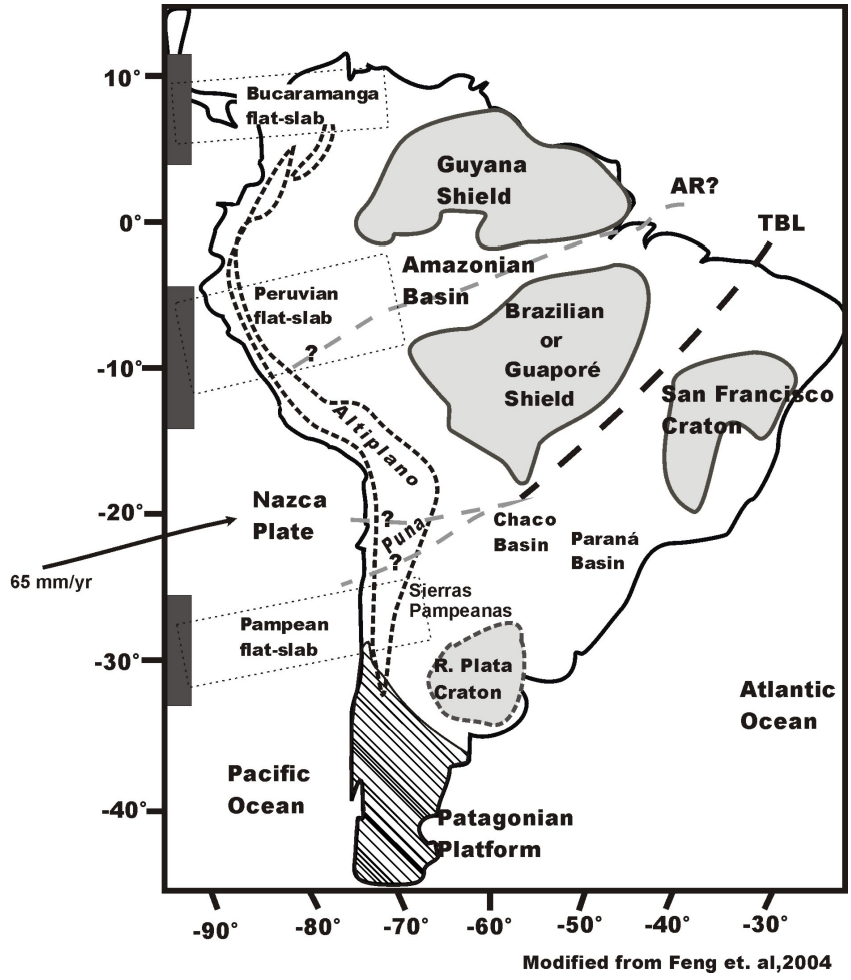

Figure 6.9: Bold Rectangles and related grey dashed rectangles show the correlation between the flat-slab regions and the absence of the exposed Precambrian cratons. Note the position of the Altiplano plateau flanked by units with opposite directions of movement i.e., Nazca Plate (Angermann et al, 1999) and Brazilian Shield (Guaporé). North and south of the BS, large sedimentary basins developed covering continental suture zones. TBL: Trans-Brazilian Lineament (in Cordani and Sato, 1999) could be responsible for structural differences in the plateau (Altiplano and Puna). The grey dashed line at the Amazonian basin is the AR? (Amazonian Rift) as suggested by Burke and Lytwyn (1993). Black dashed area from north to south represent the Andean chain with the position of the plateaus marked

As discussed in Section 6.1.3, shortening and uplift in the Central Andes are responsible for two characteristic features: the thrust belt (Eastern Cordillera) and the thin-skinned fold-thrust belt (Subandean) on the eastern side of the Altiplano plateau. According to Sempere et al. (1997), this compressional regime started around ~90 Ma and has been migrating eastward since then (Jordan et al., 1997; Sempere et al., 1997). This could be related again with to presence of the Brazilian shield.

In addition to the previous statements, we suggest that the presence of the Brazilian Shield is responsible for the change in block rotation (clock- and counter clockwise) (Beck, 1998) from the Arica bending line between 19°S and 23°S, that has been proposed as the symmetry axis of the Central Andes (Gephard, 1994). This is also the trend of the movement of opposite direction on either side of the zone of maximum shortening (Isacks, 1988, Kley and Monaldi, 1998).

An argument that opposes this theory is that the subduction angle of the oceanic plate in the central Andes has changed many times, going from normal to flat and again to normal, while the velocity of convergence and subduction has also changed. Presently, the subduction takes place at a convergence rate of 8.5cm/yr (Angermann, 1999) and the angle, on the basis of seismicity, is ~30° (Engdahl et al., 1995). The subduction angle could therefore have changed due to velocity variations of the subducting plate due to a retarded effect of mineral transformation.

Other authors (e.g. Lamb and Hoke, 1997; Lamb and Davies, 2003) suggest that climatic change during the Cenozoic is responsible for the unusual width and height of the central part of the Altiplano in the Andes and that the onset of hyper aridity along the west coast of South America is responsible for the lack of a thick sediment layer that would otherwise lubricate the interface between the Nazca and South American plates, as is the case in the southern Andes. Erosion, sediment deposition and climate controlled sediment starvation cause high shear stresses in the western part of continental South America where the resulting deformation created a high plateau without collision.

A higher Puna plateau with a more irregular surface could be indicative of less space for shortening and uplift than the Altiplano, probably induced by differences in lithospheric structures or the absence of a thick layer of sediments. This idea is demonstrated by Babeyko and Sobolev (2005) who suggested that different shortening modes for the Central Andes (pure and

simple shear accompanied by thin or thick-skinned tectonics) might be controlled by strength of the foreland uppermost crust and by temperature of the foreland lithosphere. In their model the sediment cover plays a key role in tectonic evolution and support the idea of Allmendinger and Gubbels (1996) that the thick layer of Paleozoic sediments at the Bolivian foreland might be responsible for the simple shear mode of shortening north of 23°S. For the southern Puna at 24°S, the weak sedimentary layer is almost absent and the deformation pattern is described as simple shear with thick-skinned foreland tectonics, similar to the Santa Barbara system east of Puna at ~26°S. A higher temperature of the leading edge of the Brazilian shield south of 24°S than north of 23°S implying a thermal effect for explaining the thick-skinned tectonics in the Puna foreland has been suggested. In our models (for Puna and Altiplano anomalies) we are able to detect changes in relative velocities and therefore interpret that they are related to these temperatures variations. The case of the Puna having a different thermal state than the Altiplano can be then linked to the distribution of deformation that resulted from shortening variations in the crust for both plateaus.

Considering these ideas, it is possible to explain the evolution of the plateau as result of the confluence of many factors that determine the characteristic aspects of the central Andean region, but there is little that we can say about which factors played the larger role.

6.6. Conclusions

The profile of stations at 21°S tomographic analysis confirms previous observations about the presence of a low-velocity layer in the upper crustal portions of the Altiplano (Altiplano Low-Velocity Zone) and shows that this zone may extend towards the Eastern Cordillera where a similar low-velocity body has been detected. A possible relationship between this low-velocity zone and the anomalies observed to the west beneath the volcanic arc can also be interpreted from tomographic results. To the east of the profile, the transition to the Brazilian Shield seems to be abrupt and is governed by the presence of major fault systems, such as the Main Andean Thrust. The tomographic images do not show any evidence supporting underthrusting of the Brazilian lithosphere as suggested by some authors. The presence of a high-velocity block at a depth of ~150km can be associated with the detachment or delamination of lithospheric material. The crustal thickness from receiver function analyses shows a Moho that deepens beneath the volcanic arc probably related to partially melted material accumulated at the base of the

continental crust. In the centre of the profile, beneath the Altiplano plateau, the Moho thins to ~65km and thickens again beneath the Eastern Cordillera. Towards the Chaco Plain in the east, the Moho thins to ~ 40km. It is not possible to observe variations in Moho topography that could suggest variations in lithospheric thicknesses

The Puna profile data indicate the presence of a two-branched pathway for the ascent of fluids and melts. The western part is clearly related to the fluids that reach the volcanic arc (Antofalla volcano) while the other coincides with the presence of back-arc volcanoes along the eastern border of the plateau (e.g. Galan volcano). The tomographic images suggest that the thermal state of the Puna plateau is different from that of the Altiplano, indicating the presence of colder asthenospheric material beneath the Altiplano and hotter beneath Puna. This thermal effect can be interpreted as responsible for the higher elevations of the Puna plateau. Beneath the Salar de Antofalla, a high-velocity block with seismic activity is interpreted as part of the old and cold Paleaozoic magmatic arc (Faja Eruptiva de la Puna occidental). The presence of this block is may be responsible for the distribution of volcanic activity localized at both sides of this anomaly.

Receiver function data provide the best (up to date) images of the Moho topography for both profiles (along 21°S and 25.5°S), indicating that there are no big differences between Altiplano and Puna crustal thicknesses (~65km and ~60km respectively). The internal structures of both plateaus, in terms of the distribution of fault systems and detachment zones in the internal portions of the crust, seem to be more similar than originally thought.

REFERENCES

Achauer, U., A study of the Kenya rift using delay time tomography analysis and gravity modelling, Tectonophysics 209, (1992) 197-207.

Aki, K. and Lee W., Determination of three-dimensional velocity anomalies under a seismic array using first P arrival times from local earthquakes, Part 1. A homogeneous initial model, J. Geophys. Res. 81 (1976) 4381-99.

Aki, K., A. Christofferson, E.S. Husebye, Determination of the three dimensional structure of the lithosphere, J. Geophys. Res., 82 (1977) 277-296.

Aki, K, Seismic Tomography: Theory and Practice. Ed. by H.M. Iyer and K. Hirahara, Chapman and Hall, London, 1993, pp. 842.

Allmendinger, R.W, T. Gubbels, Pure and simple shear plateau uplift, Altiplano-Puna, Argentina and Bolivia, Tectonophysics, 259 (1996)1-13.

Allmendinger, R.W., T.E Jordan, S.M. Kay, B. L. Isacks, The evolution of the Altiplano-Puna Plateau of the central Andes. Annu. Rev. Earth Planet. Sci. 25 (1997) 139-174.

ANCORP Working Group, Seismic reflection image of the Andean Subduction Zone Revealing Offset of Andean subduction-zone earthquake locations into oceanic mantle, Nature 397 (1999) 341-344.

ANCORP Working Group, Seismic imaging of a convergent continental margin and plateau in the Central Andes (Andean Continental Research Project 1996 (ANCORP ´96)), J. Geophys. Res. 108 (2003), 2328, doi:10.1029/2002JB001771.

Angermann, D., J. Klotz, C. Reigber, Space-geodetic estimation of the Nazca-South America Euler vector, Earth Planet. Sci. Lett., 171 (1999) 329-334.

Baby, P., Hérail, G., Salinas, R., Sempere, T., Geometry and kinematics evolution of passive roof duplexes deduced from cross-section balancing: Example from the foreland thrust system of the southern Bolivian Subandean Zone (1992) Tectonics, 11 pp. 523-536

Babeyko, A. and S. Sobolev, Quantifying different modes of the late Cenozoic shortening in the central Andes, Geology, v33 (2005); no. 8; p. 621–624; doi: 10.1130/G21126.

Beck, M E. Jr., On the mechanism of crustal block rotations in the central Andes. Tectonophysics, 299 (1998) 75–92.

Beck, S.L., P.G. Silver, L. Drake, G. Zandt, S.C. Myers, T.C. Wallace, Crustal-thickness variations in the central Andes, Geology 24 (1996) 407-410.

Beck, S., G. Zandt,. The nature of orogenic crust in the central Andes, J. Geophys. Res. 107 (2002) B10 - 2230.

Bijwaard, H., W. Spakman, and E. Engdahl, Closing the gap between regional and global travel time tomography, J. Geophys. Res., 103, 30055-30078, 1998.

Bird, P., Continental delamination and the Colorado Plateau. J. Geophys. Res., 84 (1979) 7561-7571.

Bock, G., B. Schurr, G. Asch, High-resolution receiver function image of the oceanic Moho in the subducting Nazca plate from P-S converted waves, Geophys. Res. Lett. 27 (2000) 3929-3932.

Brasse, H., P. Lezaeta, V. Rath, K. Schwalenberg, W. Soyer, V. Haak,. The Bolivian Altiplano conductivity anomaly, J. Geophys. Res., 107 (2002) doi: 10.1029/2001JB000391.

Burke, K.C. and J.Lytwyn, Origin of the rift under the Amazon Basin as a result of continental collision during Pan-African time, International Geology ReviewVolume 35, Issue 10 (1993), Pages 881-897.

Cahill, T., B. Isacks, Seismicity and Shape of the subducted Nazca plate, J. Geophys. Res., 97(1992) 17,503-17,529.

Chmielowski, J., G. Zandt, C. Haberland, The Central Andean Altiplano-Puna Magma Body, Geophys. Res. Lett., 26 (1999): 783-78.

Class, C. and S. L. Goldstein, Evolution of helium isotopes in the Earth's mantle, Nature 436 (2005), 1107-1112 doi: 10.1038/nature03930.

Coira, B., Davidson, J., Mpodozis, C., Ramos, V., Tectonic and magmatic evolution of the Andes of northern Argentina and Chile, Earth Science Reviews,(1982)18pp.303-332.

Davies, J.H. and Stevenson, D.J., Physical Model of Source Region of Subduction Zone Volcanics, J. Geophys. Res. B, 1992, vol. 97, no. 2, pp. 2037–2070.

DeSilva, S.L., Altiplano-Puna volcanic complex of the central Andes. Geology **17** (1989), pp. 1102–1106.

Dorbath, C., F. Masson, Composition of the crust and upper-mantle in the Central Andes (19.5°S) inferred from P wave velocity and Poisson's ratio: Tectonophysics, 327 (2000) 213-223.

Elger, K., Analysis of deformation and tectonic history of the Southern Altiplano Plateau (Bolivia) and their importance for plateau formation. PhD -Scientific Technical Report, 03/05.GeoForschungsZentrum, Potsdam.

Elger, K., Oncken, O. and Glodny, J. Plateau-style accumulation of deformation: Southern Altiplano, Tectonics, (2005), 24, TC4020.

Engdahl, E. R, . R. D. van der Hilst, J .Berrocal, Imaging of subducted lithosphere beneath Sotuh America, Geophys. Res. Lett. 22 (1995) 2317-2320.

Engdahl, E. R., R. van der Hilst, R. Buland, Global teleseismic earthquake relocation with improved travel times and procedures for depth determination, Bull. Seism. Soc. Am. 88 (1998) 722-743.

Evans, J. and Achauer, U. Teleseismic velocity tomography using the ACH method: theory and application to continental scale studies. In: Iyer, H., Hirahara, K. (Eds.). Seismic tomography: Theory and Practice, Chapman and Hall, London, (1993), pp. 319-360.

Feng, M., M, Assumpcao and Van der Lee, Group-velocity tomography and lithospheric S-velocity structure of the South American continent, Physics of the Earth and Planetary Interiors 147 (2004) 315–331

Francis, P. W.; R. Sparks; C. J. Hawkesworth; R.S. Thorpe; D.M. Pyle; S.R. Tait; M.S. Mantovani; F. McDermott, Petrology and geochemistry of volcanic rocks of the Cerro Galan Caldera, Northwest Argentina, Geological Magazine 126, 5 (1989), pp. 515-547.

Gansser, A., Facts and Theories on the Andes. Journal of the Geological Society (1973), v 129, pp. 93 131.

Gephard, J., Topography and subduction geometry in the central Andes: Clues to the mechanics of a non-collisional orogen, J. Geophys. Res. 99 (1994) 12279-12288.

Giese, P., Scheuber, E., Schilling, F., Schmitz, M. and P. Wigger, Crustal thickening processes in the Central Andes and the different natures of the Moho-discontinuity. Jour. of South American Earth Sci., (1999) 12: 201-220.

Götze, H.-J., B. Lahmeyer, S. Schmidt, S. Strunk, The lithospheric structure of the Central Andes (20-26S) as inferred from quantitative interpretation of regional gravity. In: Tectonics of the Southern Central Andes, in: K.-J. Reutter, E. Scheuber, P.J. Wigger (Eds), Tectonics of the southern Central Andes. Springer-Verlag, New York, (1994), pp. 7-21.

Götze, H.-J., A. Kirchner, The Gravity Field at the Continental Margin of South America (20° to 29° S).Proceedings of the 30th International Geological Congress, in: Ed. Hong Dawei, (4) Utrecht (1997), pp.135-141

Götze, H.-J. and S. Krause, The Central Andean gravity high, a relic of an old subduction complex? Journal of South American Earth Sciences (2002), 14 pp.799-811

Graeber, F. and Asch G., Three-dimensional models of P wave velocity and P-to-S velocity ratio in the southern central Andes by simultaneous inversion of local earthquake data. J. Geophys. Res. 104 (1999) 20237-20256

Gubbels, T., B. Isacks, E. Farrar, High level surfaces, plateau uplift and foreland development, Bolivian central Andes, Geology, 21(1993) 695-698.

Gutscher, M.-A., W. Spakman, H. Bijwaard, and E. Engdahl, Geodynamics of flat subduction: seismicity and tomographic constraints from the Andean margin, Tectonics, 19 (2000) 814–833.

Haberland, C., A. Rietbrock, Attenuation tomography in the western Central Andes: A detailed insight into the structure of a magmatic arc, J. Geophys. Res., 106(2001) 11151-11167.

Haberland, C., A. Rietbrock, B. Schurr, H. Brasse, Coincident anomalies of seimic attenuation and electrical resistivity beneath the southern Bolivian Altiplano plateau, Geophys. Res. Lett., 30 (2003) doi:10.1029/2003GL017492.

Heit, B., Koulakov, I., Asch, G., Yuan, X., Kind, R., Alcozer-R., I., Tawackoli S. and Wilke, H., A teleseismic tomography image of the Southern Central Andes at 21°S. (Submitted to Earth Planet. Sci. Lett., 2005)

Hoke, L., D.R. Hilton, S.H. Lamb, K. Hammerschmidt, H. Friedrichsen, 3He evidence for a wide zone of active mantle melting beneath the Central Andes, Earth Planet. Sci. Lett., 128 (1994) 341-355.

Housemann, G.A., D.P. McKenzie, P. Molnar, Convective instability of a thickened boundary layer and its relevance for the thermal evolution of continental convergence belts, J. Geophys. Res., 142 (1981) 6115–6132.

Husen, S., E. Kissling, E. Flueh, G. Asch, Accurate hypocenter determination in the seismogenic zone of the subducting Nazca Plate in Northern Chile using a combined on-/offshore Network, Geophys. J. Int.,138 (1999) 687-701

Husson, L., Ricard, Y.,: Stress balance above subduction zones - application to the Andes; Earth Planet Sc. Lett., 222 (2004), 1037-1050.

Isacks, B., Uplift of the Central Andean plateau and bending of the Bolivian orocline. J. Geophys. Res. 93 (1988) 3211-3231.

Jordan, T.E., B. Isacks, V.A. Ramos, R.W. Allmendinger, Mountain building in the Central Andes, Episodes 3, (1983) 20-26.

Kay, R. W., S. M. Kay, Delamination and delamination magmatism, Tectonophysics, 219 (1993) 177-189.

Kay, S.M., R.W. Kay, Aleutian magmas in space and time, in: Plafker, G., and Berg, H.C., (Eds), The Geology of Alaska, Geology of North America, G-1, Geological Society of America, 1994, pp. 687-722.

Kay, S.M. and J.M. Abbruzzi, Magmatic evidence for Neogene lithospheric evolution of the Central Andean “flat-slab” between 30°S and 32°S, Tectonophysics (1996) 259, 15-28.

Kay, S.M., C. Mpodozis, B. Coira, Neogene magmatism, tectonism, and mineral deposits of the Central Andes (22ES to 33ES). In B. Skinner et al. (Eds.), Geology and Mineral Deposits of the Central Andes, Society of Economic Geology, Special Publication, 1999, vol. 7, pp. 27-59.

Kennett, B. L., E. R. Engdahl, R. Buland, Constraints on seismic velocities in the Earth from travel times, Geophys. J. Int., 122 (1995) 403-416.

Kley, J. and Reinhardt, M., Geothermal and Tectonic Evolution of the Eastern Cordillera and the Subandean Ranges of Southern Bolivia. - In: Reutter, Scheuber, Wigger (eds.): Tectonics of the Southern Central Andes: 155-170 (1994); Springer Verlag, Berlin.

Kley, J., C. Monaldi, Tectonic shortening and crustal thickness in the Central Andes: How good is correlation?, Geology, 26, (1998), 723-726.

Kley, J., C. R. Monaldi, Tectonic inversion of the Santa Barbara System of the central Andean foreland thrust belt, northwestern Argentina, Tectonics, 21(6) (2002), doi: 10.1029/2002TC902003, 2002.

Koulakov, I. Yu., S.A. Tychkov, S.I. Keselman, Three-dimensional structure of lateral heterogeneities in P-velocities in the upper mantle of the southern margin of Siberia and its preliminary geodynamical interpretation, Tectonophysics, 241, 1(1995) 239-257.

Koulakov, I. Yu., 3D tomographic structure of the upper mantle beneath the central part of Eurasian continent, Geophys. Journ. Int., 133 (1998) 467-489.

Koulakov,I. Yu., S. Tychkov, N. Bushenkova, A. Vasilevskiy, Structure and dynamics of the upper mantle beneath the Alpine-Himalayan orogenic belt, from teleseismic tomography. Tectonophysics. , 358 (2002) 77-96.

Kraemer, B., Adelmann, D., Alten, M., Schnurr, W., Erpenstein, K., Kiefer, E., van den Bogaard, P. and Görler, K. Incorporation of the Paleogene foreland into the Argentina Puna plateau: The Salar de Antofalla area, Southern Central Andes - Journal of South American Earth Sciences 12/2 (1999) 157-182.

Lee, W. and V. Pereyra, Mathematical introduction to seismic tomography. In: Seismic Tomography: Theory and Practice. Ed. by H.M. Iyer and K. Hirahara, Chapman and Hall, London, 1993, pp. 842.

Lamb, S. L., Hoke, L. Kennan, J. Dewey, Cenozoic evolution of the Central Andes in Bolivia and northern Chile, in: J. P. Burg, M. Ford (Eds) Orogeny through time. Geological Society of London, Special Publication, London, vol. 121, 1997, pp. 237-246.

Lamb, S., L. Hoke, Origin of the high plateau in the central Andes, Bolivia, South America, Tectonics 16 (1997) 623-649.

Lamb, S. and P. Davis, Cenozoic climate change as a possible cause for the rise of the Andes, Nature, Vol. 425, (2003) 792-797.

Lüth, S., Ergebnisse weitwinckelseismischer Untersuchungen und die Struktur der Kruste auf einer Traverse über die Zentralen Anden bei 21 Grad S, Berliner Geowissentschaftliche Abhandlungen, (2000) 37, Reihe B.

Martin, S., A. Rietbrock, C. Haberland, G.Asch, Guided waves propagating in subducted oceanic crust, J. Geophys. Res., 108 (2003) doi:10.1029/2003JB002450.

Mertmann, D., E. Scheuber, H. Ege, P. Silva, K-J. Reutter,E. Sobel, V. Jacobshagen, Tectono-sedimentary evolution of the southern Altiplano: basin evolution, thermochronology and structural geology, in: Interaction between endogenic and exogenic processes during subduction orogenesis. SFB-267.Deformation Processes in the Andes, Research period 1999-2001 (2001) 25-50.

Müller, R. D., Roest, W. R., Royer, J.-Y., Gahagan, L. M., and Sclater, J. G., Digital isochrons of the World's ocean floor, Journal of Geophysical Reasearch, 102.(1997) B2, p. 3211-3214.

Myers, S., S. Beck., G. Zandt, T. Wallace, Lithospheric-scale structure across the Central Andes of Bolivia from seismic velocity and attenuation tomography, J. Geophys. Res. 103 (1998) 21233-21252.

Pardo-Casas, F., P. Molnar, Relative motion of the Nazca (Farallon) and South American Plates since Late Cretaceous time. Tectonics, 6 (1987) 233-248.

Patzig, R., Lokalbeben-Tomographie der Umgebung von Antofagasta (Nordchile) sowie Betrachtung der Magnituden-Häufigkeits-Parameter in dieser Region, Diss. Fu-Berlin. Berliner Geowissentschaftliche Abhandlungen, 36 (2000) Reihe B.

Pilger, R. H., Plate reconstruction, aseismic ridges, and low-angle subduction beneath the Andes, Bull. Geol. Soc. Am. 92 (1981) 448-456.

Pilger, R.H., Kinematics of the South American subduction zone from global plate reconstructions. Geodynamics of the Eastern Pacific Region, Caribbean and Scotia Arcs, American Geophysical Union, Geodyn. Ser. 9, (1983) 113-126.

Polet, J., P. Silver, G. Zandt, S. Ruppert, G. Bock, R. Kind, A. Reudloff, G. Asch, S. Beck, and T. Wallace, Shear wave anisotropy beneath the Andes from the BANJO, SEDA, and PISCO experiments, J. Geophys. Res., 105, 6287–6304, 2000.

Poli S and M.W. Schmidt, H2O transport and release in subduction zones—experimental constraints on basaltic and andesitic systems. J. Geophys. Res.(1995) 100:22299–314

Ramos, V., Plate tectonic setting of the Andean Cordillera, Episodes (1999), v.22, No.3, pp. 183-190.

Reutter, K.-J., Giese, P., Götze, H.-J., Scheuber, E., Schwab, K., Schwarz, G. and Wigger, P. (1988): Structures and crustal development of the Central Andes between 210 and 250 S. In: The Southern Central Andes. Bahlburg, H., Breitkreuz, Ch. And Giese, P., (eds.), Lecture Notes in Earth Sciences, 17: 231-261, Berlin.

Riller, U., Petrinovic, L, Ramelow, 1, Greskowiak, L, Strecker, M., and Oncken, 0. (2001): Late Cenozoic tectonism, caldera and plateau formation in the central Andes.. - Earth and Planetary Science Letters, 188: 299-311;

Riller, U., & Oncken, O. (2002): Growth of the central Andean Plateau by tectonic segmentation is controlled by the gradient in crustal shortening.. - Journ. of Geology, Vol. 111: 367-384.

Romanyuk, T. and Yu. L. Rebetsky (2000) Izvestiya, Physics of the Solid Earth, Vol. 37, No. 2, 2001, pp. 107–119. Translated from Fizika Zemli, No. 2, 2001, pp. 23–35. Original Russian Text by Romanyuk, Rebetsky.

Scanlan, P. M. and P. Turner, Structural constraints on palaeomagnetic rotations south of the Arica Bend, northern Chile: implications for the Bolivian Orocline Tectonophysics, Volume 205, Issues1-3 (1992)141-154.

Sempere, T., R. F. Butler, D.R. Richards, L.G. Marshall, W. Sharp, C. Swisher, Stratigraphy and chronology of Upper Cretaceous-lower Paleogene strata in Bolivia and northwest Argentina. Geol. Soc. Am. Bull. 109 (1997) 709-727.

Scheuber, E., Bogdanic, T., Jensen, A. and Reutter, K.-J., 1994, Tectonic development of the North Chilean Andes in relation to plate convergence and magmatism since the Jurassic: *in* Reutter, K.-J., Scheuber, E. and Wigger, P.J. (eds), Tectonics of the Southern Central Andes, Springer-Verlag, 121–139.

Scheuber, E. and Giese, P., Architecture of the Central Andes - a compilation of geoscientific data along a transect at 21°S. J. S. Am. Earth Sci. **12** (1999), pp. 103–107

Scheuber, E., Mertmann, D., EGE, H., Silva, P., Heubeck C., Reutter K-J.; Jacobshagen, V., Exhumation and basin development related to formation of the central Andean plateau, 21°S, Submitted to Frontiers in Earth Sciences. Editors: O. Oncken, G. Chong, G. Franz, P. Giese, H.J. Götze, V. Ramos, M. Strecker, and P. Wigger.

Schilling, F.R., Partzsch, G.M., Brasse, H., Schwarz, G.,Partial Melting below the Magmatic Arc in the Central Andes deduced from Geoelectromagnetic Field Experiments and Laboratory Data. Physics of the Earth and Planetary Interiors (1997) 103, 17±31.

Schilling, F. R., P. Giese, R. Patzig, H. Brasse, A. Rietbrock, P. Wigger, G. Asch, R. Kind, C. Haberland, Fluid/Rock interactions in the Central Andean subduction zone imaged by geophysical observations, Latein Amerika Kollokium, Ext. Abstract, Stuttgart. (2000)

Schmidt, M.W. and Poli, S., Experimentally based water budgets for dehydrating slabs and consequences for arc magma generation. Earth and Planetary Science Letters 163 (1998) 361–379.

Schmitz, M, A balanced model of the southern Central Andes, Tectonics, (1994) 13(2), 484–492.

Schmitz, M., K. Lessel, P. Giese, P. Wigger, M. Araneda, J. Bribach, F. Graeber, S. Grunewald, C. Haberland, S. Lüth, P. Röwer, T. Ryberg, A. Schulze, The crustal structure beneath the Central Andean forearc and magmatic arc as derived from seismic studies – the PISCO 94 experiment in northern Chile (21°-23°S), J. S. Am. Earth Sci. 12 (1999) 237-260.

Schurr, B., G. Asch, A. Rietbrock, R. Kind, M. Pardo, B. Heit, T. Monfret, Seismicity and average velocities beneath the argentine Puna Plateau, Geophys. Res. Lett., 26 (1999) 3025-3028.

Schurr, B., Seismic structure of the central Andean subduction zone from local earthquake data. Ph.D Thesis, Freie Universitaet Berlin, 2000.

Schurr, B., G. Asch, A. Rietbrock, R. Trumbull, C. Haberland,. Complex patterns of fluid and melt transport in the central Andean subduction zone revealed by attenuation tomography. Earth Planet. Sci. Lett. 215 (2003) 105-119.

Schurr, B., A. Rietbrock, Deep seismic structure of the Atacama Basin, northern Chile, Geophys. Res. Lett., 31 (2004) doi:10.1029/2004GL019796.

Schmitt, A.K., Kasemann, S., Meixner, A. and Rhede, D. Boron in central Andean ignimbrites: Implications for crustal boron cycles in an active continental margin. Chemical Geology **183**, (2002) pp. 333–347

Sobolev, S and A. Babeyko, What drives orogeny in the Andes? Geology; v. 33 (2005)8; p. 617–620; doi: 10.1130/G21557.1.

Springer, M. and A. Förster, Heat-flow density across the Central Andean subduction zone. Tectonophysics 291, 1998, 123-139.

Springer, M., Interpretation of heat-flow density in the Central Andes Tectonophysics 306, 1999, 377–395.

Turcotte, D.L. and Schubert, G. Geodynamics: Applications of Continuum Physics to Geological Problems. (1982), New York, John Wiley, 450 p.

Troeng, B., E. Soria, H. Claure, R. Mobarec, F. Murillo, Descubrimiento de basamento precámbrico en la Cordillera Occidental Altiplano de los Andes Bolivianos. Mem. del XI Cong. Geol. Bol., 1994, 231-238.

van Hunen, J., van den Berg, A.P., Vlaar, N.J. The impact of the South-American plate motion and the Nazca Ridge subduction on the flat subduction below south Peru Geophys. Res. Lett., (2002a) p. 29.

van Hunen, J., van den Berg, A.P., Vlaar, N.J On the role of subducting oceanic plateaus in the development of shallow flat subduction (2002b) Tectonophysics, 352 pp. 317-333

Victor, P., O. Oncken, J. Glodny, Uplift of the western Altiplano plateau: Evidence from the Precordillera between 20° and 21°S (northern Chile). Tectonics, 23 (2004) doi:10.1029/2003TC001519.

Walck, M. C., The P-wave upper mantle structure beneath an active spreading centre: The Gulf of California, Geophys. J. R. Astr. Soc., **76**, (1984) 697–723.

Watts, A. B., S.H. Lamb, J.D. Fairhead, J.F. Dewey, Lithospheric flexure and bending of the central Andes, Earth Planet. Sci. Lett. 134 (1995) 9-21.

Whitman, D., B. Isacks, S.M. Kay, Lithospheric structure and along-strike segmentation of the Central Andean Plateau; seismic *Q*, magmatism, flexure, topography and tectonics. Tectonophysics, 259(1996) (1-3): 29-40.

Wigger, P. J., Araneda, M., Giese, P., Heinsohn. W.-D., Röwer, P., Scmitz, M. and Viramonte, J.: The crustal structure along the Central Andean Transect derived from seismic refraction investigations. In: Global Geoscience Transect 6, 1991. Eds.: H.-J. Götze & O. Omarini. Copubl. by the ICL and AGU.

Wigger, P., M. Schmitz, M. Araneda, G. Asch, S. Baldzuhn, P. Giese,W.-D. Heinsohn, E. Martinez, E. Ricaldi, P. Röwer, J. Viramonte, Variation of the crustal structure of the southern Central Andes deduced from seismic refraction investigations, in: K.-J. Reutter, E. Scheuber, P.J. Wigger (Eds), Tectonics of the southern Central Andes. Springer-Verlag, New York, 1994, pp. 23-48.

Wittlinger, G., P. Tapponier, G. Poupinet, J. Mei, S. Danian, G. Herquel, F. Masson, Tomographic Evidence for Localized Lithospheric Shear along the Altyn Tagh Fault, Science 282 (1998)74-76

Yuan, X., S.V. Sobolev, R. Kind, O. Oncken, G. Bock, G. Asch, B. Schurr, F. Graeber, A. Rudloff, W. Hanka, K. Wylegalla, R. Tibi, C. Haberland, A. Rietbrok, P. Giese, P. Wigger, P.Röwer, G. Zandt, S. Beck, T. Wallace, M. Pardo, D. Comte, New constraints on subduction and collision processes in the Central Andes from P-to-S converted seismic phases, Nature, 408 (2000) 958-961.

Yuan, X., S.V Sobolev, R. Kind, Moho topography in the Central Andes and its geodynamic implications, Earth Planet. Sci. Lett., 199 (2002) 389-402.

Zandt, G., S.L. Beck, S.R. Ruppert, C.J. Ammons, D. Rock, E. Minaya, T.C. Wallace, P.G. Silver, Anomalous crust of the Bolivian Altiplano, Central Andes: Constraints from broadband regional seismic waveforms, Geophys. Res. Lett., 23 (1996) 1159-1162.

Zandt, G., M. Leidig, J. Chmielowski, D. Beaumont; X. Yuan, Seismic detection and Characterization of the Altiplano-Puna Volcanic Complex, Central Andes, PAGEOPH 160 (2003) 789-807.

Appendix A.1.

Tables1 and 2

Altiplano & Puna
Station information

Appendix A.1.

Table 1 – Altiplano Chile-Bolivia Stations Information

Name	Instrument Type	Seismometer Type	Latitude (°)	Longitude (°)	Elevation (m)
RF01	REF/7224	L4-3D/1359a	-21.17283	-70.08462	360
RF02	REF/7689	L4-3D/1330	-21.19267	-69.99057	786
RF03	REF/7687	L4-3D/1356a	-21.22222	-69.90070	840
RF04	REF/7681	L4-3D/1353	-21.18321	-69.80809	881
RF05	REF/7233	40T/T4283	-21.11898	-69.72015	968
RF06	REF/7686	L4-3D/1336	-21.09046	-69.61042	907
RF07	REF/7682	L4-3D/1347a	-21.06195	-69.48387	921
RF08	REF/7685	L4-3D/1348a	-21.03160	-69.36105	1154
RF09	REF/7678	L4-3D/1329	-20.98847	-69.23636	1569
RF10	REF/7204	40T/T4282	-20.93445	-69.13488	1925
RF11	REF/7677	L4-3D/1894	-20.93380	-69.01234	2552
RF12	REF/7693	L4-3D/1332	-20.89591	-68.82790	4317
RF13	REF/7680	L4-3D/1333	-20.92401	-68.72174	4714
RF14	REF/7688	L4-3D/1831	-20.95188	-68.56058	4400
RF15	REF/7225	40T/T4281	-21.00850	-68.46247	4400
RF16	SAM/0052	3ESP/T3696	-21.00915	-68.35221	3756
RF17	REF/7226	L4-3D/1178	-21.04238	-68.27659	3781
RF18	EDL/3033	L4-3D/1181	-21.05930	-68.20420	3731
RF19	REF/7226	L4-3D/1190	-21.07285	-68.12930	3847
RF20	EDL/3021	L4-3D/1010	-21.07750	-68.05470	3763
RF21	SAM/0036	3ESP/T3714	-21.05948	-67.97059	3729
RF22	REF/7245	L4-3D/1346	-20.97206	-67.85809	3743
RF23	EDL/3057	L4-3D/1351a	-21.05327	-67.76513	3674
RF24	REF/7228	L4-3D/1191	-20.88210	-67.66955	3728
RF25	EDL/3041	L4-3D/1346a	-20.91234	-67.56601	3690
RF26	EDL/3027	L4-3D/1173	-20.88650	-67.48610	3696
RF27	REF/7206	L4-3D/1012	-20.87315	-67.39110	3731
RF28	SAM/0046	3ESP/T3635	-20.82134	-67.29743	3710
RF29	REF/7209	L4-3D/1176	-20.85613	-67.22707	3700
RF30	EDL/3024	L4-3D/1016	-20.90250	-67.12390	3705
RF31	REF/7237	L4-3D/1192	-20.94274	-67.05694	3734
RF32	EDL/3069	L4-3D/1357a	-20.88470	-66.95910	3691
RF33	REF/7203	L4-3D/1168	-20.92544	-66.89500	3721
RF34	SAM/0049	3ESP/T3709	-20.99935	-66.82792	3705
RF35	EDL/3029	L4-3D/1174	-21.13612	-66.74168	3898
RF36	REF/7231	L4-3D/1340a	-21.16290	-66.63643	3924
RF37	SAM/0038	3ESP/T3735	-21.21918	-66.55107	4017
RF38	EDL/3068	L4-3D/1353a	-21.27210	-66.47090	4265
RF39	REF/7230	L4-3D/1134a	-21.24543	-66.38894	4302
RF40	EDL/3032	L4-3D/1180	-21.39621	-66.29284	4273
RF41	REF/7246	L4-3D/1338	-21.43848	-66.21472	4369
RF42	EDL/3072	L4-3D/1818	-21.42390	-66.15370	4061
RF43	SAM/0052	3ESP/T3696	-21.40724	-66.10284	4024
RF44	EDL/3041	L4-3D/1346a	-21.46727	-66.05178	4027
RF45	REF/7203	L4-3D/1020	-21.43244	-65.98230	3962
RF46	EDL/3025	L4-3D/1018	-21.43510	-65.90440	4141

Name	Instrument Type	Seismometer Type	Latitude (°)	Longitude (°)	Elevation (m)
RF47	REF/7235	L4-3D/1189	-21.45207	-65.82601	3989
RF48	SAM/0057	3ESP/T3695	-21.42440	-65.73810	3003
RF49	EDL/3027	L4-3D/1013	-21.34070	-65.61570	3490
RF50	REF/7244	L4-3D/1332	-21.36676	-65.53179	3681
RF51	SAM/0043	3ESP/T3718	-21.43266	-65.47300	3933
RF52	EDL/3034	L4-3D/1342a	-21.42280	-65.38950	4025
RF53	REF/7211	L4-3D/1182	-21.36119	-65.27616	2635
RF54	EDL/3026	L4-3D/1170	-21.27650	-65.21240	2367
RF55	REF/7214	L4-3D/1245a	-21.29925	-65.12134	2858
RF56	REF/7227	L4-3D/1017	-21.37146	-65.05614	2550
RF57	SAM/0042	3ESP/T3699	-21.42751	-64.97803	3000
RF58	REF/7248	L4-3D/1331	-21.45819	-64.88013	3324
RF59	REF/7215	L4-3D/1187	-21.46413	-64.75682	2008

Table 2 – Argentine Puna Stations Information

Name	Instrument Type	Seismometer Type	Latitude (°)	Longitude (°)	Elevation (m)
PC01	SAM/0050	3ESP/T3689	-25.53569	-68.23110	4339
PC02	EDL/3076	L4-3D/1337a	-25.52340	-68.14692	4209
PC03	SAM/0060	3ESP/T3689	-25.53184	-68.04665	4589
PC04	EDL/3074	L4-3D/1333	-25.46925	-67.96567	4753
PC05	SAM/0086	3ESP/T3713	-25.33550	-67.90624	4123
PC06	EDL/3078	L4-3D/1335	-25.30507	-67.81282	4368
PC07	SAM/0056	3ESP/T3715	-25.33876	-67.73137	4170
PC08	EDL/3079	L4-3D/1339a	-25.43083	-67.64494	4164
PC09	SAM/0059	3ESP/T3693	-25.51648	-67.61888	3400
PC10	EDL/3082	L4-3D/1341	-25.59201	-67.51111	3949
PC11	SAM/0048	3ESP/T3541	-25.58266	-67.40479	4495
PC12	EDL/3080	L4-3D/1340	-25.58238	-67.31203	4072
PC13	SAM/0054	3ESP/T3668	-25.53967	-67.21871	4184
PC14	EDL/3048	L4-3D/1019	-25.46375	-67.16014	4024
PC15	EDL/3077	L4-3D/1343a	-25.51142	-67.03025	3990
PC16	EDL/3073	L4-3D/1349	-25.56353	-66.91698	4104
PC17	EDL/3075	L4-3D/1336	-25.67546	-66.84844	4257
PC18	SAM/0047	3ESP/T3716	-25.74593	-66.75667	4182
PC19	SAM/0039	3ESP/T3697	-25.58170	-66.43080	2425

List of events
Altiplano & Puna
P- and S- waves

Events from PDE (*Preliminary Determination of Epicenters)* catalogue from the
National Earthquake Information Center (NEIC)
http://neic.usgs.gov/neis/epic/

Events used for P-wave tomography Altiplano 21° S

	yymmdd:hhmm ss.ss	Lat. (°)	Lon. (°)	Depth(km)	m*b*	Δ(°)	BAZ (°)
1	020602 0052 10.09	07.60	-37.38	10	5.1	42	47.1
2	020605 1245 17.32	35.47	-36.29	10	5.1	65	27.4
3	020611 0232 31.94	17.61	-94.52	154	5.2	48.5	324
4	020615 1323 08.24	-53.22	23.57	10	5.3	72.2	140.8
5	020616 0246 14.03	08.78	-83.99	35	6.2	35.7	330.3
6	020619 2150 08.30	16.32	-97.94	33	5.2	49.4	319.5
7	020624 0120 36.67	35.85	09.88	10	5.3	93.2	52.4
8	020625 0406 46.10	04.20	-82.49	10	5.1	31	328.8
9	020625 0815 45.41	14.11	-91.25	70	5.1	43.9	324.9
10	020702 1015 59.24	-29.85	-112.39	10	5.5	41	250.5
11	020709 1840 35.63	43.51	-127.16	10	5.5	86.2	320.8
12	020730 0655 07.78	-57.88	-23.24	33	5.8	46.8	149.6
13	020731 0016 44.61	07.92	-82.79	10	6.4	34.4	331.5
14	020731 0445 14.27	07.90	-82.78	10	5.5	34.4	331.5
15	020731 0912 44.73	07.52	-36.31	10	5.2	42.7	48.3
16	020802 1613 19.17	12.13	-86.68	69	5.2	39.9	329.1
17	020803 0239 01.84	08.26	-82.82	10	5.5	34.7	331.7
18	020803 1418 13.45	-01.50	-14.37	10	5.1	55.3	75.1
19	020804 0021 42.88	11.37	-87.31	33	5.1	39.5	327.7
20	020807 2359 14.54	07.85	-82.89	10	5.6	34.4	331.3
21	020823 1816 01.29	-55.50	-26.17	33	5.1	44.3	147.8
22	020827 0648 13.82	-55.70	-25.93	33	5.0	44.5	147.9
23	020831 0527 18.24	02.70	-84.37	23	5.1	30.7	324.2
24	020908 2303 45.29	-01.22	-14.63	10	5.0	55.2	74.6
25	020916 0749 02.34	-55.13	-129.43	10	5.0	55.7	218
26	020921 0212 50.79	18.52	-101.25	60	5.2	53.1	318.1
27	020926 1255 29.78	-19.64	-12.01	10	5.4	51.1	97.2
28	020927 0704 58.10	17.16	-100.59	36	5.5	51.7	317.6
29	020929 1325 01.65	09.05	-84.13	23	5.1	36	330.3
30	021001 0700 58.99	18.81	-63.06	41	5.2	41.7	5.6
31	021003 1608 29.62	23.32	-108.53	10	6.2	61.2	315.9
32	021004 1237 16.35	-57.34	-26.29	150	5.1	45.2	150.1
33	021006 0118 35.80	58.47	-31.81	10	5.4	86.3	17.7
34	021007 2003 54.58	58.31	-31.94	10	5.5	86.1	17.7
35	021011 1441 25.33	15.67	-95.69	33	5.0	47.6	321.2
36	021012 2028 42.59	-59.53	-25.96	33	5.3	46.5	152.5
37	021022 0638 48.17	-43.97	39.01	10	5.0	85.1	135.8
38	021023 0737 30.88	-32.20	-109.51	10	5.1	38.6	246.8
39	021024 0608 37.98	-01.88	29.00	11	6.3	94.8	94.1
40	021105 1405 07.64	19.28	-104.78	10	5.0	55.9	315.7
41	021109 0014 18.08	13.74	-91.18	33	5.6	43.5	324.7
42	021112 0146 48.94	-56.55	-27.53	120	6.0	44.2	149.6
43	021114 1530 29.07	-55.65	-35.63	10	5.0	40	152.7
44	021114 1553 33.81	16.32	-91.15	32	5.0	45.7	326.7
45	021115 1305 36.96	-55.71	-35.78	10	5.5	40	152.8
46	021115 1958 31.78	-56.05	-36.40	10	6.6	40	153.6
47	021116 1016 26.55	-55.77	-35.19	10	5.1	40.3	152.6
48	021121 0253 14.97	12.37	-82.22	7	5.4	38.2	335.5
49	021201 0227 55.18	-35.14	179.98	33	5.7	94.2	229.1
50	021210 0128 33.67	-50.02	-114.12	10	5.7	45.5	221.5

	yymmdd:hhmm ss.ss	Lat. (°)	Lon. (°)	Depth(km)	m*b*	Δ(°)	BAZ (°)
51	021210 1351 26.70	36.19	-07.47	10	5.2	81.4	44.8
52	021215 0556 23.81	10.82	-43.24	10	5.2	40.9	37.2
53	021216 0946 32.18	-26.78	-107.20	10	5.1	36.6	255.6
54	021217 0432 53.07	-56.95	-24.82	10	6.3	45.6	149
55	021218 0147 07.03	-56.99	-25.20	10	5.2	45.5	149.2
56	021218 1412 21.75	-57.09	-24.98	10	6.0	45.6	149.3
57	021219 1417 37.59	-56.87	-24.99	10	5.0	45.5	149
58	030108 1429 10.31	06.03	-77.38	33	5.4	30.6	339.4
59	030109 1543 56.40	-60.01	-58.11	10	5.2	37.5	172.7
60	030110 0208 02.80	16.96	-100.30	29	5.1	51.4	317.7
61	030116 0106 30.63	44.17	-129.26	10	5.1	87.8	320.4
62	030116 0225 05.07	44.28	-129.35	10	5.3	87.9	320.5
63	030116 0503 29.39	44.14	-129.18	10	5.1	87.7	320.4
64	030116 0652 04.44	44.16	-128.93	10	5.2	87.6	320.5
65	030119 0625 51.64	-55.78	-27.05	33	5.0	44	148.5
66	030121 0246 47.74	13.62	-90.77	24	6.3	43.2	325.1
67	030121 0706 53.20	13.56	-90.85	33	5.4	43.2	324.9
68	030122 0206 34.61	18.77	-104.10	24	7.6	55.1	315.8
69	030122 1941 38.51	18.82	-104.37	10	5.6	55.3	315.6
70	030127 1756 25.83	-46.04	35.05	10	6.3	81.7	136.5
71	030131 2012 17.25	10.24	-85.33	27	5.3	37.6	329.5
72	030201 1347 46.82	07.46	-81.81	10	5.1	33.6	332.7
73	030201 1630 57.00	16.55	-92.88	211	5.5	46.8	324.9
74	030201 1847 52.15	57.44	-33.34	10	5.5	85	17.5
75	030207 0634 03.22	-56.28	-26.98	85	5.3	44.3	149.1
76	030208 0849 57.44	-39.78	45.10	10	5.3	91.1	134.4
77	030212 1033 13.19	13.02	-88.78	47	5.2	41.7	327
78	030212 1143 54.09	-37.84	178.84	58	5.6	93.5	226.4
79	030213 0559 10.58	-06.72	-11.80	10	5.1	55.4	82.1
80	030213 0823 47.24	-12.91	-14.54	10	5.1	50.7	88.1
81	030214 1903 21.48	-61.53	-54.03	10	5.0	39.5	170.3
82	030214 2317 52.22	-54.47	05.74	10	5.3	61.6	140.7
83	030218 1601 06.96	-34.42	-112.14	10	5.0	40.9	243.5
84	030220 0548 18.66	-62.46	-160.56	10	5.4	71.5	209.3
85	030302 1307 19.67	-35.08	-178.80	46	5.3	93.3	229.7
86	030302 1642 56.33	-36.95	-20.87	10	5.5	41.9	120.2
87	030303 1954 08.60	-55.23	-27.93	33	5.1	43.3	148.2
88	030312 2341 32.92	26.55	-110.58	10	6.5	64.8	317
89	030317 0410 06.45	-58.20	-11.20	10	5.2	52.9	146.7
90	030321 0109 55.19	18.06	-68.12	97	5.0	40.8	358.4
91	030321 0123 50.87	-57.92	-25.16	33	5.0	46	150.3
92	030327 0744 20.45	18.16	-101.76	33	5.0	53.2	317.4
93	030402 0804 02.54	25.02	-45.43	10	5.0	52.1	25
94	030411 0612 54.58	07.03	-82.35	10	5.6	33.4	331.5
95	030415 0252 15.47	-59.79	-26.21	50	5.1	46.5	152.9
96	030417 0346 42.97	-55.27	-128.91	10	5.0	55.5	217.8
97	030419 1143 51.13	-26.99	-113.15	10	5.0	41.8	254.7
98	030430 0047 08.81	-54.40	05.03	10	5.1	61.2	140.6
99	030507 1310 29.19	50.17	-30.06	10	5.2	79.9	23.1
100	030509 2026 15.98	-48.20	32.27	10	6.1	79.1	137.7
101	030516 0909 24.50	18.29	-101.26	68	5.0	53	317.9
102	030519 0021 36.43	-60.08	-26.90	33	5.5	46.4	153.5

	yymmdd:hhmm ssss	Lat. (°)	Lon. (°)	Depth(km)	m*b*	Δ(°)	BAZ (°)
103	030521 1851 10.30	36.97	03.81	10	5.6	89.4	49.2
104	030522 0314 03.85	37.08	03.63	10	5.4	89.4	49
105	030523 1105 11.92	05.67	-82.65	10	5.4	32.3	329.9
106	030527 1711 28.82	36.93	03.57	8	5.5	89.2	49.1
107	030612 0602 14.37	-22.72	-112.66	10	5.1	41.9	261.1
108	030613 1824 04.05	-04.58	-104.97	10	5.4	41	290.7
109	030621 0555 56.80	10.66	-59.36	10	5.0	34.3	13.4
110	030625 0138 42.17	28.82	-43.61	10	5.5	56.2	24.8
111	030625 0231 03.07	28.66	-43.63	10	5.0	56.1	24.8
112	030702 0511 34.83	22.90	-108.19	10	5.2	60.7	315.9
113	030719 1510 35.67	-41.96	-16.45	10	5.0	45.9	126.7
114	030721 2353 41.51	18.62	-101.03	61	5.0	53.1	318.4
115	030801 0137 13.79	-54.64	01.25	10	5.1	59	141
116	030804 0437 20.13	-60.53	-43.41	10	7.5	41	162.4
117	030804 0536 48.53	-60.57	-42.84	10	5.2	41.1	162.1
118	030804 0634 11.27	-60.54	-44.43	10	5.4	40.7	163.1
119	030804 0638 21.78	-60.64	-43.02	10	5.0	41.2	162.3
120	030804 1253 51.00	-60.51	-42.70	10	5.3	41.1	162
121	030813 0829 27.28	09.35	-79.94	54	5.0	34.6	337.1
122	030814 0841 31.68	-60.54	-43.89	10	5.3	40.8	162.7
123	030825 0628 35.18	14.03	-91.06	100	5.6	43.7	325.1
124	030825 2324 59.13	18.54	-106.69	10	5.3	56.6	313.5
125	030827 1440 42.15	43.74	-28.92	10	5.0	75	27.6
126	030828 0448 19.88	-49.81	-114.81	10	6.1	45.8	222
127	030904 2340 11.81	07.88	-82.20	10	5.3	34.1	332.4
128	030906 0208 13.81	-04.62	-106.04	10	5.8	41.9	289.9
129	030906 1546 59.92	-57.41	-25.63	33	5.3	45.5	149.9
130	030912 0817 37.57	-08.97	-108.77	10	5.1	42.3	282.3
131	030920 1738 34.10	-55.87	-27.90	116	5.5	43.6	149
132	030922 0445 36.24	19.77	-70.67	10	6.6	42.7	354.9
133	030923 1610 22.55	-22.96	-13.65	10	5.1	48.9	101
134	030930 0801 33.11	-60.31	-33.40	10	5.8	44	156.6
135	031005 0905 03.06	-19.93	-11.78	10	5.1	51.2	97.6
136	031009 2213 12.50	57.27	-33.45	10	5.2	84.8	17.5
137	031015 1148 49.33	19.52	-70.86	10	5.0	42.4	354.6
138	031020 1650 18.42	-58.09	-26.24	156	5.5	45.6	151
139	031022 0230 37.20	08.19	-102.94	10	5.2	46.9	307.2
140	031029 1954 19.30	-60.57	-25.29	33	5.4	47.3	153.5
141	031030 0600 45.07	-60.71	-25.15	10	5.5	47.5	153.6
142	031105 0057 24.90	11.19	-86.75	61	5.0	39.1	328.3
143	031109 1348 01.96	-59.51	-25.89	65	5.0	46.5	152.5
144	031112 0454 56.42	28.96	-113.21	10	5.4	68.2	317
145	031122 0229 05.83	19.60	-78.15	10	5.0	43.7	344.7
146	031219 2257 51.35	-03.77	-102.63	10	5.2	39.4	293.7
147	031222 1915 56.00	35.70	-121.10	7	6.4	77.6	317.5
148	031223 0558 37.19	-00.69	-20.33	10	5.3	50.4	70.6
149	031225 0711 11.59	08.41	-82.82	33	6.4	34.8	331.8
150	040101 2331 50.05	17.48	-101.30	29	5.7	52.4	317.2
151	040101 2358 01.55	17.42	-101.31	28	5.8	52.3	317.2
152	040107 1042 38.69	08.38	-82.69	36	5.1	34.8	332
153	040112 1414 30.13	05.61	-79.08	21	5.2	30.8	336
154	040117 2113 09.53	17.74	-95.50	110	5.1	49.1	323

Events used for S-wave tomography Altiplano 21° S

	yymmdd:hhmm ss.ss	Lat. (°)	Lon. (°)	Depth(km)	m*b*	Δ(°)	BAZ (°)
1	020616 0246 14.03	08.78	-83.99	35	6.2	35.7	330.3
2	020731 0016 44.61	07.92	-82.79	10	6.4	34.4	331.5
3	020804 1516 26.99	-35.45	-16.23	10	5.3	45.6	117.7
4	020807 2359 14.54	07.85	-82.89	10	5.6	34.4	331.3
5	021003 1608 29.62	23.32	-108.53	10	6.2	61.2	315.9
6	021109 0014 18.08	13.74	-91.18	33	5.6	43.5	324.7
7	021112 0146 48.94	-56.55	-27.53	120	6.2	44.2	149.6
8	021115 1958 31.78	-56.05	-36.40	10	6.6	40	153.6
9	021210 0128 33.67	-50.02	-114.12	10	5.7	45.5	221.5
10	021217 0432 53.07	-56.95	-24.82	10	6.3	45.6	149
11	021218 1412 21.75	-57.09	-24.98	10	6.0	45.6	149.3
12	030116 0053 15.72	44.28	-129.02	10	6.0	87.7	320.6
13	030121 0246 47.74	13.62	-90.77	24	6.3	43.2	325.1
14	030122 0206 34.61	18.77	-104.10	24	7.6	55.1	315.8
15	030312 2341 32.92	26.55	-110.58	10	6.5	64.8	317
16	030411 0612 54.58	07.03	-82.35	10	5.6	33.4	331.5
17	030417 1450 48.58	-54.62	01.43	10	6.0	59.1	140.9
18	030514 0603 35.86	18.26	-58.63	41	6.5	41.8	12
19	030519 1627 10.20	17.54	-105.47	10	5.8	55.1	313.6
20	030521 1844 20.10	36.96	03.63	12	6.9	89.3	49.1
21	030804 0437 20.13	-60.53	-43.41	10	7.5	41	162.4
22	030828 0448 19.88	-49.81	-114.81	10	6.1	45.8	222
23	030906 0208 13.81	-04.62	-106.04	10	5.8	41.9	289.9
24	030922 0445 36.24	19.77	-70.67	10	6.6	42.7	354.9
25	030930 0801 33.11	-60.31	-33.40	10	5.8	44	156.6
26	031109 1952 36.82	-00.67	-19.68	10	6.0	51	71
27	031221 0740 45.83	-00.76	-20.60	10	5.8	50.2	70.5
28	031222 1915 56.00	35.70	-121.10	7	6.4	77.6	317.5
29	031225 0711 11.59	08.41	-82.82	33	6.4	34.8	331.8
30	040101 2331 50.05	17.48	-101.30	29	5.7	52.4	317.2
31	040116 1807 55.66	07.64	-37.70	10	6.0	41.8	46.7

Events used for P-wave tomography Puna 25.5° S

	yymmdd:hhmm ss.ss	Lat. (°)	Lon. (°)	Depth(km)	m*b*	Δ(°)	BAZ (°)
1	020831 0527 18.24	02.70	-84.37	23	5.7	30.7	324.2
2	020908 2303 45.29	-01.22	-14.63	10	5.3	55.2	74.6
3	020916 0749 02.34	-55.13	-129.43	10	5.0	55.7	218
4	020921 0212 50.79	18.52	-101.25	60	5.0	53.1	318.1
5	020921 0503 21.60	-55.58	-124.96	10	5.0	53.3	216.9
6	020925 1814 48.50	16.87	-100.11	5	5.2	51.2	317.8
7	020926 1255 29.78	-19.64	-12.01	10	5.3	51.1	97.2
8	020927 0704 58.10	17.16	-100.59	36	5.2	51.7	317.6
9	020928 0353 56.68	-53.26	-117.50	10	5.1	48.5	218.2
10	020929 0944 28.22	-33.40	-109.45	10	5.1	38.6	244.9
11	020929 1325 01.65	09.05	-84.13	23	5.1	36	330.3
12	021001 0700 58.99	18.81	-63.06	41	5.3	41.7	5.6
13	021003 1608 29.62	23.32	-108.53	10	5.4	61.2	315.9
14	021004 1237 16.35	-57.34	-26.29	150	5.1	45.2	150.1
15	021006 0118 35.80	58.47	-31.81	10	5.2	86.3	17.7
16	021007 0007 01.23	-59.25	-26.32	33	5.0	46.2	152.3
17	021011 1441 25.33	15.67	-95.69	33	5.2	47.6	321.2
18	021012 1448 36.14	-58.85	-14.19	33	5.0	51.6	148.1
19	021012 2028 42.59	-59.53	-25.96	33	5.3	46.5	152.5
20	021024 0608 37.98	-01.88	29.00	11	5.9	94.8	94.1
21	021028 0238 32.59	-33.90	-178.78	33	5.0	93.9	230.7
22	021103 0149 25.00	51.31	-131.12	10	5.6	92.9	325.6
23	021104 1000 47.15	17.49	-101.43	33	5.2	52.5	317.1
24	021105 1405 07.64	19.28	-104.78	10	5.1	55.9	315.7
25	021108 2320 41.77	16.33	-97.99	25	5.1	49.5	319.4
26	021109 0014 18.08	13.74	-91.18	33	5.4	43.5	324.7
27	021112 0146 48.94	-56.55	-27.53	120	6.0	44.2	149.6
28	021114 1530 29.07	-55.65	-35.63	10	5.1	40	152.7
29	021114 1553 33.81	16.32	-91.15	32	5.1	45.7	326.7
30	021115 1305 36.96	-55.71	-35.78	10	5.8	40	152.8
31	021115 1958 31.78	-56.05	-36.40	10	6.1	40	153.6
32	021116 1016 26.55	-55.77	-35.19	10	5.4	40.3	152.6
33	021117 0924 31.88	-55.66	-35.41	10	5.2	40.1	152.6
34	021120 1819 37.15	12.66	-88.19	51	5.1	41.1	327.5
35	021121 0253 14.97	12.37	-82.22	7	5.4	38.2	335.5
36	021127 1550 04.40	-55.83	-27.40	33	5.0	43.8	148.7
37	021130 0850 55.02	-32.85	-179.26	161	5.1	94.8	231.4
38	021201 0227 55.18	-35.14	179.98	33	5.6	94.2	229.1
39	021207 0824 14.55	-55.71	-35.44	10	5.0	40.1	152.6
40	021210 0309 40.11	17.88	-100.90	85	5.1	52.4	317.9
41	021210 1351 26.70	36.19	-07.47	10	5.0	81.4	44.8
42	021212 0416 02.19	-57.97	-25.18	33	5.0	46	150.4
43	021216 0946 32.18	-26.78	-107.20	10	5.0	36.6	255.6
44	021217 0432 53.07	-56.95	-24.82	10	5.4	45.6	149
45	021218 0147 07.03	-56.99	-25.20	10	5.1	45.5	149.2
46	021218 1412 21.75	-57.09	-24.98	10	5.5	45.6	149.3
47	021219 1417 37.59	-56.87	-24.99	10	5.0	45.5	149
48	021221 1850 54.76	18.35	-62.38	52	5.4	41.3	6.7
49	021226 0819 27.80	-58.23	-139.56	10	5.0	61.6	215
50	030104 1026 23.07	-35.51	179.95	157	5.0	94	228.8
51	030108 1429 10.31	06.03	-77.38	33	5.5	30.6	339.4

	yymmdd:hhmm ss.ss	Lat. (°)	Lon. (°)	Depth(km)	m*b*	Δ(°)	BAZ (°)
52	030109 1543 56.40	-60.01	-58.11	10	5.1	37.5	172.7
53	030110 0129 17.98	-33.24	-178.77	33	5.1	94.3	231.3
54	030110 0208 02.80	16.96	-100.30	29	5.1	51.4	317.7
55	030116 0053 15.72	44.28	-129.02	10	5.4	87.7	320.6
56	030116 0106 30.63	44.17	-129.26	10	5.1	87.8	320.4
57	030116 0225 05.07	44.28	-129.35	10	5.2	87.9	320.5
58	030116 0503 29.39	44.14	-129.18	10	5.1	87.7	320.4
59	030116 0652 04.44	44.16	-128.93	10	5.2	87.6	320.5
60	030118 0210 13.11	-35.84	179.26	114	5.0	94.3	228.2
61	030118 2037 41.37	35.08	-34.93	10	5.2	65.3	28.6
62	030119 0625 51.64	-55.78	-27.05	33	5.0	44	148.5
63	030121 0246 47.74	13.62	-90.77	24	5.5	43.2	325.1
64	030121 0706 53.20	13.56	-90.85	33	5.4	43.2	324.9
65	030122 0206 34.61	18.77	-104.10	24	6.5	55.1	315.8
66	030122 1941 38.51	18.82	-104.37	10	5.6	55.3	315.6
67	030127 1756 25.83	-46.04	35.05	10	5.6	81.7	136.5
68	030131 1832 28.58	10.30	-85.38	25	5.0	37.7	329.5
69	030201 1347 46.82	07.46	-81.81	10	5.1	33.6	332.7
70	030201 1630 57.00	16.55	-92.88	211	5.3	46.8	324.9
71	030201 1847 52.15	57.44	-33.34	10	5.3	85	17.5
72	030205 1901 11.09	13.77	-90.88	56	5.3	43.4	325.1
73	030207 0634 03.22	-56.28	-26.98	85	5.4	44.3	149.1
74	030208 0849 57.44	-39.78	45.10	10	5.5	91.1	134.4
75	030212 1143 54.09	-37.84	178.84	58	5.6	93.5	226.4
76	030213 0559 10.58	-06.72	-11.80	10	5.3	55.4	82.1
77	030213 0823 47.24	-12.91	-14.54	10	5.0	50.7	88.1
78	030214 1903 21.48	-61.53	-54.03	10	5.0	39.5	170.3
79	030214 2317 52.22	-54.47	05.74	10	5.4	61.6	140.7
80	030220 0548 18.66	-62.46	-160.56	10	5.0	71.5	209.3
81	030222 1137 45.91	-46.10	34.67	10	5.1	81.4	136.4
82	030222 1219 10.58	34.31	-116.84	1	5.0	74.1	318.9
83	030302 1307 19.67	-35.08	-178.80	46	5.3	93.3	229.7
84	030302 1642 56.33	-36.95	-20.87	10	5.6	41.9	120.2
85	030302 1758 03.33	-55.25	-28.00	33	5.3	43.2	148.3
86	030303 1954 08.60	-55.23	-27.93	33	5.0	43.3	148.2
87	030307 1223 10.27	00.85	-26.90	10	5.0	45.7	64.2
88	030309 1654 58.03	-33.35	-179.24	33	5.2	94.6	231
89	030312 2341 32.92	26.55	-110.58	10	5.5	64.8	317
90	030314 0255 45.33	-62.09	161.72	10	5.2	86.7	200.7
91	030317 0410 06.45	-58.20	-11.20	10	5.3	52.9	146.7
92	030321 0109 55.19	18.06	-68.12	97	5.1	40.8	358.4
93	030321 0123 50.87	-57.92	-25.16	33	5.0	46	150.3
94	030327 0744 20.45	18.16	-101.76	33	5.0	53.2	317.4
95	030402 0057 27.44	-14.63	-109.39	10	5.0	40.9	274.1
96	030402 0343 11.58	35.28	-35.72	10	5.5	65.1	27.9
97	030402 0804 02.54	25.02	-45.43	10	5.0	52.1	25
98	030411 0612 54.58	07.03	-82.35	10	5.6	33.4	331.5
99	030415 0252 15.47	-59.79	-26.21	50	5.1	46.5	152.9
100	030417 0346 42.97	-55.27	-128.91	10	5.0	55.5	217.8
101	030418 0835 53.66	-55.03	-128.69	10	5.0	55.3	218.1
102	030419 1143 51.13	-26.99	-113.15	10	5.0	41.8	254.7
103	030430 0047 08.81	-54.40	05.03	10	5.1	61.2	140.6
104	030507 1310 29.19	50.17	-30.06	10	5.2	79.9	23.1
105	030509 1424 26.24	-55.86	-27.43	33	5.0	43.8	148.8

	yymmdd:hhmm ss.ss	Lat. (°)	Lon. (°)	Depth(km)	m*b*	Δ(°)	BAZ (°)
106	030509 2026 15.98	-48.20	32.27	10	5.5	79.1	137.7
107	030512 0417 38.48	-56.98	-26.39	70	5.0	44.9	149.7
108	030514 0603 35.86	18.26	-58.63	41	6.5	41.8	12
109	030516 0909 24.50	18.29	-101.26	68	5.0	53	317.9
110	030519 0021 36.43	-60.08	-26.90	33	5.5	46.4	153.5
111	030519 1627 10.20	17.54	-105.47	10	5.6	55.1	313.6
112	030521 1844 20.10	36.96	03.63	12	6.5	89.3	49.1
113	030521 1851 10.30	36.97	03.81	10	5.7	89.4	49.2
114	030523 1105 11.92	05.67	-82.65	10	5.1	32.3	329.9
115	030527 1711 28.82	36.93	03.57	8	5.5	89.2	49.1
116	030604 1628 15.05	08.37	-103.06	10	5.0	47.1	307.3
117	030613 1824 04.05	-04.58	-104.97	10	5.2	41	290.7
118	030619 2058 07.64	-31.26	-178.33	52	5.3	95	233.2
119	030621 0555 56.80	10.66	-59.36	10	5.0	34.3	13.4
120	030702 0511 34.83	22.90	-108.19	10	5.1	60.7	315.9
121	030719 1313 48.27	61.96	-26.74	10	5.0	90.6	17.8
122	030721 2353 41.51	18.62	-101.03	61	5.0	53.1	318.4
123	030801 0137 13.79	-54.64	01.25	10	5.1	59	141
124	030804 0437 20.13	-60.53	-43.41	10	6.2	41	162.4
125	030804 0536 48.53	-60.57	-42.84	10	5.2	41.1	162.1
126	030804 0634 11.27	-60.54	-44.43	10	5.4	40.7	163.1
127	030804 0638 21.78	-60.64	-43.02	10	5.0	41.2	162.3
128	030804 1253 51.00	-60.51	-42.70	10	5.6	41.1	162
129	030811 0117 53.60	18.34	-106.03	10	5.1	56.1	313.9
130	030813 0829 27.28	09.35	-79.94	54	5.0	34.6	337.1
131	030819 0113 28.31	-32.93	-179.20	33	5.2	94.7	231.4
132	030825 0628 35.18	14.03	-91.06	100	5.4	43.7	325.1
133	030825 2324 59.13	18.54	-106.69	10	5.5	56.6	313.5
134	030827 1440 42.15	43.74	-28.92	10	5.1	75	27.6
135	030828 0448 19.88	-49.81	-114.81	10	5.4	45.8	222
136	030829 0941 37.23	-59.28	-24.87	10	5.2	46.8	151.8
137	030904 2340 11.81	07.88	-82.20	10	5.4	34.1	332.4
138	030906 0208 13.81	-04.62	-106.04	10	5.4	41.9	289.9
139	030906 1546 59.92	-57.41	-25.63	33	5.6	45.5	149.9
140	030912 0817 37.57	-08.97	-108.77	10	5.1	42.3	282.3
141	030920 1738 34.10	-55.87	-27.90	116	5.5	43.6	149
142	030922 0445 36.24	19.77	-70.67	10	6.2	42.7	354.9
143	030922 0530 17.80	19.91	-70.50	10	5.1	42.8	355.1
144	030923 1610 22.55	-22.96	-13.65	10	5.1	48.9	101
145	030930 0801 33.11	-60.31	-33.40	10	5.6	44	156.6
146	030930 1408 37.74	-30.43	-177.39	10	5.8	94.7	234.3
147	030930 1522 31.70	-30.49	-177.18	33	5.4	94.5	234.4
148	031005 0905 03.06	-19.93	-11.78	10	5.1	51.2	97.6
149	031015 1148 49.33	19.52	-70.86	10	5.0	42.4	354.6
150	031020 1650 18.42	-58.09	-26.24	156	5.4	45.6	151
151	031022 0230 37.20	08.19	-102.94	10	5.2	46.9	307.2
152	031029 1954 19.30	-60.57	-25.29	33	5.4	47.3	153.5
153	031030 0600 45.07	-60.71	-25.15	10	5.6	47.5	153.6
154	031105 0057 24.90	11.19	-86.75	61	5.0	39.1	328.3
155	031107 1819 07.49	-57.30	-25.01	33	5.0	45.7	149.5
156	031109 1348 01.96	-59.51	-25.89	65	5.0	46.5	152.5
157	031112 0454 56.42	28.96	-113.21	10	5.5	68.2	317
158	031122 0229 05.83	19.60	-78.15	10	5.0	43.7	344.7
159	031210 0942 25.41	-50.03	-114.88	10	5.1	45.9	221.7

	yymmdd:hhmm ss.ss	Lat. (°)	Lon. (°)	Depth(km)	m*b*	Δ(°)	BAZ (°)
160	031214 1437 37.99	-55.44	-01.83	10	5.3	57.3	142.1
161	031217 0421 05.26	-58.30	-139.75	10	5.0	61.7	214.9
162	031219 2257 51.35	-03.77	-102.63	10	5.2	39.4	293.7
163	031222 1915 56.00	35.70	-121.10	7	6.1	77.6	317.5
164	031223 0558 37.19	-00.69	-20.33	10	5.6	50.4	70.6
165	031223 1537 27.02	12.96	-88.28	86	5.1	41.4	327.6
166	031225 0711 11.59	08.41	-82.82	33	6.0	34.8	331.8
167	031225 1421 14.94	-34.95	-178.24	34	5.7	93	230.1
168	040101 2331 50.05	17.48	-101.30	29	5.6	52.4	317.2
169	040101 2358 01.55	17.42	-101.31	28	5.2	52.3	317.2
170	040107 0751 37.32	43.57	-110.38	3	5.0	77.3	329.2
171	040107 1042 38.69	08.38	-82.69	36	5.1	34.8	332
172	040112 1414 30.13	05.61	-79.08	21	5.2	30.8	336
173	040113 1950 19.15	16.06	-96.94	28	5.1	48.6	320.3
174	040113 2128 57.76	16.10	-96.93	28	5.5	48.7	320.3
175	040114 1838 54.18	-19.84	-125.24	10	5.2	54	261.6
176	040116 1807 55.66	07.64	-37.70	10	5.9	41.8	46.7
177	040117 2113 09.53	17.74	-95.50	110	5.1	49.1	323

Events for S-wave tomography Puna 25.5° S

	yymmdd:hhmm ss.ss	Lat. (°)	Lon. (°)	Depth(km)	m*b*	Δ(°)	BAZ (°)
1	021003 1608 29.62	23.32	-108.53	10	6.2	61.2	315.9
2	021109 0014 18.08	13.74	-91.18	33	5.6	43.5	324.7
3	021112 0146 48.94	-56.55	-27.53	120	6.2	44.2	149.6
4	021115 1958 31.78	-56.05	-36.40	10	6.6	40	153.6
5	021210 0128 33.67	-50.02	-114.12	10	5.7	45.5	221.5
6	021217 0432 53.07	-56.95	-24.82	10	6.3	45.6	149
7	021218 1412 21.75	-57.09	-24.98	10	6.0	45.6	149.3
8	030116 0053 15.72	44.28	-129.02	10	6.0	87.7	320.6
9	030121 0246 47.74	13.62	-90.77	24	5.5	43.2	325.1
10	030122 0206 34.61	18.77	-104.10	24	6.5	55.1	315.8
11	030127 1756 25.83	-46.04	35.05	10	5.6	81.7	136.5
12	030312 2341 32.92	26.55	-110.58	10	5.5	64.8	317
13	030411 0612 54.58	07.03	-82.35	10	5.6	33.4	331.5
14	030417 1450 48.58	-54.62	01.43	10	5.5	59.1	140.9
15	030514 0603 35.86	18.26	-58.63	41	6.5	41.8	12
16	030519 1627 10.20	17.54	-105.47	10	5.6	55.1	313.6
17	030521 1844 20.10	36.96	03.63	12	6.5	89.3	49.1
18	030804 0437 20.13	-60.53	-43.41	10	6.2	41	162.4
19	030828 0448 19.88	-49.81	-114.81	10	5.4	45.8	222
20	030906 0208 13.81	-04.62	-106.04	10	5.4	41.9	289.9
21	030922 0445 36.24	19.77	-70.67	10	6.2	42.7	354.9
22	030930 0801 33.11	-60.31	-33.40	10	5.6	44	156.6
23	030930 1408 37.74	-30.43	-177.39	10	5.8	94.7	234.3
24	031109 1952 36.82	-00.67	-19.68	10	5.5	51	71
25	031221 0740 45.83	-00.76	-20.60	10	5.5	50.2	70.5
26	031222 1915 56.00	35.70	-121.10	7	6.1	77.6	317.5
27	031225 0711 11.59	08.41	-82.82	33	6.0	34.8	331.8
28	040101 2331 50.05	17.48	-101.30	29	5.6	52.4	317.2
29	040116 1807 55.66	07.64	-37.70	10	5.9	41.8	46.7

Appendix A.3

Flow Chart

(Green: data base; Red: Inversion algorithm; Blue: final model)

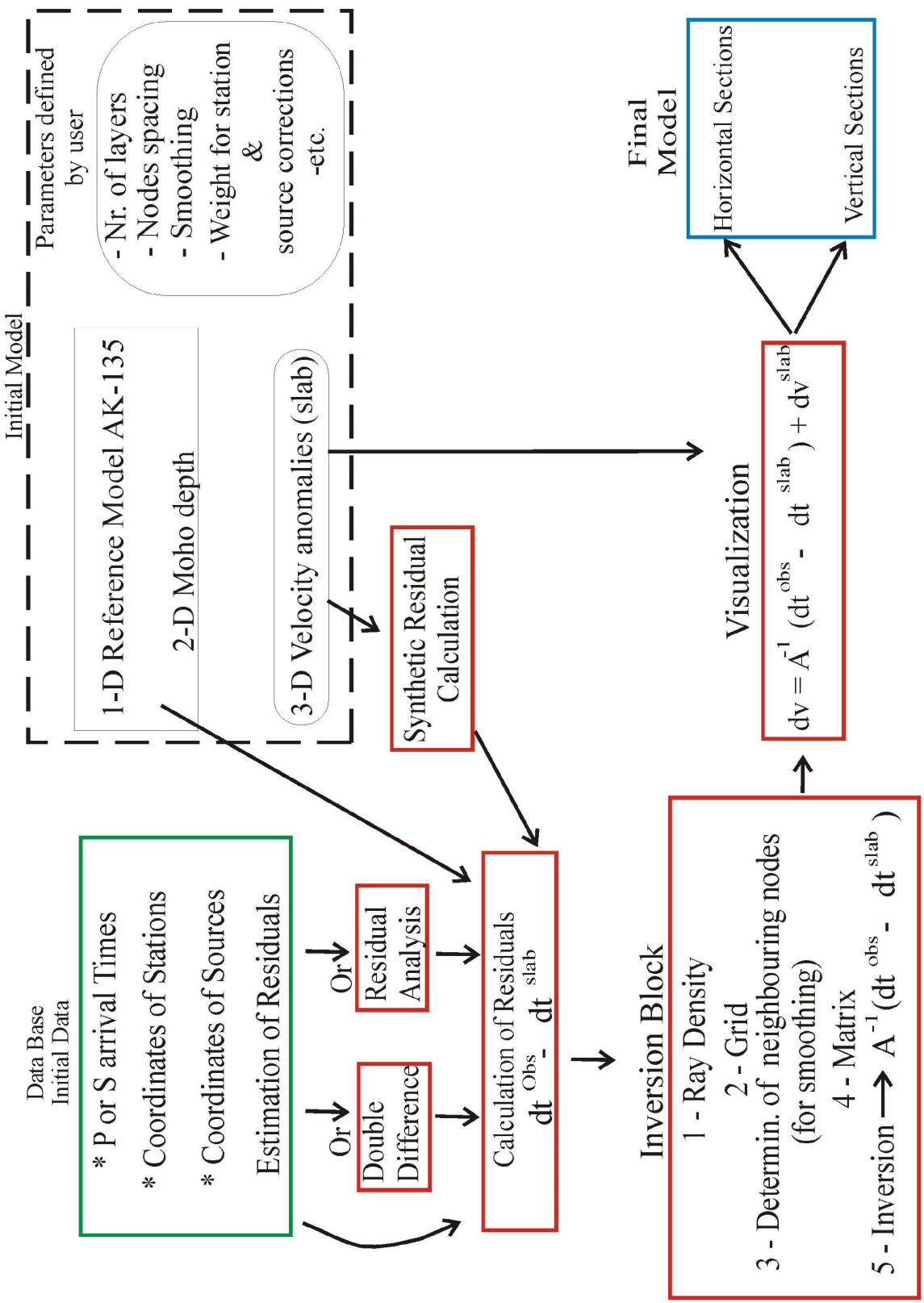

Appendix A.4. Altiplano

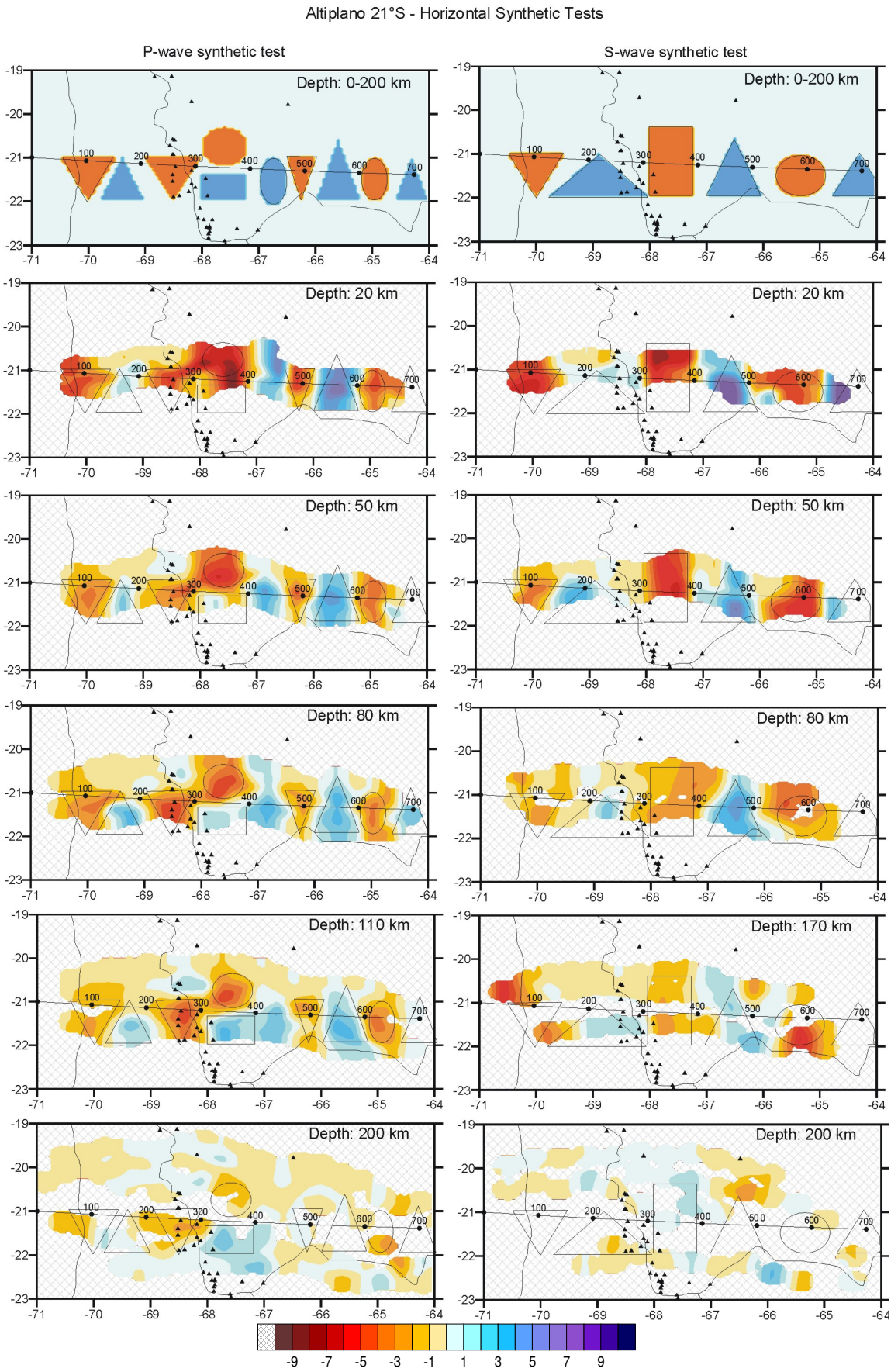

Appendix A.4. Altiplano

Altiplano ~21°S – Vertical tests

P- synthetic tests S- synthetic tests

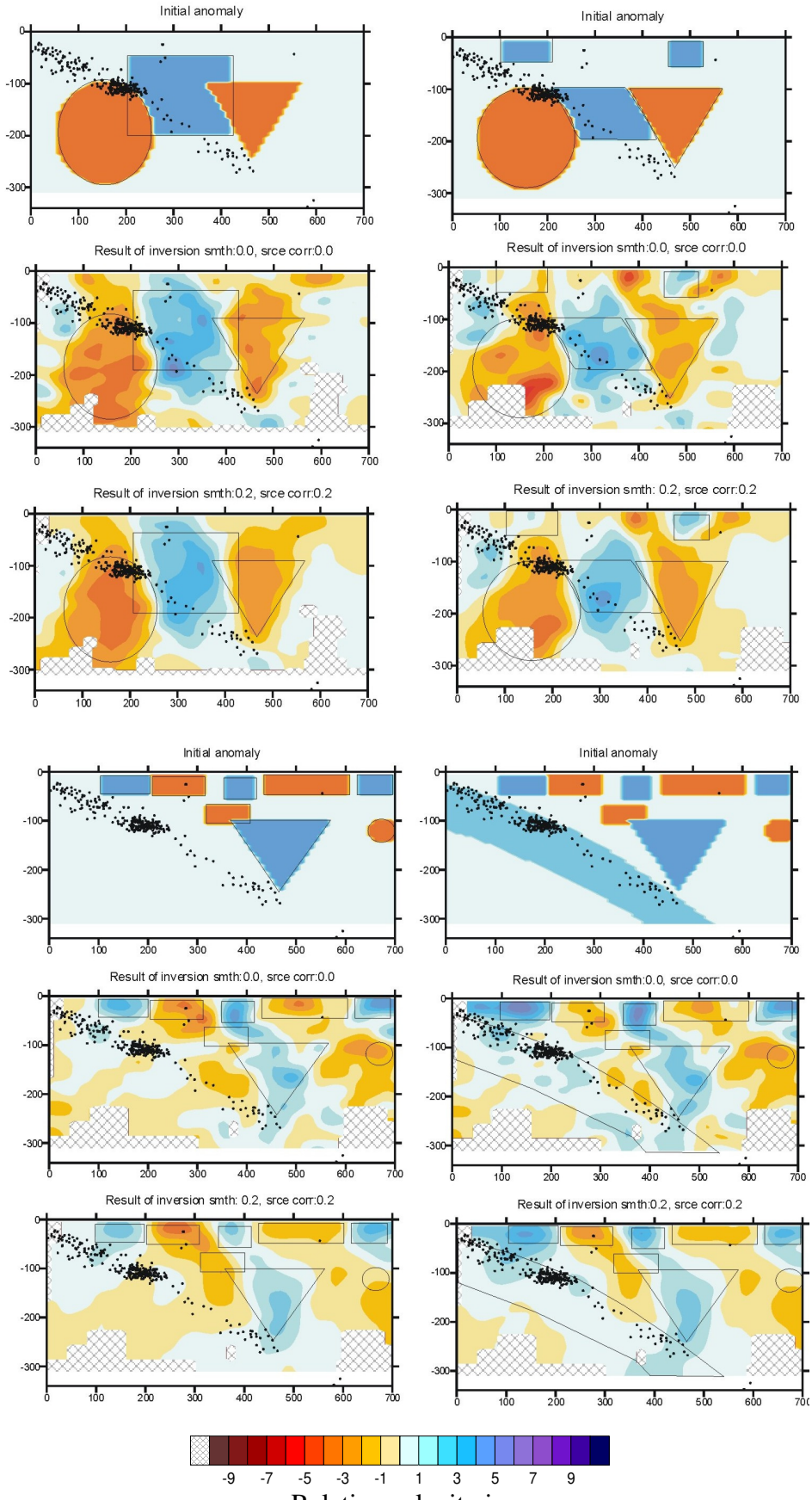

Relative velocity in

Appendix A.4. Puna

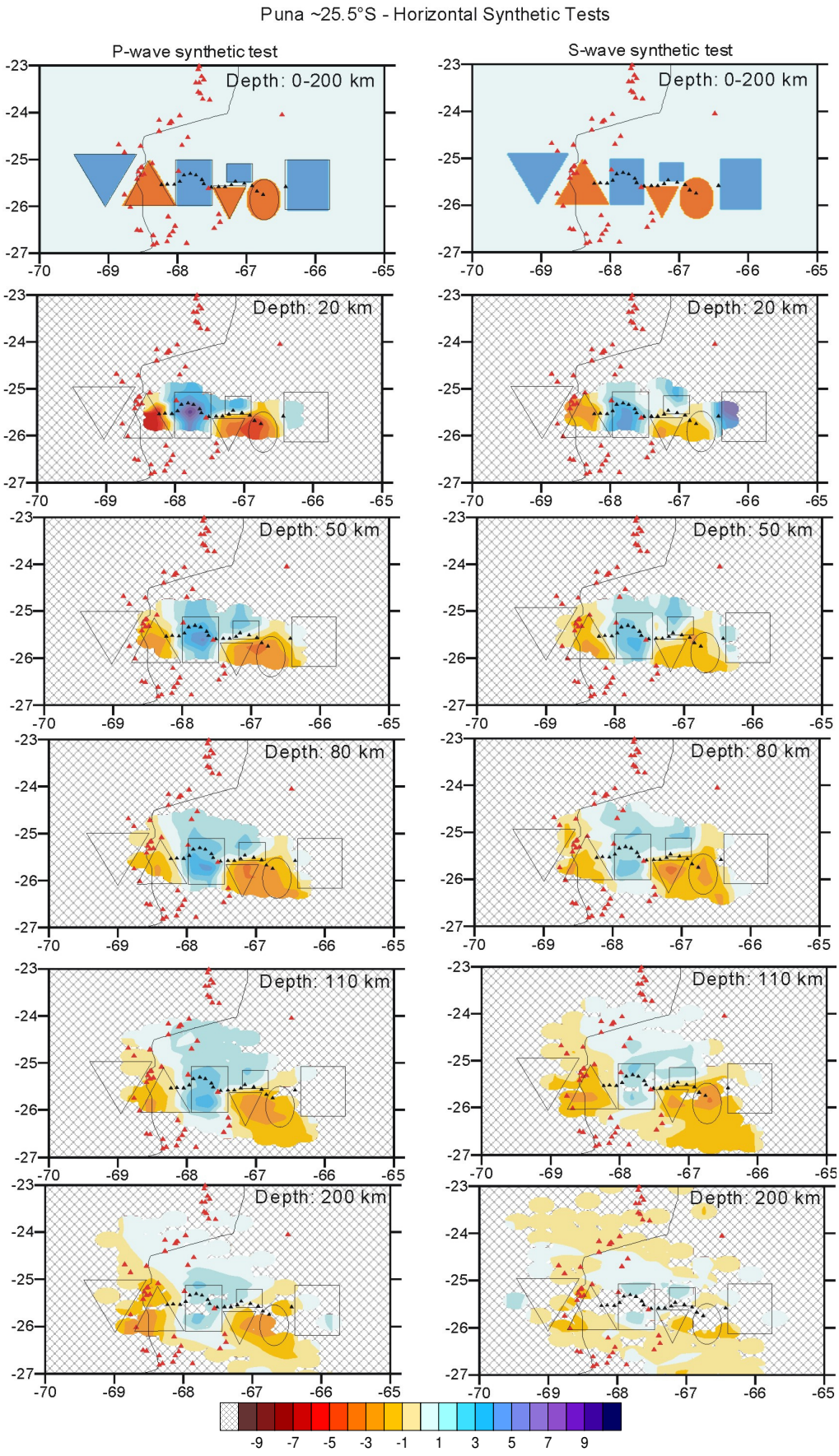

Appendix A.4. Puna

Puna ~25.5°S Vertical tests

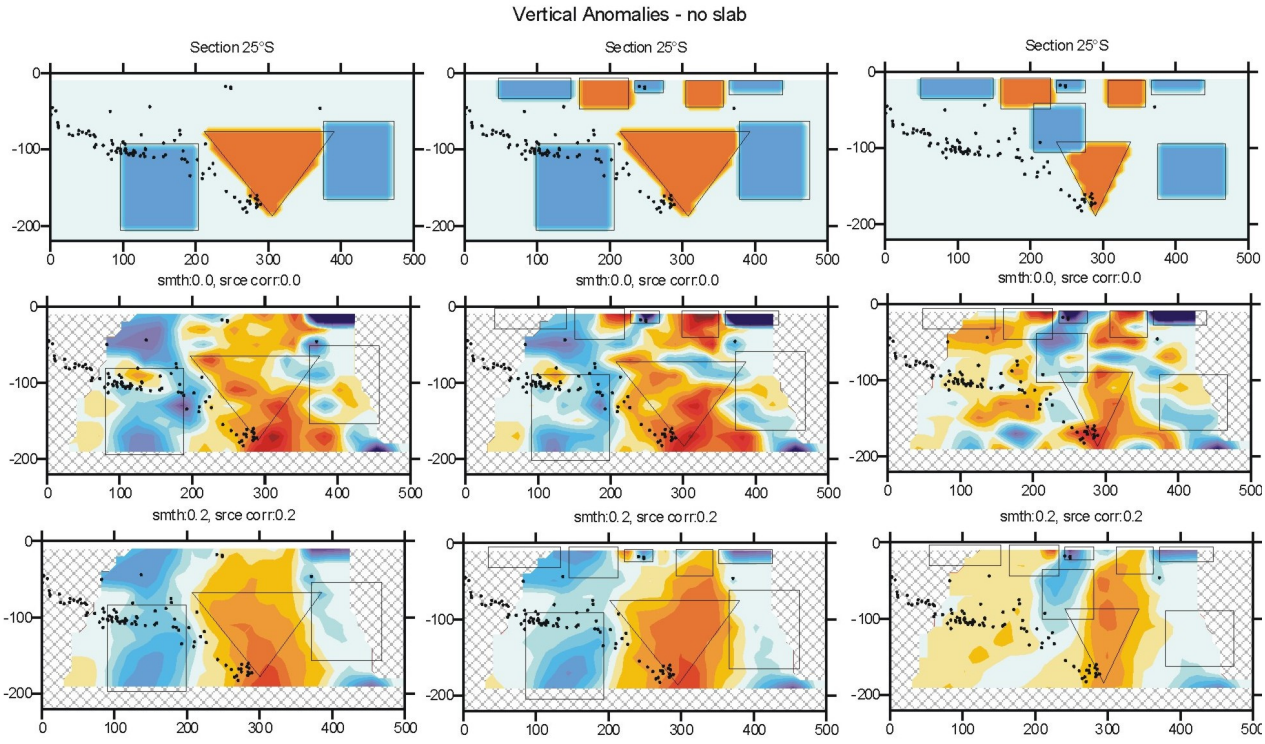

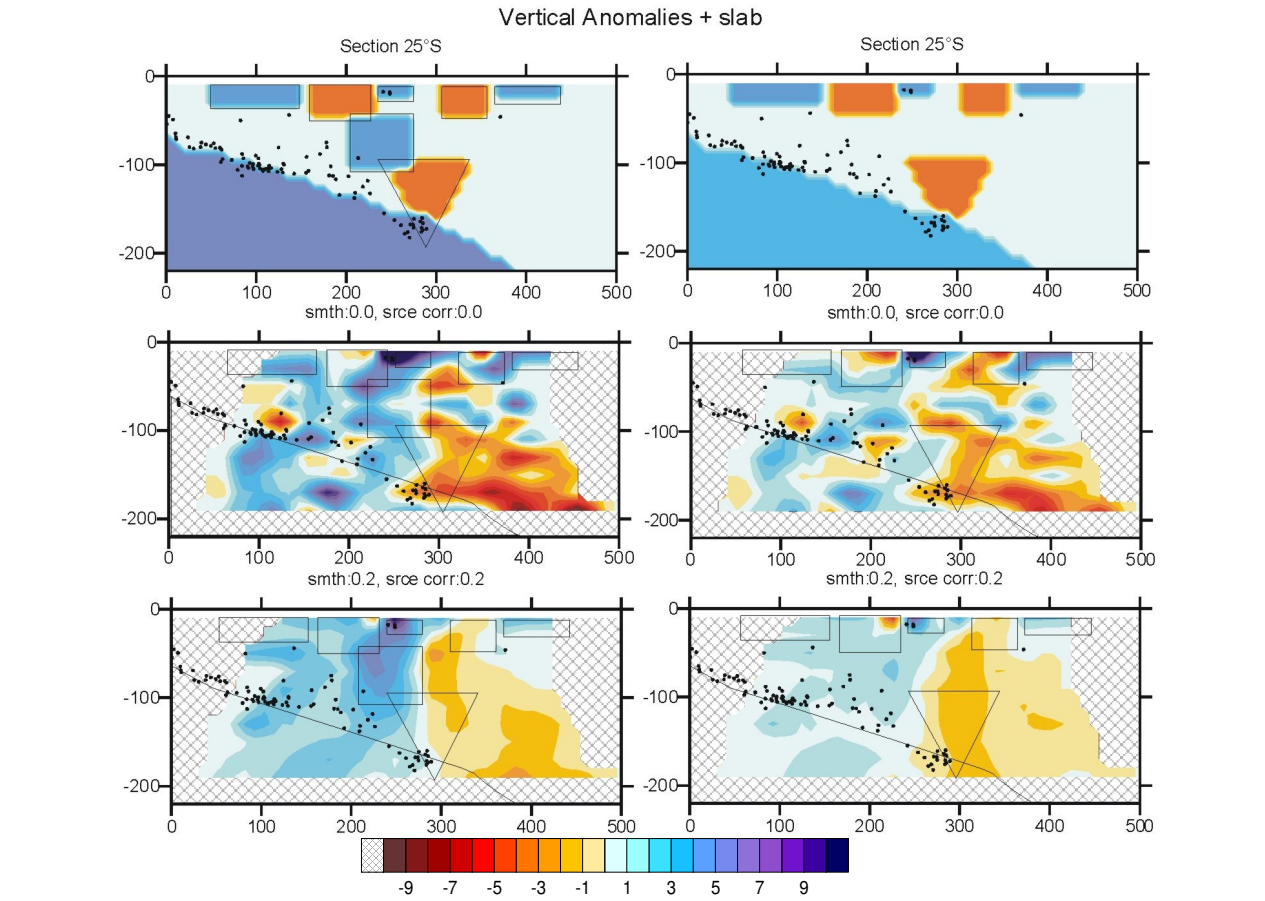

Appendix A.5. Altiplano

Horizontal Sections P- and S- waves Altiplano 21°S
Real data Inversion

P-velocity anomalies

S-velocity anomalies

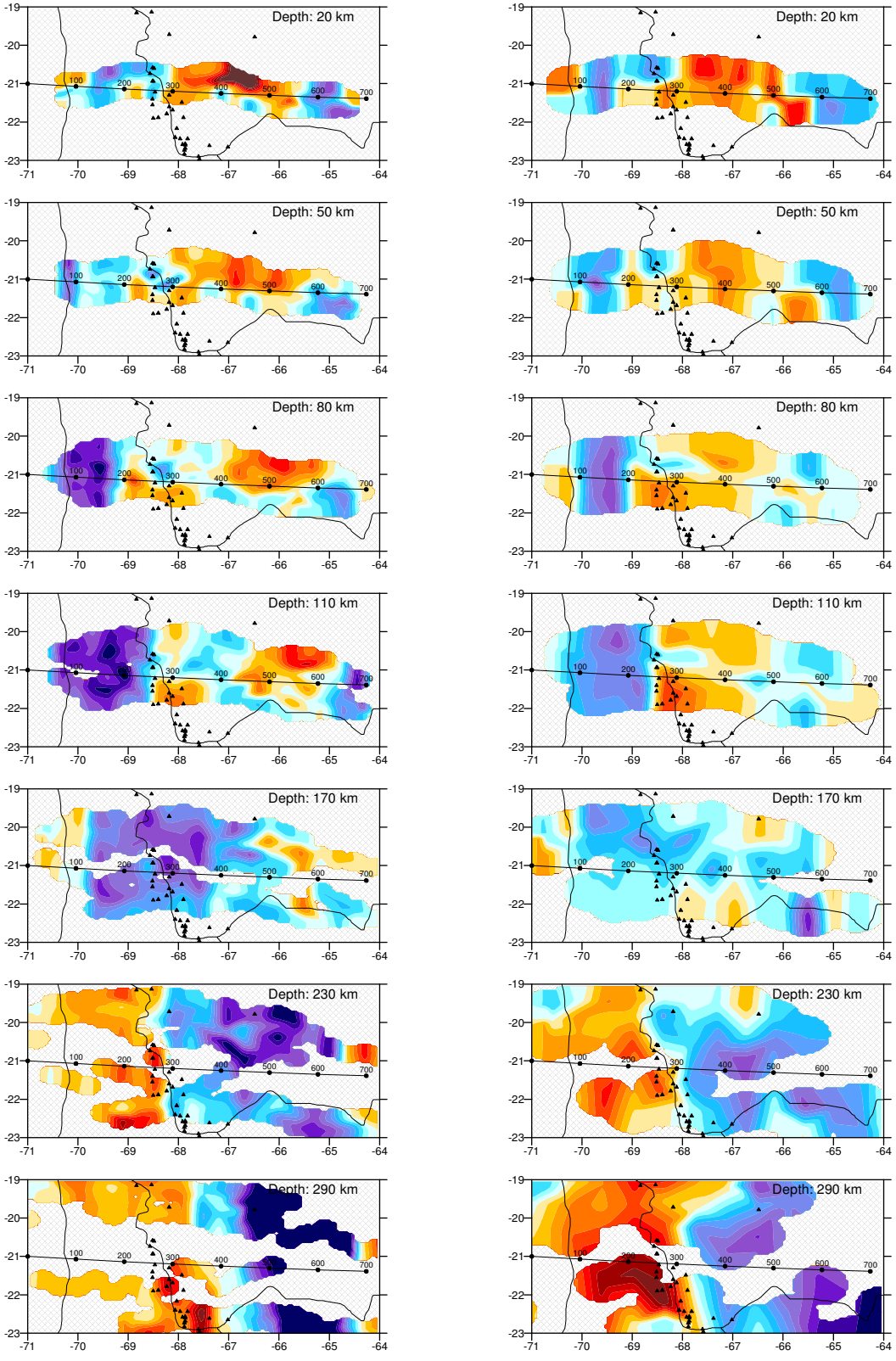

P- and S- velocity in %

Appendix A.5. Puna

Horizontal Sections P- and S- waves Puna 25.5°S
Real data Inversion

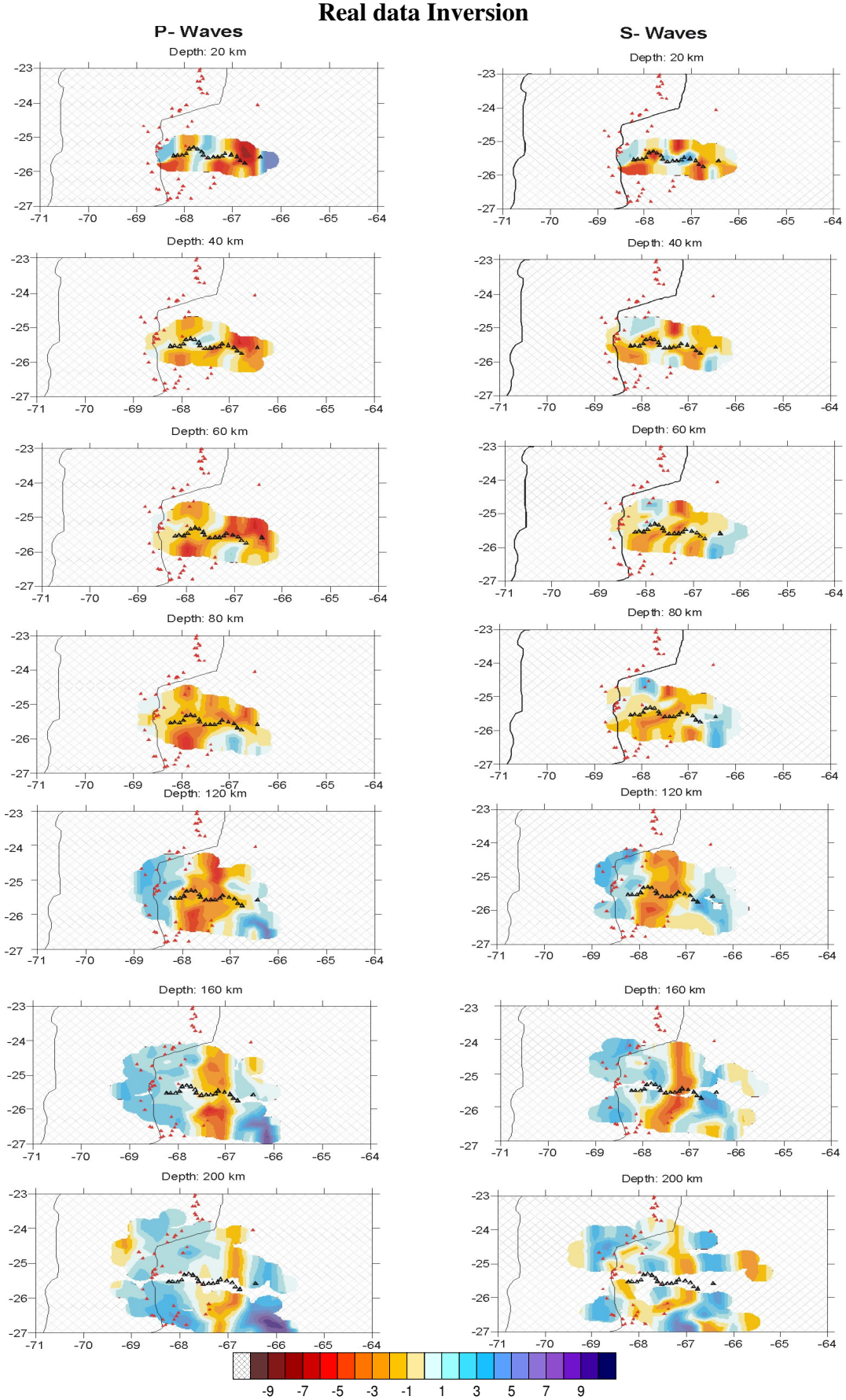

P- and S- velocity in %

Appendix A.6. Altiplano

Distribution of P- wave residuals for different back azimuth (BAZ)
Altiplano (Chile – Bolivia) 21°S

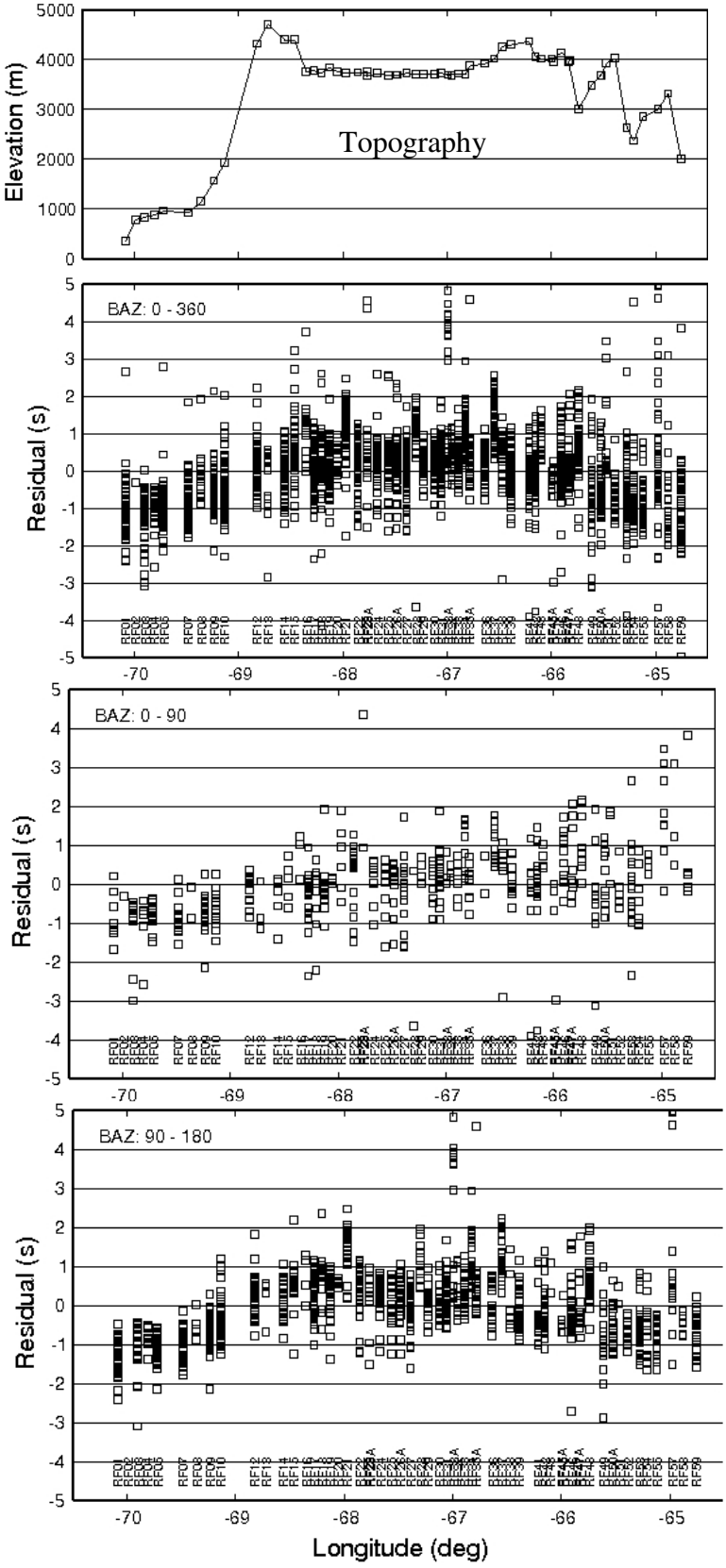

Appendix A.6. Altiplano

Distribution of P- wave residuals for different back azimuth (BAZ) Altiplano (Chile – Bolivia) 21°S

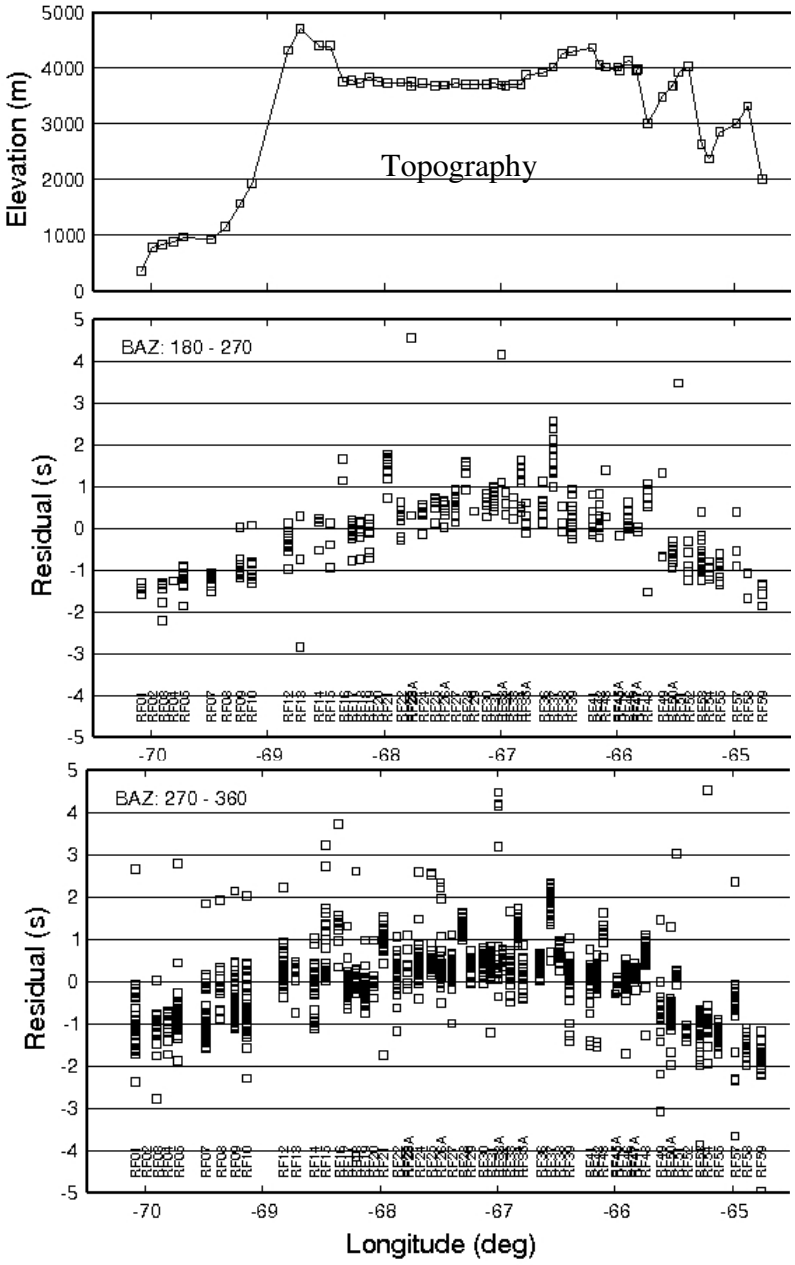

Appendix A.6. Puna

Distribution of P- wave residuals for different back azimuth (BAZ)
Argentine Puna 25.5°S

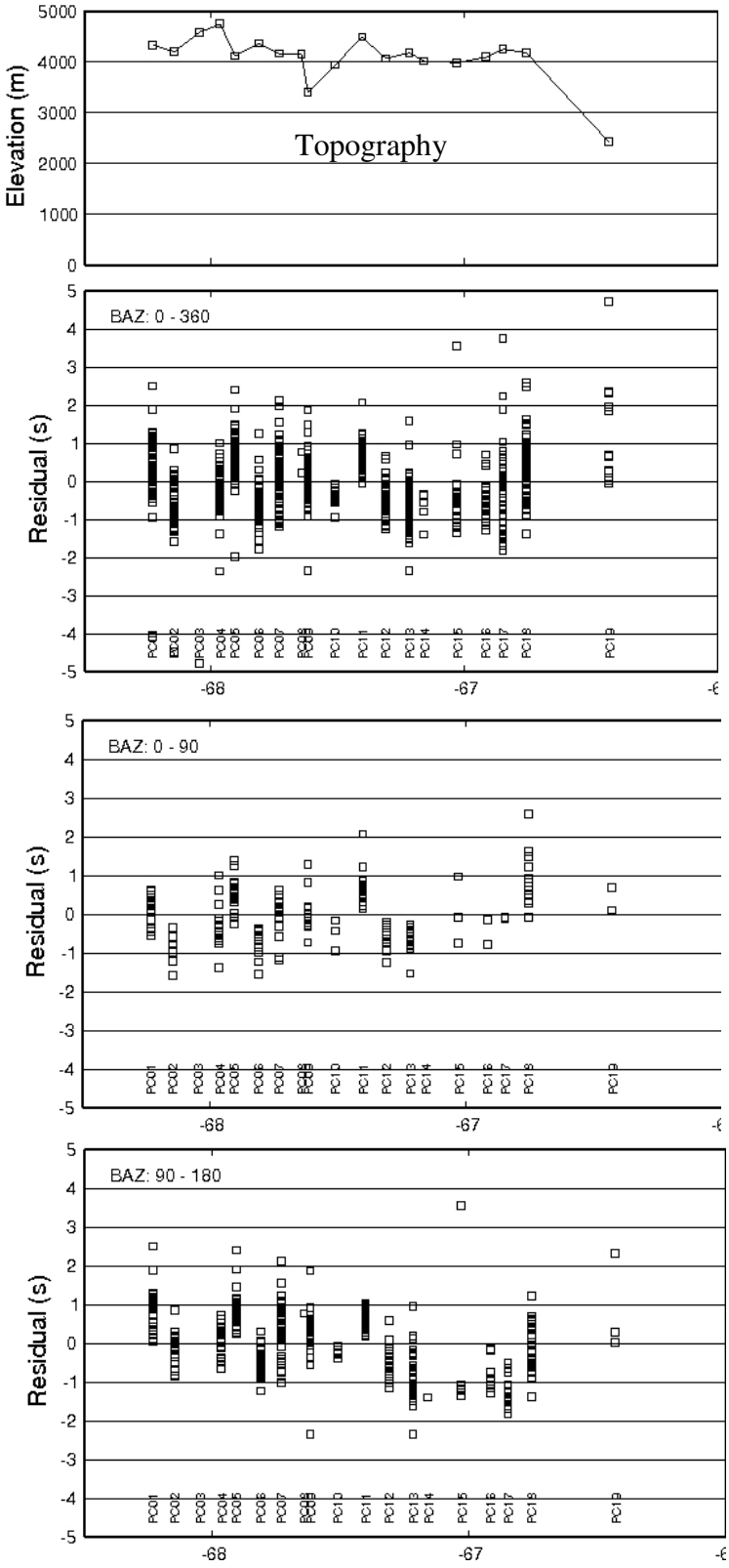

Appendix A.6. Puna

Distribution of P- wave residuals for different back azimuth (BAZ)
Argentine Puna 25.5°S

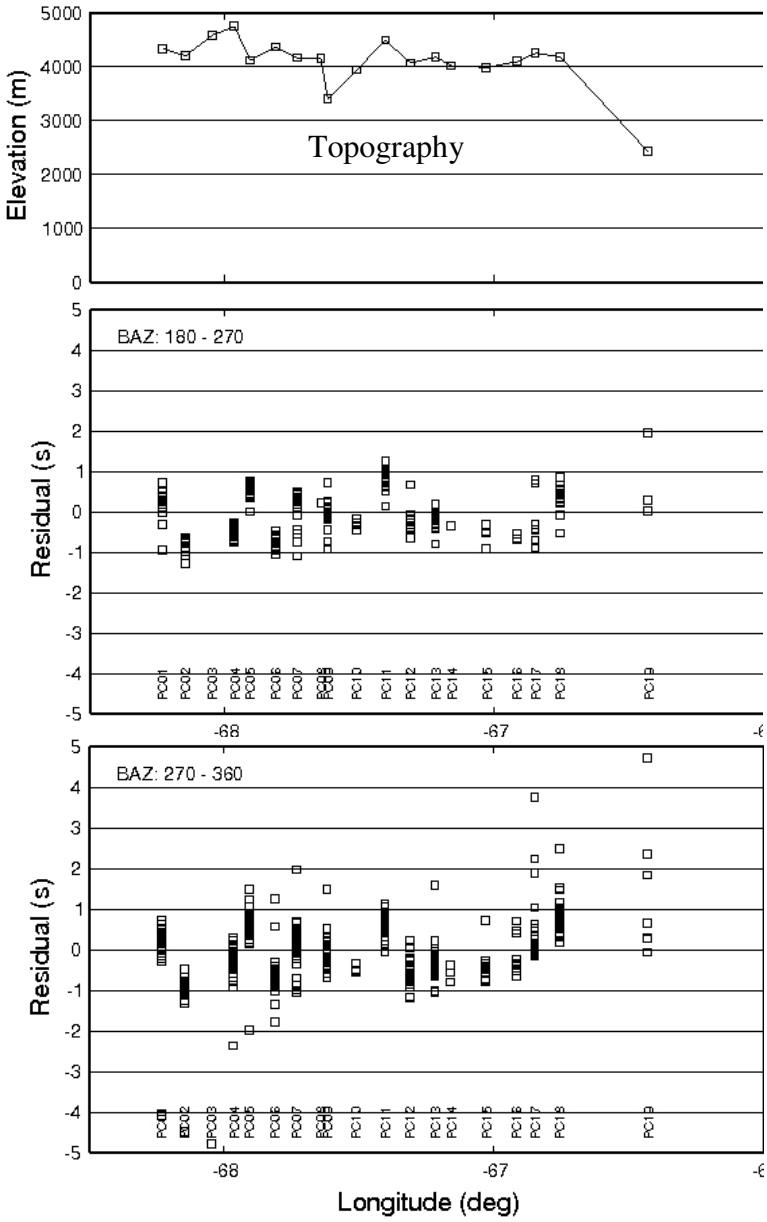

Acknowledgements

I would like to express my gratitude to my supervisor Priv. Doz. Dr. Günter Asch for his support during my PhD work at the GFZ Potsdam. Without his amazing experience, the fieldwork would never have been carried out successfully. In particular, I want to thank him for his support during the hard times and also for the long discussions with Luigi at the library in Salta during the good times. To Prof. Dr. Rainer Kind my co-supervisor, I wish to thank him for encouraging the present thesis and providing help when I most needed it.

My gratitude also goes to Prof. Dr. Frank Schilling, Prof. Dr Onno Oncken, Dr. Peter Wigger and Geophysicist Carsten Dinske for integrating the commission. I also wish to remember Prof. Dr. Peter Giese (+RIP) as the initiator of the SFB-267 "Deformation Processes in the Andes" project, and the SFB-267 group for their support since my first steps in the Andes back in 1996.

I also thank Dr. Ivan Koulakov, who provided his tomography software and taught me how to get the best out of it. With his help, knowledge and suggestions, this work was improved significantly. He was very patient with my many questions and even had time for me when he was back in Siberia. He is also a great artist. The seismic software used was SHM (Seismic Handler Motif) from Klaus Stammler (Seismological Observatory Gräfenberg - SZGRF).

A very special thanks goes to my friend and colleague Dr. Xiahoui Yuan for his continuous help and support. Working with him was one of the best things that ever happened to me. Dr. Yuan is an inspiring scientist that was available whenever I had problems, always giving the right advice or just making things look easier. Without his help and knowledge this work could have never been done. I also thank his wife Dr. Xuequing Li for her help.

I wish to thank Dr. Ingo Wölbern who kindly provided the receiver function data obtained from our project. To Dr. Winfried Hanka from Geofon (GFZ) for data management and support; Dr. Karl Heinz Jäckel, Dr. Kurt Wylegalla and Ing. Mike Hönig for helping with the instruments. To the GIPP (Gerätepool at GFZ) for providing the instruments and to Dr. Jens Bribach. To Liane Tröger for taking good care of everything.

To Dr. Friedrich Lucassen, Dr. Bob Trumbull, Dr. Kevin Fleming and A. Manzanares who carefully read the first versions of this manuscript and helped to improve the quality of the final version. Their patience, critical comments and time must also be acknowledged. To Prof. Dr. Ron Hackney for help with the residual gravity interpretation and comments on the data.

Many institutions have played a great part in the deployment of instruments in the field and the periodic visits to the stations, namely the Universidad Catolica del Norte, Antofagasta (Chile), SERGEOMIN, La Paz (Bolivia) and Instituto Geonorte from the Universidad Nacional de Salta (Argentina). I especially would like to thank the following people in Chile: Dr. Hans Wilke, Juan Oliva and J.L. Cerda; in Bolivia: Dr. Sohrab Tawackoli and Ing. Ivar Alcozer and in Argentina: Prof. Dr. Jose Viramonte, Pablo Maciel, Cesar Abraham, Pablo Dib Ashur, Fede, Mauri and Jose L. Heit.

Special thanks also goes to Forough Sodoudi, Amerika Manzanares and Mirjam Bohm, Peter Pilz, Jörn Kummerow, Barbara Heuer, Joachim Saul, X. Yuan and Xueqing Li for the lovely atmosphere at work and nice times shared among the glasses of wine and empanadas during the weekends.

To my dear mother Elba and to my beloved father Jose who died last year……I miss you dad. This thesis is dedicated to my wife Simone for all her love and support.